Quantum transport in topological insulator HgTe point contacts

Dissertation

zur Erlangung des Doktorgrades
der Naturwissenschaften (Dr. rer. nat.)
der Fakultät für Physik
der Universität Regensburg

vorgelegt von

Elisabeth Richter
aus Mainz

im Jahr 2025

Promotionsgesuch eingereicht am: 14.01.2025

Die Arbeit wurde angeleitet von: Prof. Dr. Dieter Weiss

Prüfungsausschuss:
Vorsitzender: Prof. Dr. Klaus Richter
1. Gutachter: Prof. Dr. Dieter Weiss
2. Gutachter: Prof. Dr. Dominique Bougeard
weiterer Prüfer: Prof. Dr. Sergey Ganichev

Datum des Promotionskolloquiums: 23.07.2025

Contents

1. Introduction

In his Nobel Prize lecture in 1985, Klaus von Klitzing stated that "one may come to the conclusion that such a complicated system like a semiconductor is not useful for very fundamental discoveries. Indeed, most of the experimental data in solid state physics are analyzed on the basis of simplified theories, and very often the properties of a semiconductor device are described by empirical formulas since the macroscopic details are too complicated" [1]. It is the Aristotelian definition of science that justifies precisely this approach, according to which every acquisition of knowledge arises from existing knowledge, according to clear and demonstrable rules [2]. True knowledge is obtained through both deduction, i.e., logical reasoning, and induction, which refers to empirical observation. The yet unknown has to be explained, or at least described, by the known - and only by that - to achieve a true increase in knowledge. Indeed, 40 years after one of the most influential discoveries in quantum transport, in the present work as well, we will make use of largely simplified models to describe most fundamental properties of transport at quantum point contacts in an utterly complicated material system, as is the 3D topological insulator HgTe.

Unlike conventional insulators, topological insulators host topologically protected conducting states at their edges or surfaces. Due to this property, they are envisioned to play a crucial role in quantum computing [3]. In 2005, Kane and Mele introduced the concept of topological insulators (TIs) in two dimensions [4], later extending it to three dimensions [5]. The first experimental realization of a 2D topological insulator was achieved in a CdTe/HgTe/CdTe quantum well system [6, 7]. Recently, operation of a quantum point contact in a two-dimensional topological insulator was realized successfully, showing interaction between edge states, usable for future braiding applications [8]. A major driving force behind this research is the search for Majorana bound states (MBS), which in condensed matter physics are quasiparticle excitations. Their free particle counterparts are called Majorana fermions, which are their own antiparticles [9]. MBS are predicted to emerge in semiconductor/superconductor hybrid structures [10, 11]. Topological quantum computing as a field of research has experienced great turbulence in recent years [12], and yet, it continues in the race to discover the eagerly anticipated Majoranas [13, 14]. The hunt for Majorana bound states has also taken hold of our group (see Ref. [15–17]).

This work, however, more distantly from these cutting-edge topics in modern solid-state physics, is devoted to the study of a well-known system, the quantum

point contact, embedded in the rather intricate and lesser-known TI material HgTe. Quantum point contacts (QPCs) are narrow constrictions between two wider regions of an electron system and serve as a fundamental component of mesoscopic physics. They exhibit quantized conductance in units of $2\ e^2/h$ due to their one-dimensionality, highlighting the wave nature of electrons and the energy quantization of electronic states within the constriction [18, 19]. These observations provide experimental confirmation of the relationship between conductance and transmission, a concept originally proposed by Landauer in 1957 [20, 21]. The Landauer-Büttiker approach describes conductance and resistance in a four-point geometry, expressing these quantities in terms of transmission and reflection probabilities at the point contact [22]. In fully ballistic and adiabatic systems or within the quantum Hall regime, these probabilities take on discrete values. Conductance quantization has also been observed in metallic QPCs based on 3D systems [23, 24], though with less precision than in their semiconductor-based 2D counterparts.

QPCs are envisioned to play a crucial role in quantum computing. They can function as ultra-sensitive charge sensors capable of detecting the quantum state of a nearby qubit without collapsing it, making them essential for reliable quantum measurements [25–27]. Their high controllability and ability to perform non-invasive readout helps to preserve quantum coherence, a key requirement for the very fragile quantum states [28]. A particularly exciting application of QPCs in quantum computing lies in topological quantum computation, a field that has gained prominence due to the potential realization of robust qubits using topological states of matter [29–31].

QPCs, together with larger nanowires, have been proposed in topological insulator-based systems as potential probes for MBS, particularly when coupled to an s-wave superconducting wire via proximity effects [32, 33]. The presence of MBS would be indicated by an unconventional sequence of conductance steps given by $(n + \frac{1}{2})\frac{4\ e^2}{h}$ with $n = 0, 1, 2, 3....$ Experiments have observed conductance doubling in QPCs from $2\ e^2/h$ in the normal state to $4\ e^2/h$ in the superconducting state, reflecting proximity-induced superconductivity in the two-dimensional electron gas (2DEG) [34, 35]. Similar conductance anomalies have been proposed in 1D nanowires with a normal and a superconducting contact [36]. Beyond quantum computing, QPCs have significantly shaped other fields of research such as spinorbitronics [37–40], where they enable precise control of electron transport in materials with strong spin-orbit interactions, opening avenues for novel spintronic devices [41, 42].

Our aim in this project was to demonstrate the existence of conductance quantization in 3D TI HgTe, as is already known for 2D TI HgTe point contacts as well [8]. In the present study, quasi-ballistic QPCs made from 3D TI strained HgTe were studied systematically with respect to their geometry. Conductance was measured at unusual, but stable values instead of reaching the quantized state. The precise analysis of the conductance behavior including a simplified phenomenological Landauer-Büttiker model lies at the heart of this work.

The outline of this thesis is as follows.

- Chapter 2 provides the fundamental theoretical background for understanding transport phenomena in QPCs, focusing on 2DEGs, the quantum Hall effect, and ballistic transport in quantum point contacts. It discusses the impact of spin-orbit interaction and Zeeman splitting, which play a crucial role especially in semiconductors with strong spin-orbit coupling such as HgTe. The chapter also introduces topological concepts, emphasizing the role of HgTe as a three-dimensional topological insulator and the emergence of surface states.

- Chapter 3 describes the experimental methods used for fabricating and measuring HgTe-based quantum devices. The design of the MBE-grown materials, as well as cleanroom fabrication processes such as lithography and etching, and the deposition of oxide layers and topgates are described. The cryogenic measurement setups, including a dilution refrigerator system, and electronic instrumentation for transport measurements are explained. Possible sources of measurement errors are discussed, such as capacitive coupling and frequency-dependent noise, and strategies how to mitigate them for high-precision experiments are outlined.

- Chapter 4 examines the macroscopic transport properties of the material under study by analyzing charge carrier density, mobility, and especially the quantum Hall effect. Measurements performed on a Hall bar structure reveal the coexistence of various types of charge carriers within different gate voltage and magnetic field regions. The study employs the two-carrier Drude model and Landau quantization to extract charge carrier densities and mobilities, which show a strong dependence on gate voltage.

- Chapter 5 presents combined experimental and theoretical results of the study of electron transport across QPCs fabricated on HgTe-based 3D topological insulators. The key findings of this chapter were published in Ref. [43]. In the absence of a magnetic field, quantization of conductance is not observed. The introduction of a perpendicular magnetic field enhances the adiabaticity, resulting in the appearance of distinct anomalous steps at large magnetic fields. In particular, the heights of the fundamental plateaus systematically register values smaller than e^2/h, despite perfect Hall quantization in the macroscopic vicinity of the constriction. While such behavior could initially be interpreted as trivial impurity scattering, our results reveal a preference for certain conductance values over others. Based on numerical tight-binding calculations and a phenomenological Landauer-Büttiker approach, we attribute these atypical, non-integer quantized plateaus to significant scattering effects at the point contact. This is achieved by implementing a well-known Hamiltonian for 2D TI systems. Furthermore, our analysis of 15 devices reveals a clear categorization into three distinct groups based on their conductivity. Within

each group, the devices show quantitatively similar behavior. We propose that the QPC acts as a filter whose transmission depends on the structural properties of the energy bands within the QPC. For larger point contacts, the conductance behavior transitions from step-like to oscillation-like patterns, resembling Shubnikov–de Haas oscillations, indicating a gradual shift toward macroscopic transport behavior.

- Chapter 6 investigates the effect of a tilted magnetic field on the conductance of the QPCs. It explores how the conductance quantization pattern changes when the magnetic field is tilted, introducing both a changing in-plane and a constant out-of-plane component. The experimental results reveal a parity effect in the valence band, where odd-numbered conductance steps disappear with increasing tilt angle, a phenomenon attributed to the interplay between Zeeman splitting and orbital splitting. The theoretical framework considers the effect of the in-plane component of the magnetic field, taking into account the uniquely large Zeeman splitting in the valence band of HgTe. The finding proves that the conductivity of the QPC in strong magnetic fields is mainly determined by the quantization of two-dimensional carriers in adjacent macroscopic regions, even when the parallel component of the magnetic field is twice as high as the perpendicular one. This indicates an unexpected constancy of the properties of the QPC as a filter element.

- Finally, a summary and conclusion of the results obtained, together with an outlook on the topic with possible advanced devices, is given in Chapter 7. These include especially structures based on the present QPC system and developing it further, such as shaped nanowires consisting of two constrictions, which could serve as the basis for quantum dots with discrete energy levels [44], a fundamental building block of quantum computing.

2. Theoretical concepts

This chapter contains the fundamental theoretical background, necessary for the understanding of transport phenomena in quantum point contacts. First, the properties of a two-dimensional electron gas (2DEG) are explained. The transition from a classical description of transport to a quantized behavior in strong magnetic fields, leading to the occurrence of the quantum Hall effect, is illustrated. As quantum point contacts represent ideal quantum wires, ballistic transport in these is explained in detail. Especially due to experiments conducted in tilted magnetic fields, Zeeman splitting is introduced. As HgTe is a material with strong spin-orbit coupling, significantly affecting the transport behavior, spin-orbit interaction is discussed. Based on the quantum Hall state, the topological order of band structures is introduced, which allows us to explain the appearance of surface states in the three-dimensional (3D) topological insulator HgTe. The presentation in this chapter mostly follows Ihn [45] and Hasan and Kane [46]. Apart from the citations given, further detailed information on the presented topics can also be found especially in the theses [47–50] from our group.

2.1 Transport in two-dimensional electron gases

The peculiarity of a 2DEG consists in a limitation of the movement of electrons in two directions in space, while it is prohibited in the third direction. 2DEGs have been extensively investigated in Si-MOSFET (metal–oxide–semiconductor field-effect transistor) devices [51], high-mobility AlGaAs/GaAs heterostructures [52], and in recent years, in graphene [53] and topological insulators such as HgTe [54]. In a 2DEG, the energy of the system can be expressed as the sum of the discrete energy levels E_n, defined by the 1D confinement, and the kinetic energy of free motion in x and y-direction [45]:

$$E = E_n + \frac{\hbar^2}{2m^*}(k_x^2 + k_y^2), \tag{2.1}$$

with m^* being the effective mass of an electron, $\hbar$ the reduced Planck's constant and k_x and k_y the x- and y-component of the wave vector. The resulting subband structure is illustrated in Fig. 2.1 (a). The density of states (DOS) $D(E)$ of one subband is defined as the number of available states dN in the vicinity of a certain

energy E in an infinitesimal interval dE [45]:

$$D(E) = \frac{dN}{dE} = \left(\frac{g_s k dk}{2\pi}\right)\left(\frac{m^*}{\hbar^2 k dk}\right). \tag{2.2}$$

Here, we introduce the spin degeneracy g_s, which equals 2 for the free electron in vacuum. In a 2DEG, only the lowest subband is occupied. Consequently, its density of states is independent of the energy. In two-dimensional systems, the density of states is discretized to [55]

$$D_{2D}(E) = \frac{g_s m^*}{2\pi\hbar^2}. \tag{2.3}$$

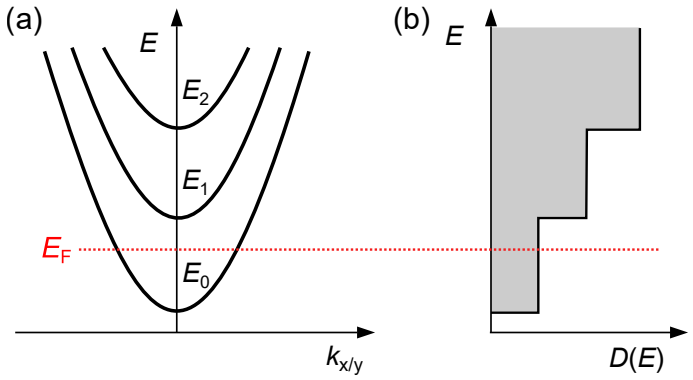

Fig. 2.1: (a) Dispersion relation for the lowest three bound states in a 2DEG (absent a magnetic field). The position of the Fermi energy, situated between the highest occupied and lowest unoccupied subband level, is indicated in red. (b) The density of states (DOS) $D(E)$ as a function of energy E is a step function. Because only the lowest subband E_0 is occupied in a 2DEG, the Fermi energy lies within the lowest step. It follows that the energy in a 2DEG is constant. Adapted from [45].

In general, $D(E)$ is the sum over the density of states of all occupied subbands. For two-dimensional systems, this results in a step-function on the scale of energy, which is illustrated in Fig. 2.1 (b). Charge carriers are occupied up to the so-called Fermi energy E_F. As only the lowest subband E_0 is occuppied in a 2DEG, the Fermi energy E_F falls within the lowest step, leading to a constant energy in the 2DEG. In the lowest subband, the charge carrier density (or electron density) n_s in a 2DEG is related to the Fermi energy by [45]

$$n_s = D_{2D}(E) \cdot E_F. \tag{2.4}$$

Consequently, E_F can be derived directly from the charge carrier density. For a free electron in a 2DEG, it is

$$E_F = \frac{\pi\hbar^2 n_s}{m^*}. \tag{2.5}$$

In order to be able to shift the Fermi energy, a structured metallic gate is applied to the device, which modifies the charge carrier density in the system locally by applying a gate voltage V_g. The Fermi energy is also closely related to the so-called Fermi wavelength λ_F. If the device dimensions become comparable to λ_F, size quantization in solid-state devices takes place. Further, we define the Fermi wave vector as $k_F = \sqrt{g_s \pi n_s}$, from which we deduce the Fermi wavelength, which is given by $\lambda_F = 2\pi/k_F$. The Fermi wavelength of electrons in semiconductor systems is on the order of a few nanometers.

2.1.1 Classical magnetotransport

The transport in a 2DEG is described by the classical Drude model when applying only a very weak or zero magnetic field $\vec{B}$ [56]. The Drude model illustrates the movement of non-interacting electrons accelerated by an electric field $\vec{E}$. From time to time, they scatter due to defects, impurities or phonons. This is described by the mean (or Drude) scattering time τ_0, discussed later in this section in more detail. Consequently, the electrons move with a constant mean drift velocity $\vec{v}_D$, driven by an external electrical field. Taking into account a magnetic field $\vec{B} = (0, 0, B)$ perpendicular to the 2DEG in the (x, y)-plane and neglecting scattering, the electron moving with velocity $\vec{v}$ in an electric field $\vec{E}$ and a magnetic field $\vec{B}$ experiences the Lorentz force $\vec{F}_L = -e(\vec{E} + \vec{v} \times \vec{B})$. Taking into account scattering events, the equation of motion can then be written as

$$m^* \frac{d\vec{v}}{dt} = -e(\vec{E} + \vec{v}_D \times \vec{B}) - m^* \frac{\vec{v}_D}{\tau_0}, \tag{2.6}$$

with the current density $\vec{j} = -en_s\vec{v}_D$, and, herein, the elementary charge e and the charge carrier density n_s [45]. Considering the steady-state condition, i.e., $\frac{d\vec{v}}{dt} = 0$, we obtain from Ohm's law

$$\begin{pmatrix} j_x \\ j_y \end{pmatrix} = \begin{pmatrix} \sigma_{xx} & \sigma_{xy} \\ -\sigma_{xy} & \sigma_{xx} \end{pmatrix} \begin{pmatrix} E_x \\ E_y \end{pmatrix}. \tag{2.7}$$

The longitudinal conductivity (referring to a Hall bar square, as depicted in Fig. 2.2)

$$\sigma_{xx} = \frac{n_s e}{B} \frac{\omega_c \tau_0}{1 + \omega_c^2 \tau_0^2} \tag{2.8}$$

and Hall conductivity

$$\sigma_{xy} = -\frac{n_s e}{B} \frac{\omega_c^2 \tau_0^2}{1 + \omega_c^2 \tau_0^2} \tag{2.9}$$

are introduced here, with the frequency of the circular motion of the electron, the cyclotron frequency

$$\omega_c = \frac{eB}{m^*}. \tag{2.10}$$

The quantities σ_{xx} and σ_{xy} will be discussed later in more detail. The components of the resistivity can be calculated via tensor inversion:

$$\begin{pmatrix} \rho_{xx} & \rho_{xy} \\ \rho_{xy} & \rho_{yy} \end{pmatrix} = \begin{pmatrix} \sigma_{xx} & \sigma_{xy} \\ \sigma_{xy} & \sigma_{yy} \end{pmatrix}^{-1} = \frac{1}{\sigma_{xx}\sigma_{yy} + \sigma_{xy}\sigma_{xy}} \begin{pmatrix} \sigma_{xx} & \sigma_{xy} \\ -\sigma_{xy} & \sigma_{xx} \end{pmatrix}. \tag{2.11}$$

It follows that the longitudinal resistivity is [45]

$$\rho_{xx} = \rho_{yy} = \frac{m^*}{n_s e^2 \tau_0} = \frac{1}{e n_s \mu}, \tag{2.12}$$

with the mobility

$$\mu = \frac{e\tau_0}{m^*} \tag{2.13}$$

and the Hall resistivity [45]

$$\rho_{xy} = -\frac{B}{n_s e}. \tag{2.14}$$

In a Hall bar structure, which is shown in Fig. 2.2, ρ_{xx} and ρ_{xy} can be determined experimentally. A current I is applied between contacts 1 and 4. The longitudinal voltage U_{xx} can be measured between contacts 5 and 6, while the Hall voltage U_{xy} between contacts 2 and 6. This leads to the longitudinal resistivity (resistance per Hall bar square)

$$\rho_{xx} = \frac{U_{xx}}{I}\frac{W}{L} \tag{2.15}$$

and

$$\rho_{xy} = \frac{U_{xy}}{I}, \tag{2.16}$$

with W the width of the Hall bar, and L is the distance between adjacent contacts.

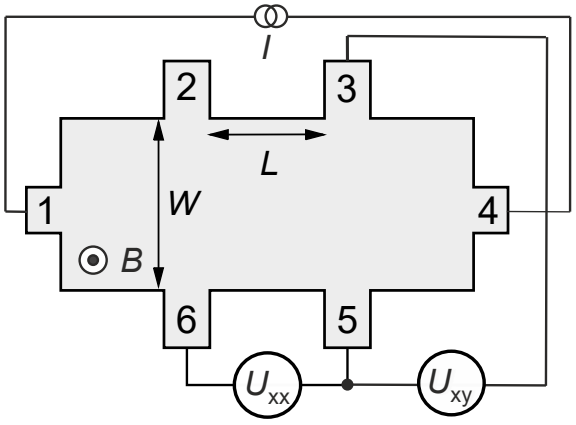

Fig. 2.2: Hall bar device, where W is the width of the Hall bar and L the length between two adjacent contacts. A current is applied between contacts 1 and 4. The longitudinal voltage U_{xx} can be measured between contacts 5 and 6, and the Hall voltage U_{xy} between contacts 3 and 5, respectively. With these values, it is possible to determine the carrier density n_s and the mobility μ. Adapted from [43].

The charge carrier density n_s is obtained from the measurement of the Hall resistivity [57] via

$$n_s = \frac{1}{e\frac{d\rho_{xy}}{dB}}. \tag{2.17}$$

The electron mobility is then given by

$$\mu = \frac{\frac{d\rho_{xy}}{dB}}{\rho_{xx\ (B=0)}}. \tag{2.18}$$

In real systems, however, the charge carriers show scattering events between each other. Therefore, we will now introduce some characteristic quantities linked to scattering processes. The elastic mean free path length l_e of a particle can be described as the average length that the particle can travel freely, i.e., before a collision, which could change its momentum. In mesoscopic devices, transport is considered ballistic (i.e., unimpeded by scattering effects) for device sizes of $L \leq l_e$. In our system, typical values of l_e are on the order of several micrometers at low temperatures. Coming back to the Drude scattering time, the scattering angle is considered. It is not averaged in order to take into account all scattering processes precisely. For this purpose, each scattering event is weighted with the scattering angle ϕ. The Drude scattering time τ_0 is then given by:

$$\frac{\hbar}{\tau_0(E)} = n_i \frac{m^*}{2\pi\hbar^2} \int_0^{2\pi} d\phi (|v^i(q)|^2)_{\text{imp}} (1 - \cos\phi). \tag{2.19}$$

where n_i denotes the areal density of scatterers $n_i = N_i/A$ [45]. Obviously, scattering angles close to $\phi = 180°$, i.e., backscattering, contribute strongly. With τ_0, the elastic mean free path can be expressed by $l_e = v_F\tau_0$, and extracted from experimentally accessible quantities via

$$l_e = \frac{\hbar}{e}\mu\sqrt{g_s\pi n_s}. \tag{2.20}$$

2.1.2 Landau quantization

Now, we apply a magnetic field in perpendicular direction to the sample plane. At higher magnetic fields (typically at several 100 mT), the classical Drude model does not apply anymore. In this case, the orbital quantization has to be taken into account, which will be discussed in the following.

In the plane of a 2DEG, the Lorentz force $\vec{F} = e(\vec{E} + \vec{v} \times \vec{B})$ acts on the electrons. It forces them to move on circular orbits. As a consequence, the radius of these cyclotron orbits at a given magnetic field is quantized and given by multiples of the magnetic length

$$l_c = \sqrt{\frac{\hbar}{eB_\perp}}, \tag{2.21}$$

which is the characteristic length scale of the cyclotron motion at a given magnetic field [45]. The energy of the electron is quantized according to

$$E_n = \frac{1}{2} m\omega_c^2 (\sqrt{2n} l_c)^2 = n\hbar\omega_c, \tag{2.22}$$

with the cyclotron energy

$$E_c = \hbar\omega_c. \tag{2.23}$$

Hence, the electron cyclotron motion gives rise to the so-called Landau quantization and depends only on the magnetic field component perpendicular to the 2DEG plane ($B_\perp$).

The Landau quantization occurs when electron energy levels condense into discrete Landau levels due to quantized cyclotron motion.

The derivation of the energy values of the quantized plateaus (or Landau levels, respectively) will be presented in the following. The Schrödinger equation of an effectively free electron in a constant magnetic field $\vec{B} = (0, 0, B)$ is given by

$$\frac{1}{2m^*}(-ih\nabla + e\vec{A})^2 \Psi = E\Psi, \tag{2.24}$$

with the vector potential $\vec{A} = (0, Bx, 0)$. The ansatz $\Psi(x, y) = \widetilde{\Psi}(y) e^{ik_x x}$ leads to the eigenvalue problem

$$\left(\frac{p_y^2}{2m^*} + \frac{1}{2} m^* \omega_c^2 \Big(y - \frac{\hbar k_x}{|e|B} \Big)^2 \right) \widetilde{\Psi}(y) = E \widetilde{\Psi}(y). \tag{2.25}$$

This is the equation of a one-dimensional quantum mechanical harmonic oscillator with the k_x-dependent center coordinate $y_0 = \frac{\hbar k_x}{|e|B}$. As a result, the quantized energy states are given by

$$E_n = \hbar\omega_c (n + \frac{1}{2}). \tag{2.26}$$

with the quantum number n. All states of different k_x, but the same quantum number n are energetically degenerate and form the so-called Landau level (LL). The energy

of a given Landau level increases linearly with the magnetic field B. This leads to the so-called Landau fan, an energy diagram depicted in Fig. 2.3. The number of occupied Landau levels is given by the filling factor

$$\nu = \frac{n_s}{n_L} = \frac{hn_s}{eB}, \tag{2.27}$$

with n_L the number of allowed states in each LL. It should be noted that n_L is not identical to the quantum number n. ν tells us how many Landau levels are occupied at a given magnetic field at zero temperature. At a fixed electron density n_s, the Fermi level of the electron gas oscillates as a function of B, i.e., with filling factor ν proportional to $1/B$. If the spin splitting, which will be considered later in Sec. 2.3.1, is negligible compared to the Landau level splitting, each Landau level hosts $2n_L$ electrons per unit area and the Fermi energy jumps between Landau levels at even values of ν [45]. However, for simplicity, the spin of the electrons is neglected in the above consideration and will be considered later in connection with Zeeman splitting.

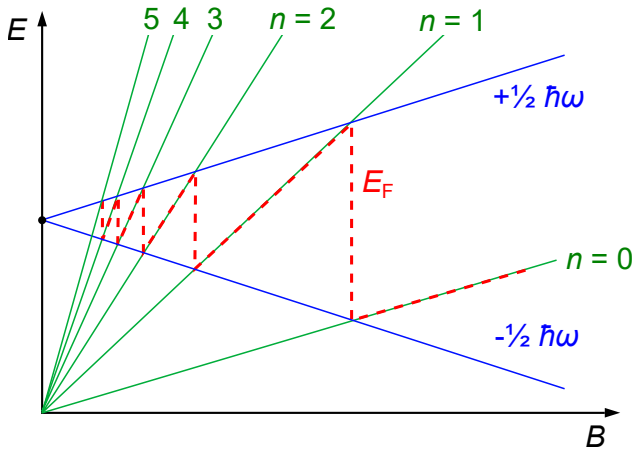

Fig. 2.3: Behavior of the Fermi energy E_F (red) as a function of magnetic field $B_\perp$. The slope of each Landau level (green lines) depends on the quantum number n. The cyclotron energy (blue) increases linearly with $B_\perp$. If the Fermi energy lies within two Landau levels, it increases linearly with the magnetic field, until enough states are available in the next LL. Then, E_F drops down to the Landau level below $(n-1)$, repeating the process, resulting in a fan-like diagram with oscillating E_F, the Landau fan. Adapted from [45].

In Fig. 2.4, the DOS is illustrated for classical Drude transport (in (a)) as well as the idealized quantized transport in strong magnetic fields (in (b)). In reality, electrons happen to be localized on impurities, leading to a broadening of Landau levels. This situation is sketched in Fig. 2.4 (c). The delocalized states, which are responsible for transport, are close to the DOS maxima (dark gray), whereas the

localized states do not contribute to transport (light gray). This is caused by spatial potential fluctuations, which are, for example, created by the random arrangement of charged dopants. They lift the degeneracy of a Landau level. This influences scattering at potential fluctuations limiting the lifetime of an electron in a certain quantum state. As a result, the ideal δ-shaped DOS peaks are broadened [45].

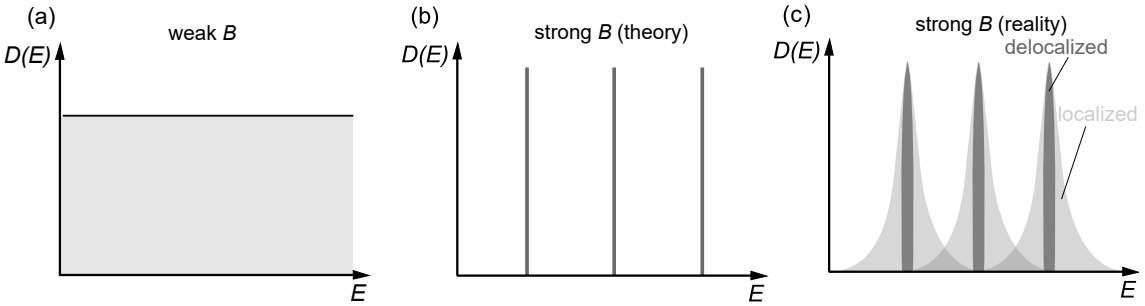

Fig. 2.4: Density of states in the classical and the quantum-mechanical transport model. (a) In the classical Drude transport regime at low magnetic fields, the DOS is constant. No Landau level broadening and splitting is necessary yet to describe this transport model. (b) Applying higher fields leads to the formation of a δ-peak-like distribution of the density of states. The discrete levels are called Landau levels. (c) In reality, the Landau levels are broadened because some electrons are localized on impurities. Only the delocalized states, which are close to the DOS maxima (dark gray area), contribute to transport. The localized states exhibit a lower DOS, where charge carriers can be localized on impurities, which leads to a reduction of transport. Adapted from [45].

In this context, we introduce the quantum lifetime (also quantum scattering time) τ_q, which describes the energy broadening Γ of the Landau levels by $\Gamma = \hbar/(2\tau_q)$ [45]. The quantum lifetime τ_q is a measure of the mean time a carrier remains in a particular state before being scattered to a different state. The quantum lifetime τ_q is given by

$$\frac{\hbar}{\tau_q(E)} = n_i \frac{m^*}{2\pi\hbar^2} \int_0^{2\pi} d\phi (|v^i(q)|^2)_{\text{imp}}. \tag{2.28}$$

Compared to τ_0, τ_q lacks the term $(1-\cos\phi)$. Thus, all scattering events are weighted equally. Unlike τ_q, τ_0 is a measure of the amount of time a carrier remains moving in a particular direction. In the case of τ_0, by including a factor of $(1-\cos\phi)$, the importance of large angle over small angle scattering events is emphasized. While τ_0 is typically calculated from Hall mobility measurements, the quantum lifetime τ_q is determined from an analysis of the magnetic field dependence of Shubnikov-de Haas oscillations. The determination of the lifetime of quantum states at arbitrary magnetic fields is difficult due to an interdependence of the scattering rate and the density of states [45]. The average length between two scattering events of arbitrary angles is called the quantum scattering length $l_q = v_F\tau_q$ [58].

2.1.3 Integer quantum Hall effect

We will now discuss the effect of quantization with the help of an exemplary measurement from our HgTe samples, which is shown in Fig. 2.5. A schematic of the DOS in Fig. 2.6 (a) and (b) will illustrate our explanation. The Hall resistance ρ_{xy} is measured in a 2D charge carrier system at low temperatures (typically at liquid helium temperature $T = 4.2$ K and lower) and high magnetic field, which is applied in perpendicular direction to the plane of the charge carrier system. It shows well-defined constant values over wide magnetic field and charge carrier density ranges, the so-called Hall plateaus. This effect is also referred to as the (integer) quantum Hall effect. Simultaneously, so-called Shubnikov-de Haas (SdH) oscillations in the longitudinal resistance ρ_{xx} emerge. The Hall plateau values are described by

$$R_H = \rho_{xy} = \frac{h}{ne^2}, \tag{2.29}$$

where h is Planck's constant, and n an integer value with $n = 1, 2, 3, ...$

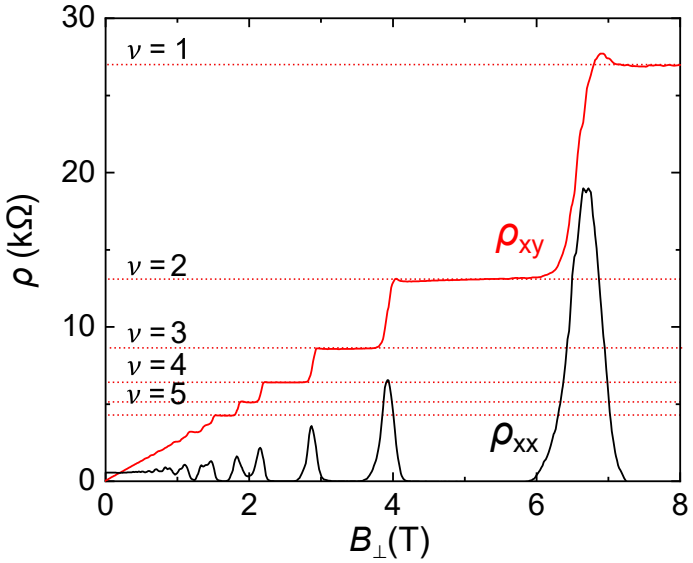

Fig. 2.5: Quantization of transport. Longitudinal ρ_{xx} (black) and Hall resistivity ρ_{xy} (red) as a function of the magnetic field in a 2DEG at gate voltage $V_g = 1.4$ V as an example from a device (e23) studied in this work. In the range of small magnetic fields (in the present case at $B_\perp \approx 0 - 0.5$ T), the behavior can be described classically using the Drude model. Here, the longitudinal resistance remains constant and the Hall resistance increases linearly with the magnetic field. For intermediate magnetic fields, Shubnikov-de-Haas oscillations occur (in the present example at $B_\perp \approx 0.5 - 1$ T), reaching zero at their minima. Quantized Hall plateaus can be found at magnetic field values where the SdH oscillations transform into minima reaching $\rho_{xx} = 0$ (here, at $B_\perp > 1$ T).

For $n = 1$, the value of R_H is $R_K \approx 25\,812.807...\Omega$, which is the Klitzing constant. The inverse value of R_K is the conductance quantum. The QHE and its relation to fundamental physical constants was discovered in 1980 by Klaus von Klitzing [59], which earned him the Nobel prize in 1985.

The SdH oscillations and the corresponding Hall plateaus can be explained by the fact that, depending on the position of the Fermi energy within a Landau level, scattering of electrons becomes possible, and the electrical resistance changes depending on the magnetic field. The scattering reaches its maximum (i.e., SdH oscillations show maxima, while the Hall resistance grows), when the Fermi energy coincides with a Landau level. Then, the number of conducting electrons is identical to the number of free electrons, due to scattering. If the Fermi energy lies between two Landau levels, then the electrons cannot overcome the energy gap to the next level. This is due to the low temperature, where scattering is no longer possible, but also the magnetic field has an influence, as it defines the distance between the Landau levels. A plateau forms in the Hall resistance, while the longitudinal resistance decreases to zero.

However, the appearance of Hall plateaus and SdH oscillations cannot be explained solely by the formation of individual scattering-broadened Landau levels. Therefore, the so-called edge channel model is introduced in the following, in which boundary effects, that were previously neglected, are now taken into account as well. In this model, electrons move on a cyclotron orbit in the presence of strong perpendicular magnetic fields (see Fig. 2.6 (a)). Inside the sample, the orbits are closed, not leading to any contribution to transport from a classical point of view.

In the edge regions, however, it is no longer possible to execute a complete cyclotron orbit, so that electrons are reflected at the edges, and so-called skipping orbits are created there. Due to the Lorentz force, the electrons are forced to move forward, irrespectively of scattering. As a result, charge carriers are no longer localized at the edge of the sample. Instead, the electrons travel along the sample edge without any dissipation. They propagate in one direction along one edge, and in the inverse direction along the opposite edge.

The potential at the edge of the sample causes the Landau levels to bend upwards (see Fig. 2.6 (b)). Thus, regardless of the position of the Landau levels, there are always states that intersect the Fermi energy. Since only the states below and including the Fermi level contribute to the current flow, one-dimensional edge channels arise at the intersection points of the Fermi energy with the Landau levels in the edge regions. These are particularly of importance when the Fermi energy lies just between two Landau levels, as is the case in Fig. 2.6 (c), since in this case, the current transport is carried exclusively by edge channels. This scenario is illustrated in Fig. 2.6 (b) with the red line. Here, the edge channel model allows us to explain the measured resistance: At this position of the Fermi energy, the edge channels are physically isolated, since no states exist in between. This results in dissipationless transport along the edges, and, as a consequence, the longitudinal resistance drops

to zero, i.e., a minimum is formed in the SdH oscillation. No potential difference develops in x-direction. This implies that one side of the sample shares the same potential as the contact where the current enters, e.g. contact 1 from Fig. 2.2. The opposite edge then matches the potential of the opposite contact 4. As a result, the potential difference U_{xy}, measured across contacts 3 and 5, equals the voltage applied between the contacts 1 and 4. This is a constant value then. If we consider the DOS picture (see Fig. 2.6 (c)), the E_F is located between two DOS-peaks. Then, the DOS decreases to zero or almost zero. Taking into account only the idea of Landau quantization, we would not be able to explain the QHE. With the edge channel model presented above, however, this becomes possible.

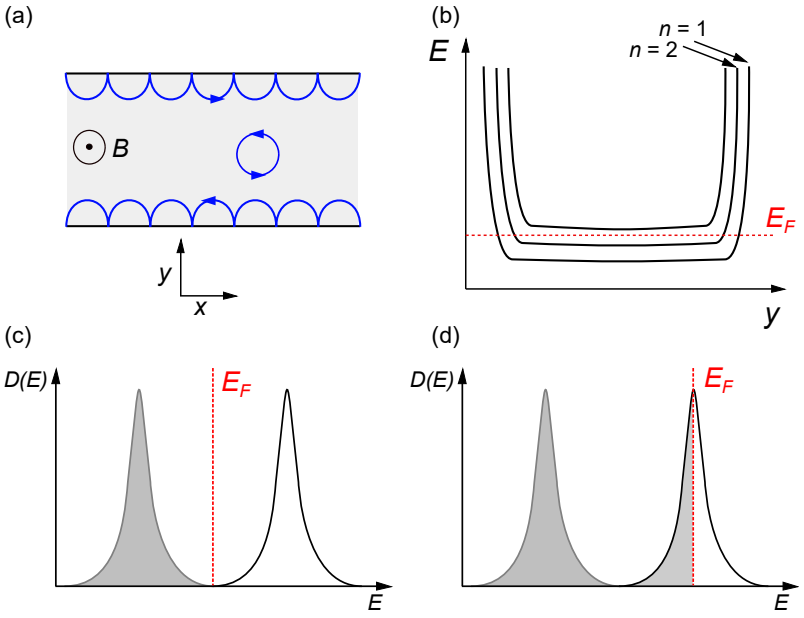

Fig. 2.6: (a) Electrons in a magnetic field move on cyclotron orbits (blue). Inside the sample, the orbits are closed, whereas at the sample edge, the electrons are reflected and forced to move forward in skipping orbits due to the Lorentz force. (b) Potential for the edge channels. The Landau levels are bent up due to the geometrical boundaries of the sample. Therefore, a Landau level crosses the Fermi energy E_F at the edge, although it is situated below E_F inside the sample. This provokes the formation of conducting one-dimensional edge channels. (c) DOS in the QHE regime: The gray peaks indicate filled Landau levels, while the transparent peaks correspond to empty ones. As E_F is located between two DOS peaks, the DOS is very low and hence no transport is possible, unless we take into account the edge channel model. (d) Here, E_F is located at a high DOS and, therefore, transport is possible also inside the sample. Adapted from [55].

Now, we consider the case where the Fermi energy is located within a Landau level (see Fig. 2.6 (d)). Here, the states inside the sample also contribute to transport.

Consequently, the edge channels are no longer isolated, leading to an increase of the scattering probability between the edges. As a result, the longitudinal resistance reaches a maximum, while the Hall resistance increases by a step until it reaches the following plateau.

The QHE is observed to be particularly pronounced if the separation of Landau levels is significantly larger than the broadening of Landau levels, which is the case in the presence of large magnetic fields. In this regime, $\omega_c \tau_q \gg 1$ applies [45].

2.1.4 Transition from classical transport to Landau quantization

Finally, the intermediate range of magnetic fields, typically given at several hundred mT, where Drude-dominated transport transforms into quantized QHE-dominated transport will be discussed. In this regime, we observe a modulation of the density of states, which is manifested in SdH-type oscillations instead of fully developed peaks and minima in the longitudinal resistance decreasing up to zero. We can imagine the broadened peaks as being close to each other, leading to an overlap, which is illustrated in Fig. 2.7. Thus, in this regime, the conductivity is determined by two components: the Drude component and the oscillatory component. The oscillatory component gives rise to oscillations in the DOS with non-zero minima, as illustrated in Fig. 2.7.

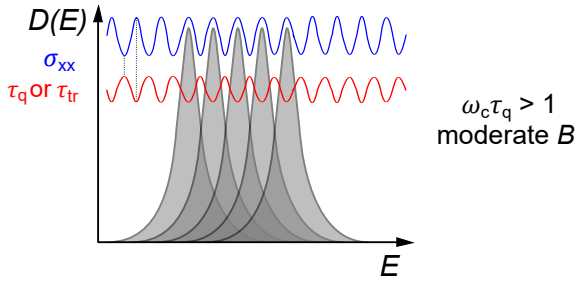

Fig. 2.7: Transport in intermediate magnetic fields: Modulation of the DOS in dependence of energy. The overlap of broadened peaks leads to a non-zero DOS, therefore transport is possible and the ρ_{xx} signal does not reach zero. Here, SdH-type conductivity oscillations begin to appear (illustrated in blue). In order to derive the behavior of the conductivity σ_{xx}, we consider τ_q (red): the DOS is proportional to the scattering rate τ_q^{-1} [45], which in turn is the inverse of τ_q. Therefore, τ_q shows an inverse behavior with respect to the DOS. Since τ_0 is inversely proportional to σ_{xx} (see Eq. 2.8), it behaves in the opposite way as σ_{xx} does. It follows that σ_{xx} acts analogously to the DOS, i.e., maxima in the DOS lead to maxima in the conductivity. Adapted from [45, 60].

In order to conclude the distinction of the different transport regimes, i.e., from

small (classical) over moderate to strong (quantizing) magnetic fields, a consideration of the lifetime quantity τ_q is useful. Within the semiclassical Drude description, a transition from classically weak to classically strong magnetic fields occurs at $\omega_c\tau_0 = 1$. For $\omega_c\tau_0 \ll 1$, i.e., for small magnetic fields, the electrons cannot complete a cyclotron orbit without being scattered. In the opposite case $\omega_c\tau_0 \gg 1$, i.e., for large magnetic fields, this is well possible. For the description of intermediate B fields, τ_q is particularly useful. In this case, $\omega_c\tau_q > 1$ applies, which means that the distance between neighboring Landau peaks is larger than their broadening width. The distance increases with increasing B. To recapitulate, the quantum lifetimes are distinguished in Tab. 2.1 for the different regimes in quantum transport.

transport regime	classical (small B)	moderate B	quantizing B
quantum lifetime relation	$\omega_c\tau_q < 1$	$\omega_c\tau_q > 1$	$\omega_c\tau_q \gg 1$
appearing effect	Hall effect	SdH oscillations	QHE

Tab. 2.1: Quantum transport regimes: quantum lifetime τ_q relations and appearing characteristic transport effects for different transport regimes [60].

2.1.5 Dispersion of different charge carrier types

We will now discuss the different possible dispersion relations shown by different types of charge carriers. They depend on the underlying symmetry and effective mass of the carriers in the material. In general, two types of dispersion appear, a parabolic one and a linear one. In experiment, our system demonstrates characteristics of both, parabolic and linear, dispersions. In the following, we explain the nature of parabolic and linear dispersions and their influence on the Landau levels.

In a parabolic system, as is the case for holes, the energy E is proportional to the square of the momentum:

$$E(k) = \frac{\hbar^2 k^2}{2m^*}, \tag{2.30}$$

where here m^* is the effective mass [61]. The parabolic dispersion results in quantized Landau levels that are evenly spaced in a perpendicular magnetic field, with energy levels that vary linearly with the magnetic field strength. This behavior is illustrated for a model system in Fig. 2.8 (a). Each Landau level has a two-fold spin degeneracy ($g_s = 2$). When spin splitting (such as from the Zeeman effect) is weak or absent, each Landau level accommodates electrons with two directions of spin. However, if the magnetic field is strong enough to cause significant spin splitting, only one spin state fills each level, leading to odd filling factors, as each level fills individually.

In contrast, massless Dirac particles possess a linear energy–momentum relationship:

$$E(k) = \hbar v_F |k|, \tag{2.31}$$

where v_F is the Fermi velocity. This relation emerges from the relativistic Dirac equation. A linear dispersion is applicable to systems with massless or nearly massless charge carriers, such as Dirac fermions in graphene [62], as well as for surface states of topological insulators, which is the aspect that is particularly pertinent to this investigation.

In a magnetic field, the Landau level energies for Dirac particles are proportional to $E \propto \sqrt{nB}$, where n denotes the Landau quantum number $n = 0, \pm1, \pm2, ...$ This relation leads to non-equidistant spacing of Landau levels (see Fig. 2.8 (b)). In graphene, filling factors exhibit a step-like behavior, with jumps occurring in increments of four. This phenomenon arises from the four-fold degeneracy of Landau levels, taking into account the spin and valley degeneracy. Consequently, filling factors in the sequence of the QHE are usually observed to be even (e.g. $\nu = 2, 6, 10, ...$) [7, 63]. In GaAs-based systems, valley degeneracy g_v is absent for fundamental reasons tied to their electronic structures. For HgTe, however, valley degeneracy ($g_v = 4$) is expected to be found in the valence band [64]. To date, this has not been confirmed in experiment.

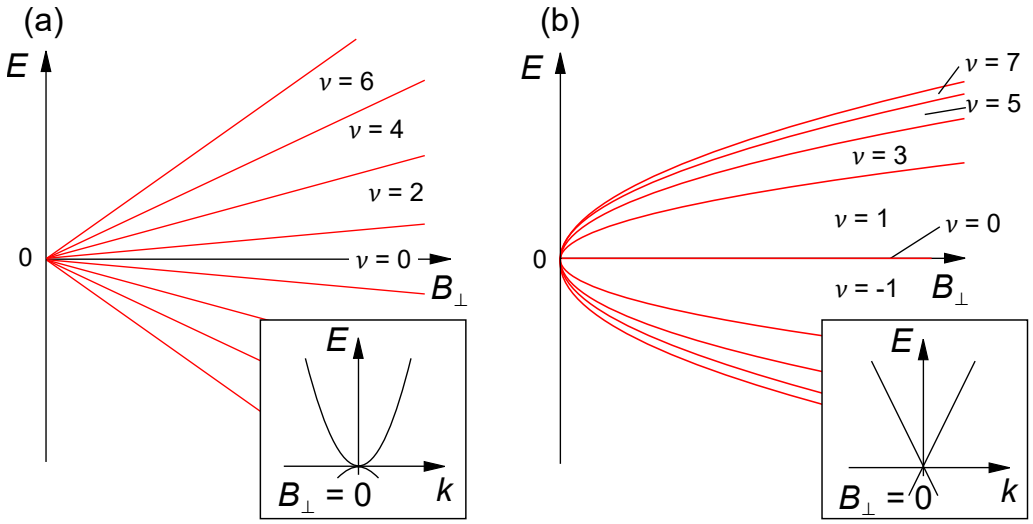

Fig. 2.8: Energy spectrum (E vs. $B_\perp$) for the simplest model system without a band gap, in order to compare the parabolic and linear dispersion laws: (a) Charge carriers with parabolic dispersion (for $B_\perp = 0$, see inset). Note that the distances between neighboring Landau levels are equidistant. In real systems, a gapless parabolic system is rare. It can be found in bilayer graphene [65]. (b) Dirac particles. The dispersion relation is linear (see inset). Note that the spacing between neighboring filling factors decreases as ν increases. In (b), a model Dirac system without taking valley degeneracy into account is shown. For graphene, we would have to take into account valley degeneracy. In both cases illustrated, we consider the spin-degenerate case, i.e., not taking Zeeman splitting into account. Adapted from [60].

Another distinguishing feature between parabolic and Dirac systems, apart from the dispersion relation and the resulting energy spectra, is the Berry phase ϕ. It denotes the phase of a parameter of the Hamiltonian acquired over the course of a cycle, and is also called the geometric phase [66]. It is $\phi = 0$ for parabolic systems, and $\phi = \pi$ for Dirac systems. In [67], a phase $\phi = \pi$ was shown for 3D TI HgTe, indicating Dirac behavior. The Berry phase will be discussed later in more detail in the context of topological insulators in Sec. 2.20.

2.2 Quantum point contacts (QPCs)

In mesoscopic physics, ballistic transport denotes the unimpeded transport of charge carriers over long distances in a material, without significant influence of scattering events. Ballistic transport is observed in samples of high quality, in which the electron (or hole) mean free path is large compared to the length and width of the channel. An ideal medium for observing ballistic transport are quantum point contacts (QPC). The conductance of a QPC is then quantized in units of 2 e^2/h, the so-called conductance quantum, proving quantization of ballistic conductance. Hence, a QPC can be considered an ideal quantum wire.

A QPC is a narrow constriction between two wide electrically conducting regions. In order to observe the quantization, the width of the channel must be comparable to the Fermi wavelength of the electrons, and the temperature must be low compared to the characteristic energy spacing of transverse modes in the channel. QPCs are well-known in split-gate technology, which is based on electrostatic definition. The number of transmitted modes is governed by the depletion of the 2DEG below the split gate, illustrated in the inset of Fig. 2.9. The 2DEG below the gate can be completely depleted by applying a gate voltage. The electrons can only pass through the narrow channels between the gates, the QPC. The first realization of a QPC in split-gate geometry showing quantized conductance was achieved in GaAs/AlGaAs heterostructures in the works of van Wees et al. [18] and Wharam et al. [19], both in 1988. QPC systems have been studied in various material systems since then, such as InAs/AlSb [68], Si/SiGe [69], or InSb [70]. The conductance quantization in QPCs is closely related to the quantization of the Hall conductance, but is measured in the absence of a magnetic field. More recently, QPCs were realized in the 2D topological insulator HgTe, where the response of topological states in combination with edge states emerging from a quantizing B-field was observed [8].

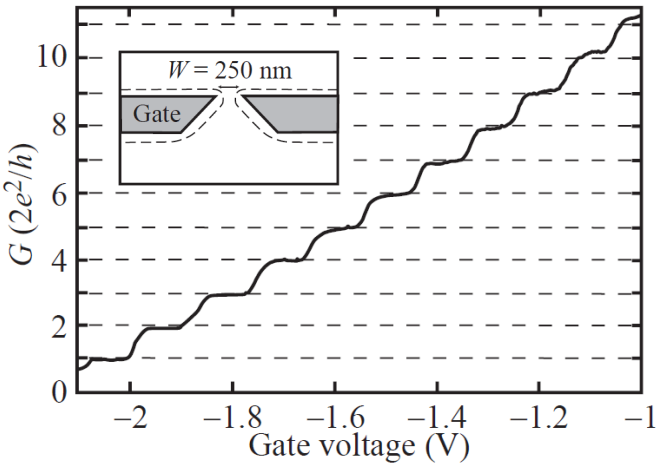

Fig. 2.9: Quantized conductance of a quantum point contact as a function of gate voltage, at $B = 0$ [18]. Conductance values in units of $2\frac{e^2}{h}$ were observed. The inset shows a schematic top view of the split-gate GaAs/AlGaAs structure. Taken from [45].

In order to understand the phenomenon of conductance quantization, we consider the simple model of a perfect one-dimensional channel. We assume the channel to be very long compared to its cross-section, so that it can be treated as translationally invariant in x-direction. This situation is illustrated in Fig. 2.10 (a). To accurately describe the conductance through the constriction, the transition between the large 2D reservoir and the wire structure (in both directions, i.e., for electrons moving from left to right, and vice versa) is considered.

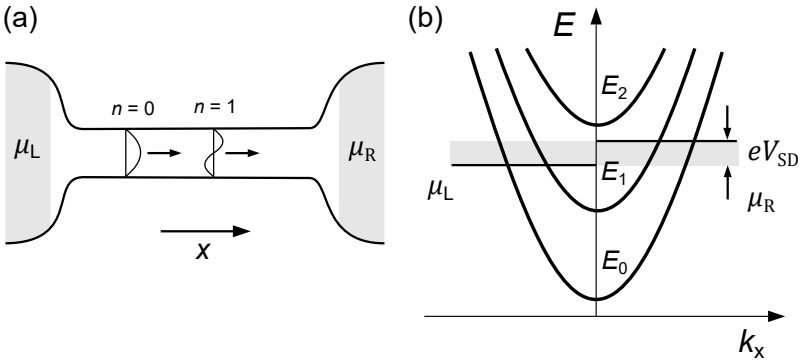

Fig. 2.10: (a) One-dimensional channel connected to left and right electron reservoirs (gray) with electrochemical potentials μ_L and μ_R. Transverse modes are drawn schematically within the channel with arrows indicating their propagation direction. (b) Dispersion relation in the 1D channel. For each mode n, the parabolic dispersion relation has its minimum at energy E_n. States with positive k_x propagate from left to right and are fed from the right reservoir with electrochemical potential μ_R, and vice versa. The gray-shaded energy interval is determined by the applied bias voltage V_{SD} between left and right reservoirs. Adapted from [45].

We assume a parabolic energy dispersion, as shown in Fig. 2.10 (b), along the QPC with

$$E_n(k_x) = E_n + \frac{\hbar^2 k_x^2}{2m^*}, \tag{2.32}$$

where E_n are energy contributions originating from mode quantization normal to the wire axis (dependent on k_y and k_z). The difference between this and Eq. (2.1), which described a 2DEG, is that the former has one fewer degree of freedom in movement. Accordingly, the number $n = 1, 2, 3, ...$ refers to the modes of the quantum wire. Positive values of k_x denote states propagating from left to right, negative ones vice versa. If the left and right electron reservoirs are not in thermodynamic equilibrium, as is the case if a voltage is applied between them via an external voltage source, a net current will flow. We introduce the net current produced by an electron between the chemical potentials μ_L and μ_R of the left and right reservoir, respectively. The distribution functions $f_i(E)$ for left- and right-moving electrons will differ, leading

to a net current

$$I = g_s \frac{|e|}{h} \sum_n \int_{E_n}^{\infty} dE |f_L(E) - f_R(E)|, \tag{2.33}$$

where the indices L and R refer to the left and the right reservoirs. The functions $f(E)$ correspond to the Fermi–Dirac distribution

$$f_i(E) = \frac{1}{\exp(\frac{E-\mu_i}{k_B T}) + 1}. \tag{2.34}$$

Assuming that the applied voltage difference V_{SD} is small, i.e., $\mu_L - \mu_R = |e|V_{SD} \ll k_B T$, we can expand

$$f_L(E) - f_R(E) = \frac{\partial f_L}{\partial \mu_L}(\mu_L - \mu_R) = -\frac{\partial f_L}{\partial E}|e|V_{SD}. \tag{2.35}$$

Inserting this into Eq. (2.33) and integrating the energy yields

$$I = g_s \frac{e^2}{h} \sum_n f_L(E_n) V_{SD}. \tag{2.36}$$

As a result, we obtain the quantization of the conductance of an ideal one-dimensional channel, where in the limit of zero temperature, the conductance becomes the step function

$$G = \frac{I}{V_{SD}} = g_s \frac{e^2}{h} \sum_n f_L(E_n) \quad \overset{0\mathrm{K}}{=} \quad g_s \frac{e^2}{h} N, \tag{2.37}$$

with $N = 1, 2, 3...$ the number of occupied modes. This number is in agreement with Eq. (2.29), yielding the quantized Hall resistance values. This expression for G reproduces the curve shown in Fig. 2.9, which depicts the original measurement of the quantized conductance (with $g_s = 2$) [18].

2.2.1 The adiabatic approximation

In the previous discussion, we have assumed a translationally invariant wire. However, this assumption is not compatible with connecting the QPC to large reservoirs which breaks translational invariance. In the experiment, the length of the electron channel is comparable to its width, and the edges that define the length of the channel are smooth. A more realistic description of conductance quantization, the so-called adiabatic approximation, implying smoother edges, must be considered [71]. In general, two types of device realization can be distinguished. A gradual confinement of the 2DEG to a 1D constriction is described as an adiabatic QPC [71], while a sharp confinement is referred to as an abrupt or sharp constriction [72]. The advantage of the adiabatic approach is related to the smooth variation of the constriction width, which enables a reflectionless matching of electron states within the transition area between the 2D reservoirs and the 1D constriction. QPC devices using the split gate

approach as well as etched constrictions that utilize wet chemical etching can both be assumed to be adiabatic. Within this model, we suppose that the transition from the macroscopic electron reservoirs (gray regions in Fig. 2.10 (a)) into the wire is very smooth (in the sense of not being hindered in transport by sharp edges) on the scale of the Fermi wavelength λ_F. Hence, we are treating a quasi-1D system. The electron then experiences the effective potential

$$V_n^{\text{eff}}(x) = E_n(x). \tag{2.38}$$

The effective potential depends on the mode index n, meaning that the potential barrier seen by an electron traveling through the QPC depends on the transverse mode of its wave function. Fig. 2.11 (a) shows an example of an adiabatic hard-wall confinement potential in the x-y-plane. The corresponding $V_0^{\text{eff}}(x)$ is shown in Fig. 2.11 (b). The closer the electron approaches $x = 0$, the narrower the channel gets and the larger is $V_0^{\text{eff}}(x)$. By that, in the adiabatic approximation, the original quantum wire geometry reduces to a one-dimensional potential barrier problem.

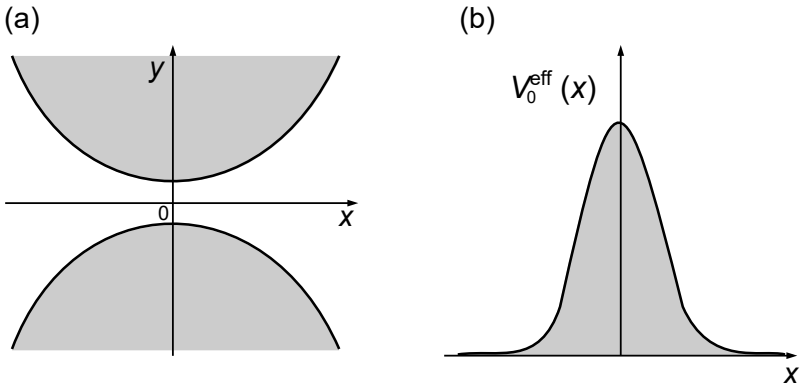

Fig. 2.11: The adiabatic QPC: (a) A hard-wall confinement potential in the x-y-plane forming a quantum point contact. Electron transport occurs in x-direction; gray-shaded areas are forbidden for electrons. (b) Effective potential barrier $V_0^{\text{eff}}(x)$ of the QPC in x-direction in the adiabatic approximation. Adapted from [45].

So far, the adiabatic approximation was general in the sense that no specific form of the potential $V(x, y, z)$ was assumed. From now on, we will assume the saddle point potential, typical for split-gate QPC systems, given by

$$V(x, y, z) = -\frac{1}{2}m^*\omega_x^2 x^2 + \frac{1}{2}m^*\omega_y^2 y^2 + V(z). \tag{2.39}$$

Here, ω_x and ω_y denote the oscillation frequency defined by the spacing between the subbands in x- and y-direction, respectively. It is given by the confinement in the corresponding direction.

A closer analysis of Eq. (2.37) indicates that the QPC conductance should exhibit a sudden, step-like increase as the gate voltage changes. This is because in a classical

QPC, by applying a gate voltage, the effective width is varied, which leads to a change in the number of transmitted modes. However, experimental data from QPC samples consistently show a smoother transition between successive conductance plateaus. To account for this discrepancy, it is essential to consider the effects of quantum mechanical transmission and reflection through the potential. This is done by using the Wentzel-Kramers-Brillouin (WKB) approximation. Applying the latter to the scenario discussed results in a transmission probability $T_n(E)$ for every individual subband. The transmission of a mode n through a parabolic potential barrier in x-direction is then given by

$$T_n(E) = \frac{1}{1 + \exp(-2\pi\epsilon_n)}, \tag{2.40}$$

with the energy parameter of each electron

$$\epsilon_n = \frac{E - \hbar\omega_y(n + \frac{1}{2}) - E_z}{\hbar\omega_x}. \tag{2.41}$$

If the electron has enough energy to overcome the effective barrier, i.e., $E > V^{\text{eff}}(0)$, then the transmission probability is close to one. Otherwise, the electron is reflected in the vicinity of $x = 0$, where $E = V^{\text{eff}}(x)$, and the transmission probability is close to zero. Now, it is possible to extend the 1D conductance formula (see Eq. (2.37)) to quasi-1D systems (= adiabatic systems). Since every transverse mode provides a 1D transport channel with potential barrier $V^{\text{eff}}(x)$ and transmission probability $T_n(E)$, the total conductance is given by the sum of all contributions to transport in the channel. At very low temperatures, the derivative of the Fermi–Dirac distribution approximates a δ-function so that the transmission does not change within a few k_BT around the Fermi energy. $T_n(E)$ is then roughly constant within the corresponding energy window and can be replaced by the transmission probability T_{mn} from mode n into mode m at energy E. Adjusting Eq. (2.37) results in the Landauer formula

$$G = g_s \frac{e^2}{h} \sum_{m,n} T_{mn}(E). \tag{2.42}$$

Fig. 2.12 shows the calculated transmission probability through the potential for the first three modes ($n = 0, 1, 2$). The Landauer formula represents the fundamental law of mesoscopic transport physics, which is the relation between conductance and transmission probabilities at the Fermi energy.

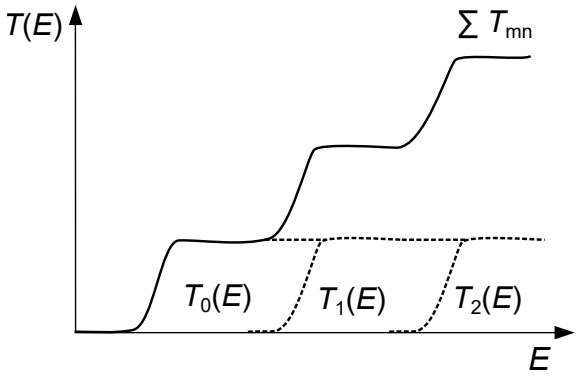

Fig. 2.12: Transmission of individual modes and total transmission, composed of the transmission probabilities $T_{mn}(E)$ from each mode n into mode m at energy E, according to the Landauer formula (see Eq. (2.42)). Here, we consider the the saddle point model for the quantum point contact. Adapted from [45].

2.2.2 One-dimensional transport in perpendicular magnetic fields

So far, we have either considered transport in magnetic fields in two dimensions, or in one dimension without taking magnetic fields into account. We will now discuss transport in one dimension in perpendicular magnetic fields. In the following, we consider the well-known QPC system defined via depletion of the 2DEG, as is the case in GaAs/AlGaAs-based heterostructures [45]. The solution presented here can be found in more detail in [73, 74]. Applying an external magnetic field $B_\perp$, perpendicular to the device plane, i.e., in z-direction, modifies the energy dispersion inside the constriction. Previously, we assumed a harmonic confinement potential in y-direction, with free motion in x-direction. For the moment, we will neither take SOI nor Zeeman splitting into account. The single-particle Hamiltonian of the QPC when adding an external magnetic field can then be expressed in the Landau gauge $A = (By, 0, 0)$ as

$$H_0 = \frac{1}{2m^*}(p_x^2 - eBy)^2 + V(y). \tag{2.43}$$

For the confinement of the QPC, we again choose a parabolic potential, which is comparable to the conditions given by wet-chemically etched hard-wall potentials, as assumed in our system:

$$V(y) = \frac{1}{2}m^*\omega_y^2 y^2. \tag{2.44}$$

With the ansatz

$$\Psi(x, y) = \phi(y)\exp(ik_x x), \tag{2.45}$$

the Hamiltonian transforms into

$$H_0 = -\frac{\hbar^2}{2m^*}\frac{d^2}{dy^2} + \frac{1}{2}m^*\omega^2(y - y_0)^2 + \frac{\omega_y^2}{\omega^2}\frac{\hbar^2 k_y^2}{2m^*}, \tag{2.46}$$

with the effective oscillator frequency $\omega^2 = \omega_y^2 + \omega_c^2$ and the quantity $m^*\left(\frac{\omega}{\omega_0}\right)^2$, which can be interpreted as an effective magnetic mass of the 1D system. The energy eigenvalues E_n of the resulting hybrid (magnetic and electronic) 1D subbands are given by [73]

$$E_n = \hbar\omega\left(n + \frac{1}{2}\right) + \frac{\hbar^2}{2m^*}\frac{\omega_0^2}{\omega^2}k_y^2. \tag{2.47}$$

At this point, two contributions to the energy of each subbands remain: the cyclotron energy (dependent on $B_\perp$), which results in constant flat bands, and the parabolic dispersion stemming from the confinement, influenced by the effective mass, which also depends on the magnetic field.

An increasing external magnetic field therefore leads to increased 1D subband separation due to a larger ω, as the 1D subbands become successively depopulated. Additionally, the effective mass of the electrons m^* is increased, which leads to a flattening of the subbands. In the limit of a strong perpendicular magnetic field, the hybrid magneto-electronic subbands evolve into magneto-subbands, i.e., the Landau levels. The evolution of the 1D subband dispersion with increasing $B_\perp$ is schematically depicted in Fig. 2.13. Due to the increased 1D subband spacing, the application of $B_\perp$ in 1D transport measurements generally leads to an improvement in ballisticity within the constriction, as backscattering is reduced.

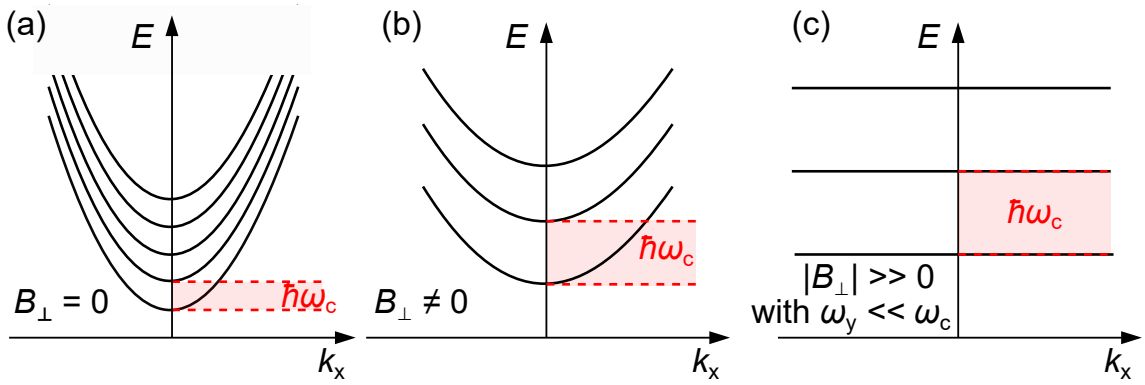

Fig. 2.13: Transport in a perpendicular magnetic field. Development for increasing magnetic fields, starting at $B_\perp = 0$. (a) Parabolic dispersion without the influence of a magnetic field. The subband position is determined by the confinement only. Hence, the spacing between the subbands is still small, as Landau quantization is not present. The latter is induced by magnetic fields. (b) As $B_\perp$ is applied and increases, the subbands become more flat, and the spacing between them increases due to larger cyclotron energy. (c) For strong magnetic fields, for which $\omega_y \ll \omega_c$ applies (with ω_y the frequency defining the spacing between the subbands), the Landau bands are completely flat because of the high effective mass dependent on $B_\perp$. The cyclotron energy subband spacing is even more increased. Adapted from [74].

2.3 Splitting of Landau levels

As we will consider terms of spin-orbit coupling and Zeeman splitting in the simulations modeling the experimental results, we briefly introduce the most relevant aspects of spin-orbit interaction and the Zeeman effect.

2.3.1 Zeeman effect

In semiconductor physics, the Zeeman effect describes the lifting of the degeneracy of spin states by the magnetic field. Charge carriers, which possess a spin and magnetic moments, interact with the magnetic field, leading to an energy shift given by [45]

$$\Delta Z_{\pm} = \pm\frac{1}{2} g \mu_B B_{\text{total}}, \tag{2.48}$$

with the Landé g-factor, μ_B the Bohr magneton, and $\pm 1/2$ the spin quantum number s. Hence, this Zeeman splitting energy is proportional to the magnitude of the magnetic field B_{total} (simplified to B throughout this thesis, unless otherwise specified or stressed). This energy shift causes spin-up and spin-down states to differ in energy, leading to the observable Zeeman splitting. The total Zeeman energy is defined by the sum of the two branches of the Zeeman splitting with $s = +\frac{1}{2}$ and $s = -\frac{1}{2}$, adding to

$$\Delta Z = \Delta Z_{+} - \Delta Z_{-} = g \mu_B B. \tag{2.49}$$

The g-factor describes how strongly a particle couples to a magnetic field. So far considered for a free particle, however, it has to be adapted to a particle which is bound in a semiconductor material. In atomic physics, the g-factor is composed of the total electronic angular momentum J, the spin angular momentum S and the orbital angular momentum L according to the Landé formula [55]. For electrons bound in a material, however, their effective mass has a major influence on the band structure, and, therefore, on the g-factor [45]. This leads to the emergence of spin-orbit interaction, which initiates a renormalization of the free-electron g factor, the so-called effective g^*-factor. It should not be confused with the spin degeneracy factor g_s, introduced in Sec. 2.1. For the free electron in vacuum, the Landé g factor is $g = 2$. For a bound electron in HgTe, the effective g^*-factor can reach values of up to $g^* = 80$ [75]. Apart from the aforementioned spin-orbit interaction, it can strongly depend on the magnetic field, but also the quantum confinement or strain. The influence on g^* will be discussed in more detail in Sec. 6.3.

As discussed previously in Sec. 2.1.3, in a 2DEG, the Landau quantization arises from the electron cyclotron motion, which depends only on the magnitude of ($B_{\perp}$). The latter affects the circular trajectory of the electron in the plane. Conversely, the Zeeman splitting, responsible for lifting the spin degeneracy, depends on the total magnetic field (B_{total}), including both perpendicular $B_{\perp}$ and parallel $B_{\parallel}$ components.

Thus, tilting the magnetic field while keeping $B_\perp$ constant increases the total field and enhances the Zeeman splitting without affecting the Landau quantization directly.

In total, if we take the Zeeman splitting of electronic levels into account, the Zeeman energy $\Delta Z_\pm$ is added to the quantized energy levels E_n, and we obtain an energy spectrum including the magnetic quantization:

$$E = E_n \pm \Delta Z_\pm = \hbar\omega_c(n + \frac{1}{2}) \pm \frac{1}{2} g^* \mu_B B_{\text{total}}, \tag{2.50}$$

with the adapted effective g^* factor and E_n according to Eq. (2.26), which includes the term for the cyclotron energy $\hbar\omega_c$. k-dependent terms are not included here, as they do not have an impact on the splitting. In summary, at sufficiently large magnetic fields, in which the effect is not hidden by the broadening of Landau levels, we observe Zeeman splitting, scaling with the total B field. It is also given in particular in the case of rotating the device under study, where one has to introduce an additional in-plane magnetic field component $B_\parallel$. The resulting energy splitting at different magnetic field strengths is visualized in Fig. 2.14.

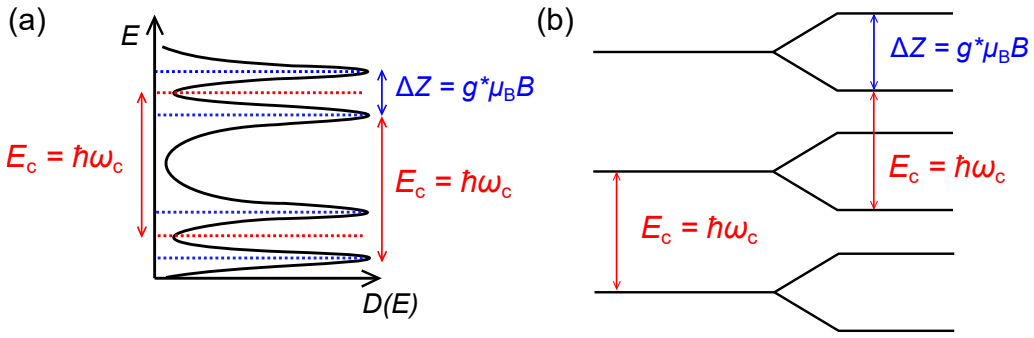

Fig. 2.14: (a) Density of states for electrons in a magnetic field. If we consider the non-degenerate case, where $B = 0$, the energy separation is $E_c = \hbar\omega_c$ (highlighted in red), with no splitting of the energy states. In the case of $B \neq 0$, where Zeeman splitting (highlighted in blue) takes place, the degenerate DOS peaks have still an energetic separation of the cyclotron energy $E_c = \hbar\omega_c$ with respect to every second peak, as the other peak arises from the spin splitting. In the present case, we assume that the Zeeman splitting is smaller than the cyclotron energy $\Delta Z < E_c$. Adapted from [45]. (b) Energy splitting diagram with qualitative layout of spin levels for $\Delta Z < E_c$. For HgTe in particular, the ratio $E_c/\Delta Z$ can vary strongly. Adapted from [76].

2.3.2 Spin-orbit interaction

An electron moving in an electric field with a certain velocity $\vec{v}$ generates a magnetic field in its frame of reference according to $\vec{B}_{\text{eff}} = \frac{\vec{v}}{c^2} \times \vec{E}$. In atoms, this effect manifests itself in the splitting of the energy levels known as the fine structure. In classical 2D systems, the spin-orbit interaction (SOI) is responsible for linear spin-dependent shifts of the momentum-dependent energy $E(k)$. In this way, the spin degeneracy of the dispersion relation is lifted with respect to k (which is in contrast to the Zeeman splitting, where the shift is with respect to the energy E). The defining aspect of SOI is that, even in the absence of an externally applied magnetic field, electrons moving in an electric field experience a magnetic field in their frame of motion - the spin-orbit field [77].

In the system under study, SOI helps to understand the behavior of the surface states. In the present case, transport is characterized by topological surface states, which behave in the same way as spin-helical states in systems with SOI in classical 2DEG systems (e.g., InAs/GaAs). In such helical systems, up-spins propagate in one direction, while the down-spins propagate into the other [46]. Because of this analogy, we will introduce the origin and mechanism of Rashba SOI, which will be utilized in the theoretical model to describe the experimental observations.

In general, two types of SOI are distinguished, Dresselhaus and Rashba SOI. For both effects to become important, a huge effective mass and a small electron density (small k_F) are of advantage [45]. We will briefly introduce both types in the following, but focus on Rashba SOI. For detailed information, see Refs. [78–81]. Dresselhaus SOI occurs in bulk crystals with bulk inversion asymmetry (BIA), depending on the crystal symmetry (such as zinc-blende structures). The Dresselhaus coefficient β_D is given by the band structure parameters of the material and by the thickness of the electron gas in the growth direction, with the Dresselhaus coefficient

$$\beta_D = \beta \frac{\pi}{h^2}, \tag{2.51}$$

with β being a material-specific constant, which describes the magnitude of the BIA-induced splitting, and h being the width of the potential well. Narrow wells (small h) result in large values, wide wells (large h) in smaller ones. In the system under study, with relatively large h, the Dresselhaus effect is expected to be relatively small. Moreover, the exact Dresselhaus SOI contribution remains unknown to date for HgTe [82].

Rashba SOI, by contrast, is caused by a confinement potential in heterostructures with structural inversion asymmetry (SIA). In particular, it occurs in epitaxially grown structures with an asymmetry of the distribution of the electric field normal to the plane of the two-dimensional electron gas. The strength of the SIA-induced splitting can be controlled by the latter. The Rashba coefficient α_R is then given by

$$\alpha_R = \alpha E_z, \tag{2.52}$$

with α a material-specific constant, which describes the magnitude of the SIA-induced splitting, and E_z being an electric field in the z-direction. The electric field can be achieved by applying a gate voltage. The dispersion relation (for parabolic systems) including Rashba SOI is then given by

$$E_{\mathrm{SO}} = \frac{\hbar^2 k^2}{2m^*} \pm \alpha_R \cdot k, \tag{2.53}$$

with $k = \sqrt{k_x^2 + k_y^2}$. It leads to spin splitting of the electron states. The two branches of the dispersion are still parabolic as in the initially assumed potential of the ideal quantum wire (see Eq. (2.32)), but their minima are shifted in k compared to the spin-degenerate dispersion by $\pm m^* \alpha_R / \hbar^2$. This shift is sketched in Fig. 2.15 (a). Rashba SOI induces an energy splitting originating in the spin. The effect occurs when an electron moves through an asymmetric potential, such as an electric field perpendicular to a 2DEG or surface. The resulting SOI aligns spin with momentum, leading to a spin-momentum locking effect, illustrated in Fig. 2.15 (b). The effect is particularly large in topological insulators, because the topological surface states are very sensitive to the interfaces. The effect of spin-momentum locking will be further discussed in Sec. 2.20. In HgTe quantum wells with an inverted band structure, the Rashba spin splitting energy can reach values up to 30 meV [83]. For further reading on Rashba SOI, see [84].

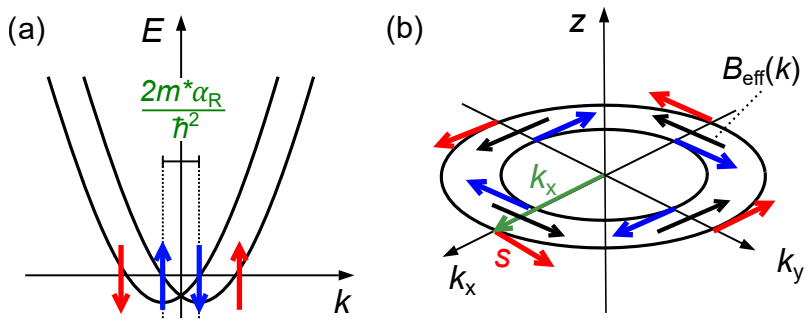

Fig. 2.15: Schematic of Rashba spin-orbit interaction: (a) Band structure with splitting of the subband and a resulting lifting of the degeneracy due to a shift in k. The arrows indicate that the spins become momentum-dependent (blue for inner arrows, red for outer arrows). (b) Distribution of spin orientations at the Fermi energy. k_x vs. k_y is plotted, showing the slice of k-space at $E = 0$. The SOI produces an effective magnetic field B_{eff} (black arrows). The spin directions s align in parallel or antiparallel orientation towards B_{eff} and form the inner and outer Fermi circle. Adapted from [84, 85].

Fig. 2.16 summarizes the relevant influences on the energy bands and the Landau fan pattern, starting from the unperturbed system with the energy dispersion shown in panel (a): The effect of a magnetic field on the energy dispersion is sketched, either resulting from an external magnetic field (see Eq. 2.48) as shown in panel (b), or from an internal effective magnetic field caused by SOI (see Eq. 2.53), shown in panel (c). The expected Landau fans in the $(E(V_g), B_{\mathrm{total}})$-parameter space are illustrated in panels (d)-(f) for each system, correspondingly.

While panel (e), which shows the Zeeman-split Landau fan chart, displays a linear, two-fold splitting of each Landau level with increasing magnetic field, the pattern resulting from SOI-induced splitting in panel (f) appears different. In this self-developed model [60], we can approximate the energy bands with two parabolas, originating from slightly different origins, representing two groups of spin non-degenerate electrons with the same effective mass, but different charge carrier density. The energy difference between the origins of the parabolas E_0 reflects the magnitude of Rashba splitting. Such an approximation allows us to reconstruct the behavior of Landau levels at energies much higher than E_0, which helps to predict the crossing of Landau levels and explain the beating pattern of SdH oscillations observed in two-dimensional systems with Rashba splitting [83, 86, 87].

In our system, top and bottom surface electrons could be treated as a Rashba-like system, however, the significant difference between the densities of top and bottom surface states makes the formation of a beating pattern impossible. Furthermore, a mixture of both types of splitting, SOI-type and Zeeman splitting, can be expected. For simplicity, we focus on parabolic systems in Fig. 2.16. However, we should keep in mind that our system contains also characteristics of linear Dirac systems, making the real dispersion more complicated. It should also be emphasized that the topological nature of the material yields a much stronger contribution than real spin-orbit coupling, and, as stated in the beginning, we only use Rashba-type SOI to describe our experimental findings, rather than taking into account real Rashba SOI.

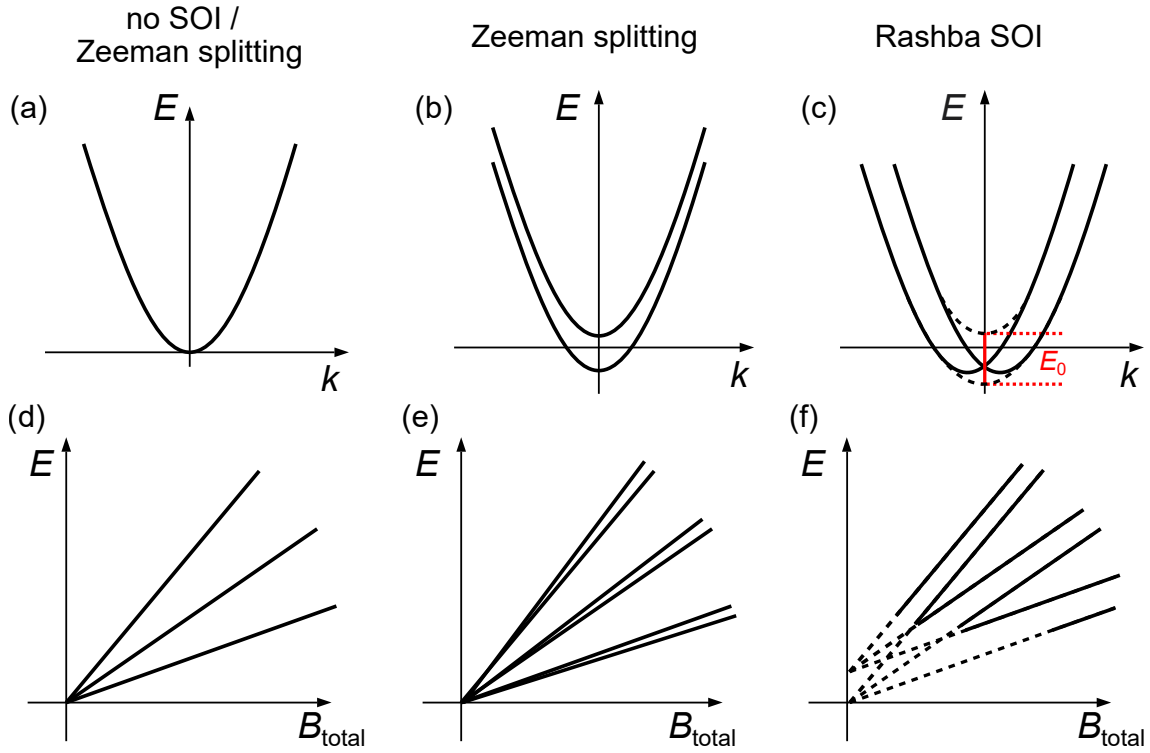

Fig. 2.16: Effect of Zeeman and Rashba splitting on dispersion of parabolic systems. (a) The degenerate band structure with a parabolic dispersion is shown. (b) Zeeman splitting: the energy band is split into subbands shifted with respect to energy. The Zeeman splitting is proportional to the magnetic field. (c) Rashba SOI. A splitting with respect to k takes place. The dashed lines represent virtual parabolas in a simplified model, belonging to two electron subsystems of different density. E_0 (red) denotes the difference in the Fermi energies between the subsystems. E_0 is determined by the structure inversion asymmetry (for example, given by the gate voltage) and does not depend on an externally applied magnetic field. (d)-(f): Corresponding Landau fan diagrams. (d) A linear dependence with equidistant spacing between the Landau levels is given in pure parabolic systems without implying SOI or the Zeeman effect. (e) The Landau levels split in linear proportion to $g^*\mu_B B$. (f) While the real behavior of the Landau levels in Rashba systems is complicated, it can be simplified in accordance to the model introduced in panel (c). Each parabola generates its own set of Landau levels, shifted by E_0. Such a simplification could be used at energies higher than E_0 and allows to describe the experimental data. Adapted from [60].

2.4 Topological insulators

Topological insulators (TIs) are a class of materials in which an energy gap separates the valence band from the conduction band as in ordinary insulators, but surface or edge states exist that close the band gap. These surface states are protected by time-reversal symmetry [46]. In this section, we review the concept of topology in condensed matter physics with a focus on the 3D topological insulator (3D TI) HgTe. Signatures of topological properties in 3D TI HgTe were displayed in [67]. Unlike in HgTe-based 2D TI QPCs [8], possible quantization effects in their 3D counterparts have not yet been achieved. At this point, it should be mentioned that the effect of conductance quantization, which is the main matter of this thesis, is however not associated with the concept of TIs in particular. The concepts reviewed in this section closely follow the theory of TIs presented in Ralf Fischer's doctoral thesis [47], which can be highly recommended as further reading, especially with regard to further concepts for understanding Majorana bound states.

2.4.1 Topology in condensed matter physics

Topology, a branch of mathematics, classifies objects based on their genus g, which represents the number of holes an object has. This quantity g shall not be confused with the g-factor (see Sec. 2.3.1). From a topological point of view, two objects share the same genus if they maintain the same amount of holes throughout being deformed. For example, a torus can be transformed into a mug by continuously deforming it without closing the hole. Therefore, they have both the genus ($g = 1$). However, a sphere has a different genus ($g = 0$) because it cannot be deformed into a torus without opening a hole [46]. The same concept can be transferred in order to classify Hamiltonians in condensed matter physics. If two Hamiltonians can be continuously deformed into each other without closing the energy gap, they are topologically equivalent. The different classes are distinguished by what is called the Chern number $n \in \mathbb{Z}$, where $\mathbb{Z}$ denotes integers. [88]. Consequently, the energy gap must close at an interface where the Chern number changes. Therefore, the presence of conducting edge or surface states at such interfaces is a fundamental consequence of the topological classification [46]. In fact, the quantum Hall state was first discovered as a topological state [89]. In this case, the electrons in a 2DEG are constricted to circular orbits if a strong magnetic field is applied perpendicular to the plane of the 2DEG. These circular orbits are quantized with the cyclotron frequency ω_c and lead to the formation of Landau levels. If a number of Landau levels are occupied, an energy gap separates the filled and empty states, just like in an ordinary insulator. Conductive edge channels form at the interface of a quantum Hall insulator and an ordinary insulator. These edge channels provoke a quantized Hall conductance $\sigma_{xy} = Ne^2/h$ [59], with $N = 0, 1, 2, 3, ...$ edge channels. In a topological description of the integer QHE, N is equal to the Chern invariant n [88]. At the

interface of a quantum Hall insulator and an ordinary insulator, with the latter described by $n = 0$, the Chern invariant is forced to change from $n \neq 0$ to $n = 0$, leading to the formation of edge channels. This situation is depicted in Fig. 2.17 (a) for $n = 1$. At the interface between the quantum Hall state and the insulating state, a single edge channel then emerges. The corresponding electronic dispersion is illustrated in Fig. 2.17 (b), the band gap being closed by a conducting edge state.

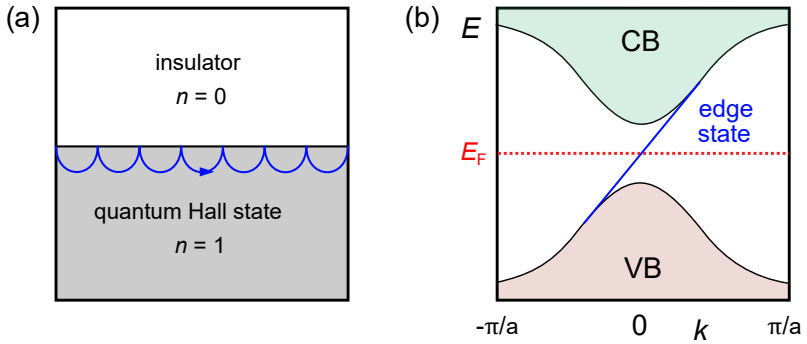

Fig. 2.17: (a) Interface of insulator and quantum Hall state. The electrons exhibit skipping orbits (blue) on the edge to close the band gap, while the Chern number n changes. (b) Electronic dispersion in the quantum Hall state. Here, an edge state connects the valence band (VB) and the conduction band (CB). Adapted from [46, 47].

Since an applied magnetic field breaks time-reversal symmetry ($\mathcal{T}$), the quantum Hall state arises exclusively in systems where $\mathcal{T}$ is no longer preserved [46, 90]. In quantum mechanics, the time reversal symmetry is represented as an antiunitary[1] operator Θ, for which $\Theta = i\sigma_y\mathcal{K}$ applies. Here, σ_y is a Pauli spin matrix[2] and $\mathcal{K}$ is the complex conjugation operator [10]. For spin 1/2 particles, it yields $\Theta^2 = -1$. It follows that the relation $\Theta H(\vec{k})\Theta^{-1} = H(-\vec{k})$ must be met by a $\mathcal{T}$-invariant Hamiltonian. However, edge states can also appear in a system without an external magnetic field applied. This applies to systems with strong spin-orbit interaction. In such systems, $\mathcal{T}$ is preserved. In fact, the edge states can even be protected by $\mathcal{T}$ [91]. In $\mathcal{T}$-invariant systems, the Chern invariant is always $n = 0$, which requires the introduction of a new $\mathbb{Z}_2$ topological number ν in order to characterize these systems. $\mathbb{Z}_2$ can adopt two possible values $\nu = 0$ and 1, which are illustrated in Fig. 2.18.

The topological invariant characterizing a 2D band structure may be constructed by imagining a long cylinder whose axis is parallel to a reciprocal-lattice vector $\vec{G}$ and which has a circumference of a single lattice constant. Then, the magnetic flux Φ threading the cylinder acts as a circumferential (or "edge") crystal momentum k_x, with the magnetic flux corresponding to two edge time-reversal invariant momenta

[1] For an antiunitary operator, $T^{-1}iT = -i$ applies, with a time-reversal operator T.

[2] The Pauli matrices are given by $\sigma_0 = \begin{pmatrix} 1 & 0 \\ 0 & 1 \end{pmatrix}, \sigma_x = \begin{pmatrix} 0 & 1 \\ 1 & 0 \end{pmatrix}, \sigma_y = \begin{pmatrix} 0 & -i \\ i & 0 \end{pmatrix}, \sigma_z = \begin{pmatrix} 1 & 0 \\ 0 & -1 \end{pmatrix}$

$k_x = \Lambda_1$ ($\Phi = 0$) and $k_x = \Lambda_2$ ($\Phi = h/2e$). The $\mathbb{Z}_2$ invariant reflects the change in the Kramers degeneracy at the ends of this 1D system between $k_x = \Lambda_1$ and $k_x = \Lambda_2$ [92].

The Brillouin zone of a 2D system has four $\mathcal{T}$-invariant momenta Λ_i, visualized as blue dots in Fig. 2.18 (a). For an edge perpendicular to the reciprocal-lattice vector $\vec{G}$, the $\mathcal{T}$-invariant momenta Γ_1, Γ_2 of the edge are projections of pairs Λ_i onto the line in perpendicular direction to $\vec{G}$ [92]. The electronic dispersion of a $\mathcal{T}$-invariant 2D insulator is illustrated in dependence of the crystal momentum k on a path connecting Γ_1 and Γ_2 in Fig. 2.18 (b) and (c). The Brillouin zone is shown for $0 < k < \pi/a$ only, with a being the lattice constant. Due to $\mathcal{T}$, the negative part can be mirrored with respect to the y-axis. The Kramers' theorem requires that all eigenstates of a $\mathcal{T}$-invariant Hamiltonian are at least twofold degenerate. [46]. Thus, if edge states are present inside the band gap, they have to be at least twofold degenerate at the $\mathcal{T}$-invariant momenta $k = \Gamma_1 = 0$ and $k = \Gamma_2 = \pi/a$. In the areas between these points, the degeneracy is lifted due to spin-orbit interaction. There are two possibilities for the states at $k = \Gamma_1$ and $k = \Gamma_2$ to connect. The first opportunity is that they connect in pairs, i.e., the Fermi energy E_F intersects the bands an even number of times (see Fig. 2.18 (b)). In this scenario, the edge states can be displaced, e.g., by strong disorder, and we obtain an ordinary insulator with $\mathbb{Z}_2$ invariant $\nu = 0$. The second opportunity is that E_F intersects the band an odd number of times (Fig. 2.18 (c)). In this scenario, in contrast, the edge states cannot be eliminated. The $\mathbb{Z}_2$ invariant is then $\nu = 1$, with the consequence that the edge states are topologically protected [5, 46, 92].

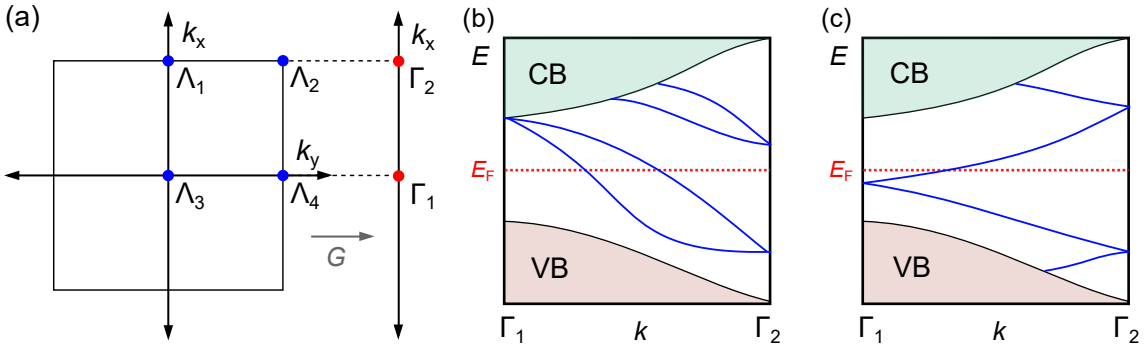

Fig. 2.18: (a) The Brillouin zone of a 2D system with four $\mathcal{T}$-invariant momenta Λ_i (blue dots). The $\mathcal{T}$-invariant momenta Γ_1, Γ_2 of an edge are projections of pairs Λ_i. The direction of the reciprocal-lattice vector G is indicated. Adapted from [5, 92]. (b) and (c): Electronic dispersion of a $\mathcal{T}$-invariant 2D insulator. In (b), the number of edge states crossing the Fermi energy E_F is even. In (c), the number is odd. An odd number leads to topologically protected edge states. Adapted from [46, 47].

2.4.2 Two-dimensional topological insulators

The aforementioned 1D topological edge states exist in particular in a quantum spin Hall insulator (QSHI), also known as a 2D topological insulator. The existence of this phase was initially proposed theoretically in graphene [91], later in HgTe/CdTe quantum wells [93], and for the latter confirmed through experiments by König et al. [7]. Since $\mathcal{T}$ is preserved, the edge states form Kramers pairs and exhibit helicity, i.e., their spin orientation determines their path of motion. Fig. 2.19 (a) illustrates this scenario, where at the interface of a QSHI and an ordinary insulator, a pair of edge channels is present. The spin-up electrons propagate to the left, while the spin-down electrons propagate to the right. On the opposite interface, the directions are inverted. As long as $\mathcal{T}$ is present, the channels are not allowed to interfere with each other [46]. The corresponding band structure of a QSHI is shown in Fig. 2.19 (b). Here, two helical edge states close the band gap by connecting the conduction and valence band.

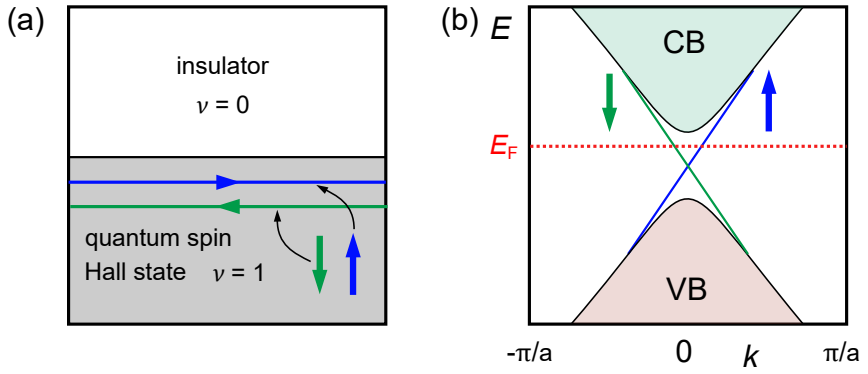

Fig. 2.19: (a) Interface between a trivial insulator and a quantum spin Hall insulator (QSHI). Since the $\mathbb{Z}_2$ invariant changes at the interface, helical edge states emerge. (b) Electronic dispersion of a QSHI. Helical edge states exist in the band gap connecting the valence band and the conduction band. Adapted from [46, 47].

2.4.3 Three-dimensional topological insulators

The concept behind the quantum spin Hall insulator can be generalized to three-dimensional systems [5]. In 3D topological insulators, two-dimensional surface states appear, replacing the edge channels found at the boundaries of 2D topological insulators. A 3D topological insulator is described by now four $\mathbb{Z}_2$ invariants, denoted as $\nu_0; \nu_1, \nu_2, \nu_3$. These invariants can be understood in a way analogous to those of the quantum spin Hall insulator. Fig. 2.20 (a) displays the Brillouin zone corresponding to a 3D topological or trivial insulator. Now, eight $\mathcal{T}$-invariant points Λ_i are present in the Brillouin zone of a 3D crystal. For a surface that is normal to the vector $\vec{G}$, the surface Brillouin zone contains four $\mathcal{T}$-invariant momenta, namely $\Gamma_1, \Gamma_2, \Gamma_3$

and Γ_4. These Γ_i points result from projecting pairs of Λ_i points onto the plane orthogonal to $\vec{G}$. Kramers' theorem ensures that the $\mathcal{T}$-invariant points at Γ_i, the so-called Dirac points, are twofold degenerate, while the degeneracy is lifted between them due to spin-orbit interaction. Again, the surface band structure resembles either Fig. 2.18 (b) or (c) for a path connecting any pair Γ_i and Γ_j. The topological properties of the system are identified by counting how many times the Fermi circle (red circle in Fig. 2.20 (b)) intersects the surface states. If the number of intersections is even, the material is classified as a weak TI. The corresponding first $\mathbb{Z}_2$ invariant is $\nu_0 = 0$. The surface states are not protected by $\mathcal{T}$ then, and can be localized in the presence of disorder. By contrast, if the Fermi surface intersects the paths connecting any pair Γ_i and Γ_j an odd number of times, $\nu_0 = 1$. Then, we obtain a so-called strong topological insulator. In this case, the surface states are topologically protected and cannot be localized. The other invariants (ν_1, ν_2, ν_3) can be interpreted as Miller indices, describing the orientation of the layer. The simplest case of a strong topological insulator is achieved when only one single Dirac point, e.g., Γ_1, is enclosed by the Fermi circle, while this point is connected to every other $\mathcal{T}$-invariant point as in Fig. 2.18 (c). Then, E_F crosses the bands an odd number of times. This situation is visualized in Fig. 2.20 (b). Here, a single surface of a 3D TI can be described by the Dirac-like dispersion

$$E = \pm\hbar v_F \sqrt{k_x^2 + k_y^2}. \tag{2.54}$$

The resulting 2D Dirac cone, describing a single surface of a 3D TI, is depicted in Fig. 2.20 (c). The peculiar property of these surface states is their non-spin-degeneracy. This is due to the fact that states at momenta $\vec{k}$ and $-\vec{k}$ must have an opposite spin due to $\mathcal{T}$. Thus, the spin rotates together with $\vec{k}$ around the Fermi circle as shown in Fig. 2.20 (c). Each state can only have one spin orientation, which always points into the perpendicular direction referred to the direction of motion. This phenomenon is known as spin-momentum locking [5, 46, 92]. A corresponding real-space picture is shown in Fig. 2.20 (d).

Spin-momentum locking leads to significant effects on the Berry phase γ_n that an electron picks up when it travels around the Fermi surface. In a more general sense, the Berry phase γ_n is the total phase of a quantum mechanical system after completing a closed path C in the parameter space, where the system returns to its starting position, i.e., where $\vec{R}(t = T)$ is equal to $\vec{R}(t = 0)$, with $\vec{R}(t)$ being a set of time-dependent parameters [94]. Mathematically, it is expressed as

$$\gamma_n = \oint_C d\vec{R} \cdot \vec{\mathcal{A}}_n(\vec{R}), \tag{2.55}$$

where n is the n-th eigenstate of the system, and $\vec{\mathcal{A}} = i\langle n, \vec{R}|\nabla_R|n, \vec{R}\rangle$ the so-called Berry connection [94]. Transferred to our system, the electron moves around a single Dirac point, causing its spin to undergo a full 2π rotation. As a result, the electron

acquires a Berry phase equal to π [95]. A Berry phase of π plays an important role in the treatment of topological insulator nanowires [67].

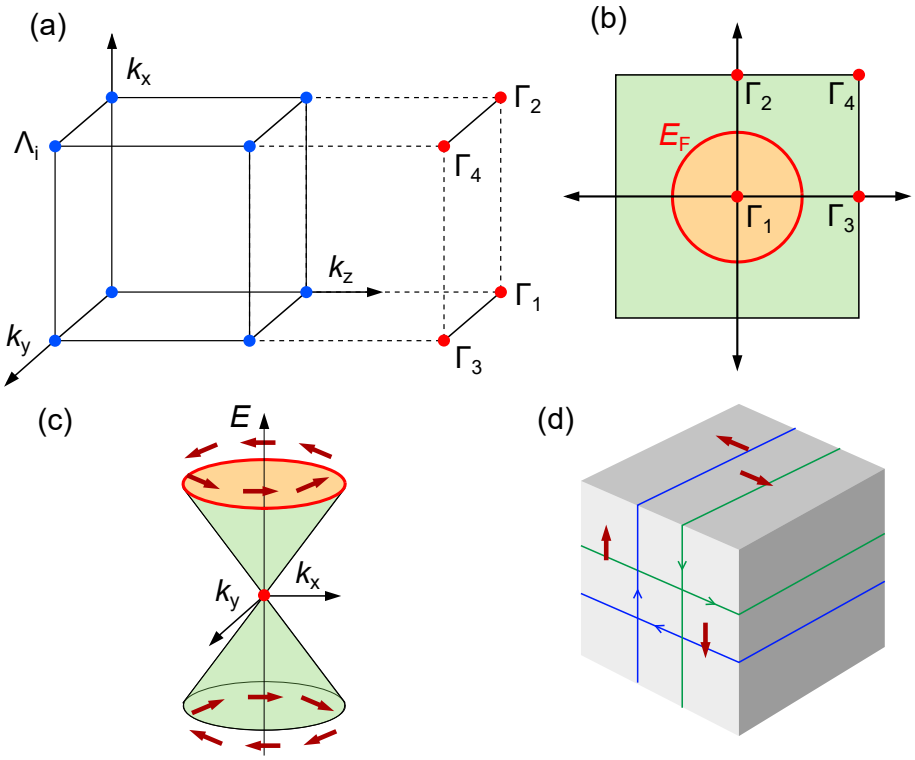

Fig. 2.20: (a) The Brillouin zone of a 3D insulator with eight $\mathcal{T}$-invariant points Λ_i (blue dots). The Brillouin zone of a surface has four $\mathcal{T}$-invariant momenta Γ_i (red dots). These are projections of pairs of Λ_i. Adapted from [5, 47, 92]. (b) Surface Brillouin zone of a 3D TI. The Fermi circle (red circle with orange area enclosed) encloses a single $\mathcal{T}$-invariant point. This characteristic describes a strong TI. Adapted from [46, 47]. (c) A Dirac cone describes the dispersion of a single surface (orange area). Adapted from [47, 94]. (d) Real-space projection of the surface states of a 3D TI. The spin of the electrons is oriented in perpendicular direction to the direction of motion, respectively. Adapted from [47, 94].

2.4.4 Strained HgTe as a three-dimensional topological insulator

Up to this point, we have only considered whether potential surface states are protected by topology. To see how these states actually form in HgTe, we need to examine the system's band structure more closely.

The topologically nontrivial phase in HgTe originates from its inverted bulk band structure, which gives rise to an unusual quantum confinement effect in HgTe/CdHgTe quantum wells. In narrow wells with a thickness below a critical value h_c, the lowest electron-like subband E_1 is positioned above the lowest hole-like subband H_1 [96], resulting in a normal band order typical of a trivial insulator. As the well width h increases, the E_1 and H_1 levels cross [97], producing a band structure that resembles the linear dispersion of massless Dirac fermions [98]. Once the thickness exceeds the critical point h_c, an inversion between the E_1 and H_1 subbands occurs, transitioning the system into the QSHI phase. As described before, this phase hosts a pair of gapless, helical edge states that are topologically protected by time-reversal symmetry $\mathcal{T}$ [93]. In HgTe-based systems, this critical thickness, marking the boundary between trivial and topological insulator behavior, is approximately $h_c = 6.3$ nm [93]. The transition between a 2D TI and a 3D TI system occurs at a thickness of $h \approx 20$ nm of the HgTe layer [99].

In a heterostructure consisting of a trivial semiconductor and a TI, the band structure has to continuously transform from one into the other. However, a continuous transformation of an s-orbital into a p-orbital is forbidden due to symmetry reasons. The s-orbital is symmetric while the p-orbital is antisymmetric under inversion symmetry. HgTe has a zincblende structure and hybridizes between the 6s electrons of the Hg atoms and the 5p electrons of the Te atoms. To demonstrate the peculiar properties of the HgTe bandstructure, we compare it to the bandstructure of CdTe.

In Fig. 2.21 (a) and (b), the energy levels of CdTe and HgTe, respectively, are shown at the Γ-point. In the initial system (with the Hamiltonian H_0), the s-type Γ_6 band lies energetically above the p-type Γ_8 band. However, relativistic corrections to the energy levels have to be taken into account. In the absence of external fields, the following perturbative terms are relevant:

- 1. The Darwin term (H_D) comes from the motion of the relativistic electron itself (so-called 'Zitterbewegung'), and corrects the energy of s-states.
- 2. The mass-velocity correction term (H_mv) appears in the expansion of the relativistic energy following the leading terms mc^2 and $\frac{p^2}{2m}$ [100].
- 3. The SOI term (H_SO) splits the Γ_8 band into a degenerate Γ_8 and Γ_7 band.

H_D and H_mv are much stronger in HgTe than in CdTe. This is due to the fact that Hg as an element has a much larger mass than Cd. Considering these corrections,

the resulting energy dispersions of bulk CdTe and bulk HgTe near the Γ-point are shown in Fig. 2.21 (c) and (d). The p-type Γ_8 band is energetically shifted above the s-type Γ_6 band in HgTe, leading to an inverted band structure in HgTe [101].

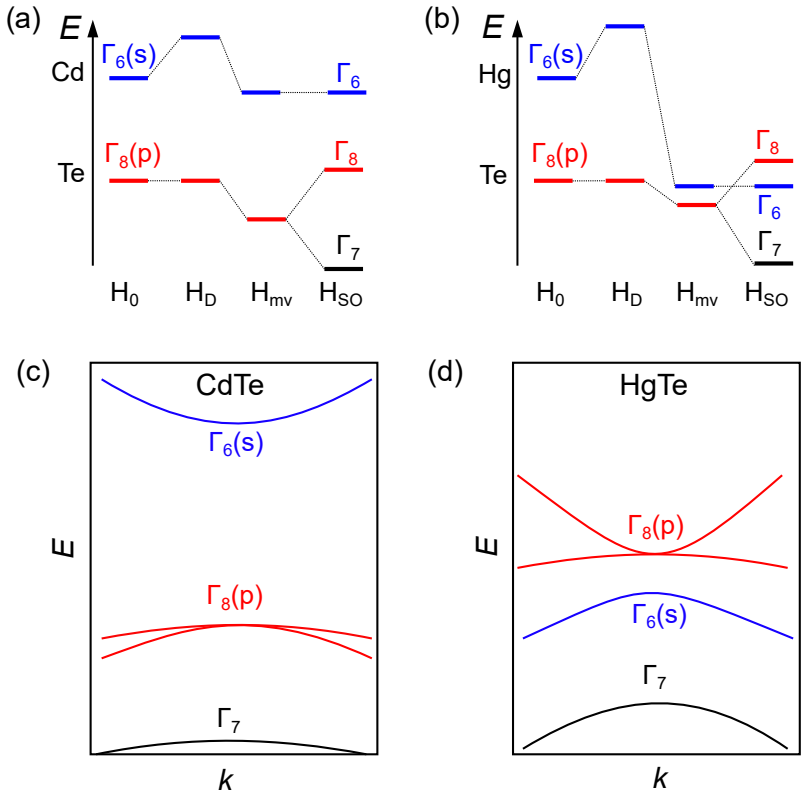

Fig. 2.21: Illustration of the band structure of CdTe (trivial seminconductor, in (a) and (c)) and HgTe (topological semiconductor, in (b) and (d)). (a) and (b): Energy corrections for elemental Cd and Te (in (a)) and Hg and Te (in (b)), contributed to the unperturbed Hamiltonian H_0 from the Darwin term (H_D), mass-velocity term (H_mv) and spin-orbit term (H_SO). All these contributions lead an inversion of the s-type Γ_6 band (blue) and the p-type Γ_8 band (red). Adapted from [101]. (c) Band structure of CdTe. CdTe has a conventional band structure where the Γ_6 band lies above the Γ_8 band. (d) Band structure of HgTe. HgTe has an inverted band structure with respect to CdTe, since the Γ_8 band lies above the Γ_6 band. Adapted from [47, 102].

At the interface between HgTe and CdTe, the bands need to reverse their order, because it is not possible to continuously transform an s-type band into a p-type band. Hence, the s-type band of CdTe descends in energy while the p-type band rises when approaching the HgTe layer. The bands cross at the interface, and the band gap vanishes. These states are the topologically protected surface states which connect the Γ_6 and Γ_8 bands of HgTe and CdTe, respectively. They are illustrated

in Fig. 2.22 in red. The described mechanism corresponds to a topological phase transition at the interface. The topological invariant (Chern number) changes from $n = 1$ (HgTe) to $n = 0$ (CdTe). HgTe has no band gap and is a semimetal. However, a gap is favored as otherwise the bulk would dominate the transport properties. In order to open a gap between the Γ_8 bands, HgTe is grown on a CdTe substrate. This leads to a strain in the HgTe layer due to a lattice mismatch of 0.3% between the two materials. This strain opens a small gap in the order of $15 - 20$ meV [54, 103] in the bulk band structure of HgTe.

When describing the band structure of strained HgTe, it is important to note that the Dirac point, i. e., the point where the two conical surfaces of the Dirac cone meet, is buried deeply in the VB, where surface electrons and bulk holes co-exist [102]. This is illustrated in Fig. 2.22 (a). It cannot be accessed directly by transport experiments as the Fermi level cannot be tuned to this region [54, 104–106]. However, it is possible to access it indirectly by probing spin-helical surface states in HgTe nanowire structures [67].

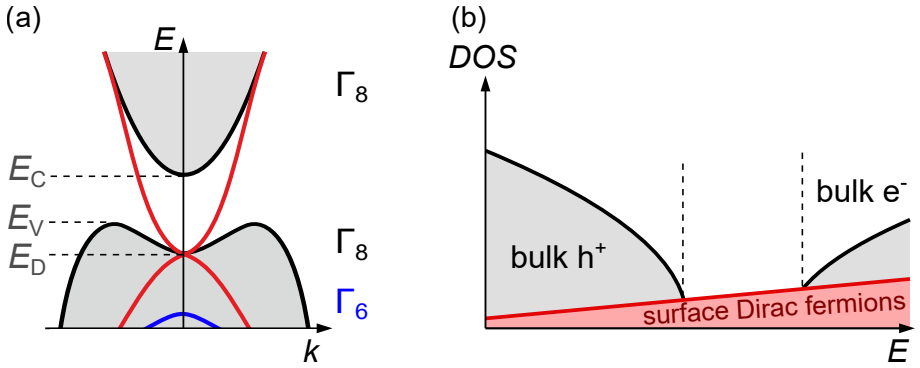

Fig. 2.22: (a) Simplified band structure of the 3D topological insulator HgTe, showing surface states (red) within the band gap. The Γ_8 (black) and Γ_6 (blue) bands, the edges of the conduction E_C and valence bands E_V, as well as the theoretical Dirac point E_D, are indicated. Adapted from [43]. (b) Schematic DOS of strained 3D TI HgTe. In the bulk gap (indicated by dashed lines), conducting surface helical states with close to linear dispersion are present (red). The bulk electrons e^- and holes h^+ (both in gray) have a parabolic dispersion. Adapted from [54].

3. Experimental methods

On the following pages, the fabrication and measurement techniques of the devices will be described. First, we explain the design of the wafers used, followed by the fabrication steps, most of which were performed under cleanroom conditions. A detailed step-by-step manual of the fabrication process can be found in Appendix A. In the end of this chapter, the measurement setups, i.e., the cryostat and electronic setup, are described. Possible causes of measurement errors are discussed.

3.1 Device fabrication

In the following, the fabrication under cleanroom conditions is described. The devices undergo a number of processes, the most complex and error-prone of which is electron-beam lithographic writing and wet-chemical etching of the nanostructures. During the entire fabrication procedure, it is essential to ensure that a temperature of 120 °C is not exceeded. At higher temperatures, the danger of diffusion effects of mercury atoms has to be taken into account, which would damage the devices under study [107, 108].

3.1.1 Used material

The investigated devices were fabricated on chips from strained 30 to 80 nm thick HgTe thin films grown by molecular beam epitaxy (MBE) on (013)-oriented GaAs substrates at the A. V. Rzhanov Institute of Semiconductor Physics in Novosibirsk (for details see Ref. [106]). GaAs substrates with (013)-oriented surface orientations are used with a 4 µm thick CdTe buffer layer [109]. This provides a defect-free substrate for the $Cd_xHg_{1-x}Te$/HgTe heterostructures. The material is intrinsically p-doped. A list of which wafer was used for each device and the exact composition of the wafers is included in Appendix B.1. The most common wafers, used for the devices presented in the experimental results, are schematized in Fig. 3.1.

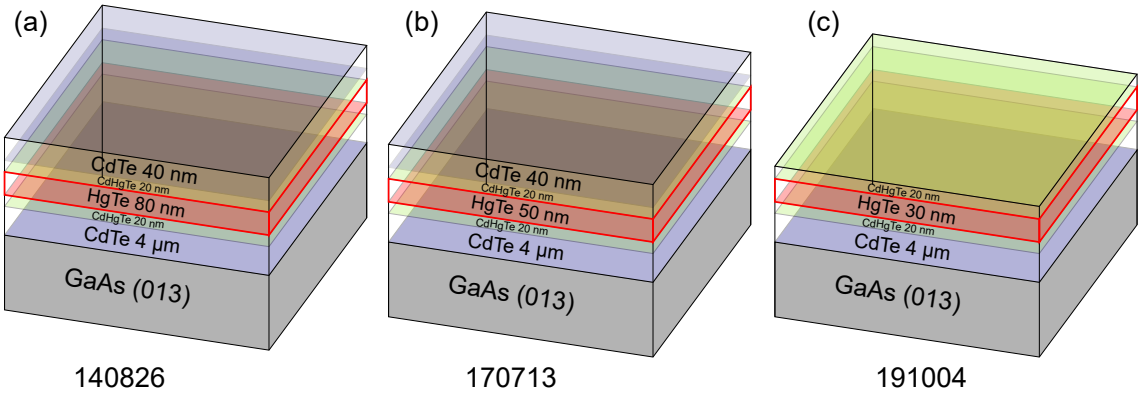

Fig. 3.1: Wafer design of the three most used wafers in this work, with the HgTe layer in red with different thicknesses: (a) $h = 80$ nm, (b) $h = 50$ nm, (c) $h = 30$ nm. The heterostructure is grown on a GaAs substrate (gray) and a CdTe buffer layer ($h = 4$ µm). Then, the HgTe layer is embedded in two $Cd_{0.45}Hg_{0.55}Te$ layers (for all three wafers). Finally, the wafers are capped by CdTe in the case of (a) and (b). (c) remains capped only by HgCdTe in order to obtain a HgTe layer very close to the surface. The numbers of the wafers are indicated below the respective illustration.

3.1.2 Fabrication of the macroscopic Hall bar

First, an etch-resistant resist for optical lithography is applied to the sample surface. It is rotated with high speed in a spin coater to achieve a well-defined homogeneous resist layer. It is then baked out in order to evaporate the solvent which is contained in the resist. Afterwards, a macroscopic Hall bar is defined by an optical mask, and the area outside of it is exposed to light. The chemical structure of the resist in the exposed parts is modified, making it soluble by a developer. After applying the latter and removing the exposed resist, the HgTe layer is selectively etched in a solution consisting of bromine (Br_2), ethylene glycol ($C_2H_6O_2$), and distilled water (H_2O) at a ratio of $0.1 : 100 : 25$. A constant temperature of $T = 0°$ C is necessary to maintain a controllable and reproducible etching rate [110]. After reaching the desired etch depth (for mesas normally reached within the range of several minutes), the etching procedure is stopped by putting the sample in distilled water. The residual resist is then removed, leaving behind a mesa in Hall bar shape along with its electrical contacts, as illustrated in Fig. 3.2 (a). The patterning was performed using a Carl Süss MBJ3 optical lithography system. This method is limited in resolution by the wavelength of the UV light used. The finite resolution is due to diffraction effects and the precision constraints of optical masks, making optical lithography suitable only for creating features larger than about 1 µm with the device used. Structures that fall below this order of magnitude, in our case the etch trenches defining the QPC (shown in Fig. 3.2 (b)), are defined using electron beam lithopgraphy, which is discussed below. An important distinction in the terminology between the term 'sample' and 'device' is explained in Fig. 3.2. The term 'sample' refers to the entire

macroscopic structure, while the term 'device' refers to the mesoscopic structure.

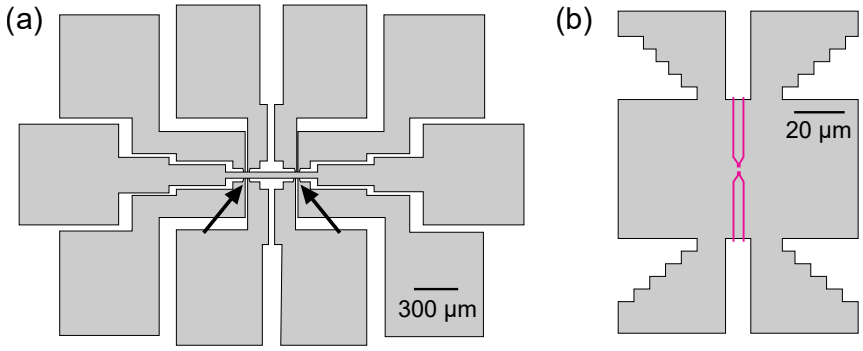

Fig. 3.2: (a) Hall bar shape (mesa) with contacts, defined by means of optical lithography. We will refer in this thesis to this entire structure as a 'sample'. The arrows mark the QPC region. We define the QPC as the 'device'. One sample can host two devices, which share the same Hall bar. This is the case in particular for the reference devices A1 and B1, which are placed on sample e23 and share the same Hall bar. (b) Detail marked by arrows in (a): QPC structure with supply lines in pink, defining the constriction as etching trenches. The pink lines are defined by electron beam lithography.

3.1.3 Lithography and structuring of nanoscale devices and etching

The de-Broglie wavelength of electrons is much shorter than the wavelength of light. Electron beam lithography (EBL) provides the necessary resolution of up to 10 nm precision for mesoscopic devices. The EBL resolution is limited only by effects such as scattering of electrons in the resist, making it a high-precision method for the definition of mesoscopic structures. Another advantage of EBL is the definition of digital instead of physical masks, transferred to the sample by means of a computer-controlled electron beam. A step-by-step scheme, illustrated in Fig. 3.3, is described in the following.

After preparing the macroscopic Hall bar structure (see Fig. 3.3 (a)), described in the previous section, the fabrication of the mesoscopic devices can proceed. An etch-resistant PMMA[1]-based resist is applied to the sample surface (see Fig. 3.3 (b)). After placing the sample in the SEM (scanning electron microscope), it is irradiated by the custom-tailored electron beam (see Fig. 3.3 (c)). For this method, a Carl Zeiss Auriga SEM system was used. The developed mask of the QPC structure is then again wet-chemically etched in a Br_2-based solution. This step is processed in an analogous way as when etching the mesa, with the difference that the etching time is

[1]poly(methyl methacrylate), also known as acrylic

much shorter, in the range of tens of seconds. After finishing etching, the protective resist is dissolved by a remover (see Fig. 3.3 (d)). Although the trench has a width of only 30 nm in the original EBL file, the final width after etching is much wider ($400 - 500$ nm). This is due to the fact that nearby parts of the irradiated areas are also developed during EBL [47], and an isotropic etching process [49], which leads to an etching width up to as twice as large compared to the etching depth. This width is caused in particular by the fact that the under-etching of the material below the resist takes place. The isotropic etching process also causes the etched structure to be rounded and smoother. Therefore, we do not obtain a rectangular shape of the QPC cross section, but instead a trapezoidal shape. An example of an etched QPC before oxide and topgate deposition is shown in Fig. 3.4 in an SEM in (a) and an AFM (atomic force microscopy) image in (b).

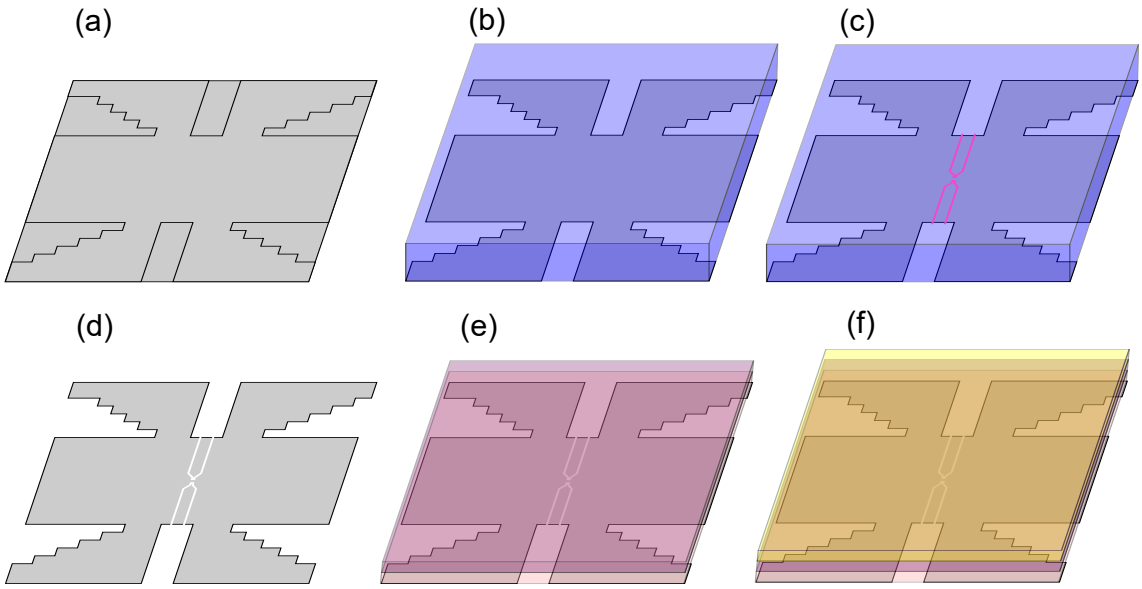

Fig. 3.3: Steps of the fabrication process. The Hall bar area around the QPC is shown. (a) Definition and etching of the Hall bar, proceeded by optical lithography. (b) Application of EBL resist. (c) EBL lithography of QPC device. The steps serve as alignment markers. (d) Wet-chemical etching with a Br solution, and removal of excess resist. (e) Deposition of oxide layers SiO_2 and Al_2O_3. (f) Deposition of a global metallic topgate.

Rough areas can be distinguished in the etched trenches especially in the AFM image. While a smooth etching profile was still relatively easy to achieve for larger nanowires by wet-chemical etching [49], it proved to be a challenge for the very fine QPC structures. In particular, the quality of the PMMA-based coating resist turned out to be a major source of obstacles during the course of the work. Once a sample has been coated with PMMA, it should be continued to be processed with this

particular coating instead of being coated several times because of inhomogeneities, as PMMA is not completely soluble in acetone and isopropanol. The last two steps of the cleanroom fabrication, illustrated in Fig. 3.3, will be introduced in the following.

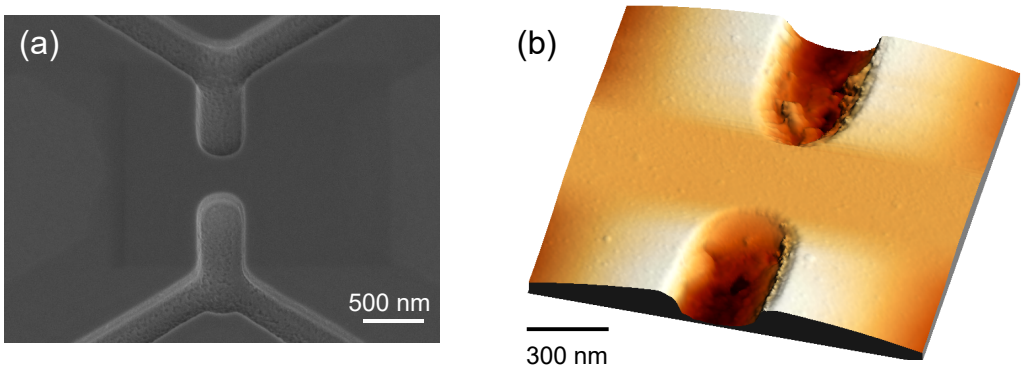

Fig. 3.4: (a) SEM image of a representative HgTe TI QPC, taken at a tilt angle of 50° before deposition of the oxide layers. Wet-chemically etched trenches with a depth of approx. 300 (±50) nm. (b) 3D AFM profile of a QPC with clearly visible rough etching profile with a roughness of ±50 nm.

3.1.4 Oxide layer and topgate fabrication

After etching, the wires are covered with 30 nm of SiO_2 using plasma enhanced chemical vapor deposition (PECVD), followed by 100 nm of Al_2O_3 applied by atomic layer deposition (ALD). As an alternative to Al_2O_3, HfO_2 can be applied. A suitable recipe for this purpose was developed in Ref. [111]. The SiO_2 layer is used in order to improve the adhesion of the Al_2O_3. For the subsequent deposition of a topgate, which is necessary for the modulation of the chemical potential, a metallic layer consisting of titanium or chromium (typically 5 nm), and gold (typically 80 nm) is used. Again, the thin titanium (or chromium) layer is necessary for an improved adhesion of the gold layer, to ensure a robust gating. For the devices under study, a global topgate covering the entire macroscopic Hall bar was applied. With this geometry, an additional p-n transition between gated and ungated regions can be excluded. A schematic cross section of the finished etched and gated QPC is depicted in Fig. 3.5. The trapezoidal shape, as mentioned previously, resulting from the isotropic etching process, is displayed.

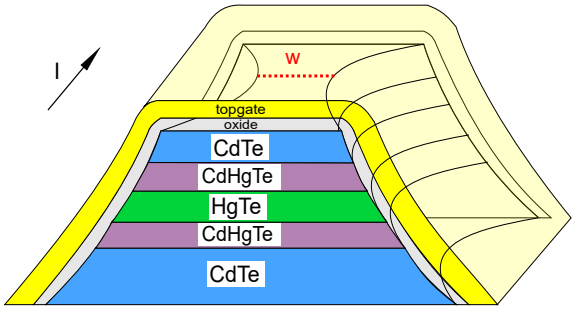

Fig. 3.5: Cross-section of a finished QPC. The point contact is defined via wet-chemical etching and covered by an oxide layer consisting of SiO_2 and Al_2O_3 (gray) and a metallic topgate (yellow). The width w is defined as indicated. However, the physically relevant width is given by the width of the HgTe layer (without the naturally oxidized edge areas), not by the slightly narrower width of the upper end of the CdTe layer. However, we can assume that these match each other to within a few nm. The current direction applied in experiment is indicated.

3.1.5 Contacting the HgTe layer

Next, Ohmic contacts, connecting the devices to the chip carrier, are formed by soldering indium manually on the contact pads (see Fig. 3.2 (a)), connecting the latter to the chip carrier with gold (or aluminum) wires. Indium as a soldering material has the advantage that it hardly deforms when it is cooled down. Alternatively, evaporating metallic pads is possible, but more intricate. The quality of contacts was studied in detail in [107].

3.1.6 Annealing

Since the quality of measurements on HgTe structures was generally often accompanied by noise and occasionally non-ideal macroscopic quantization, the fabrication process was optimized in a separate project. An additional facultative annealing step was elaborated in the Master's thesis by Juliane Steidl [107]. In the present work, it was typically not used. However, for future work it can be recommended to improve measurement quality. From multiple points of view, the most favorable measurement quality is obtained after annealing at 120°C for macroscopic measurements, which manifests in a reduction of noise and improved quality of QH plateaus and SdH oscillations. Mesoscopic structures are more sensitive to annealing due to their increased ratio of side surfaces to bulk material [107]. In general, annealing improves the quality of measurement, even though the contact quality is reduced, in the sense of measuring higher contact resistances. We attributed the improved measurement quality to a reduction of bulk inhomogeneities and side surface defects, which together dominate over a degradation of contact quality.

3.2 Measurement setups

3.2.1 Dilution refrigerator cryostat

In order to realize a ballistic transport environment in a QPC, temperatures have to be as low as possible, in the ideal case in the range of only a few mK [49]. Therefore, the majority of measurements were conducted in a dilution refrigerator at temperatures of usually 80 mK, or in conventional ^{4}He bath cryostats at approximately 1.5 K for additional measurements. The conventional cryostat system will not be discussed in detail here.

The cooling process of a dilution refrigerator relies on the phase separation of ^{3}He$-^4$He mixtures. Due to stronger zero-point motion, the binding forces between ^{3}He atoms are weaker than those between a ^{3}He atom and a ^{4}He atom. As a result, the two isotopes do not form completely distinct phases, even at absolute zero temperature (0 K). However, when the concentration of ^{3}He in ^{4}He reaches 6.4 %, the binding energies become sufficiently low so that ^{3}He is no longer soluble in ^{4}He. This results in the formation of two separate phases: a concentrated phase composed entirely of ^{3}He, and a dilute phase containing 6.4 % ^{3}He and 93.6 % ^{4}He. By continuously extracting ^{3}He from the dilute phase, additional ^{3}He from the concentrated phase enters the dilute phase to maintain equilibrium. This phase transition requires energy, which is drawn from the surroundings, thereby producing a cooling effect [55].

The wet Oxford Instruments Kelvinox TLM dilution refrigerator is schematically shown and explained in Fig. 3.6. The dilution unit chamber is surrounded by multiple layers of insulation: an inner vacuum chamber, followed by a ^{4}He reservoir, a nitrogen shield, and an outer vacuum chamber. The mixing chamber, where the ^{3}He$-^4$He mixture is placed, connects to a distiller ('still'), which distils the ^{3}He from the ^{4}He due to the difference in vapor pressure. The components are illustrated in Fig. 3.6 (a). The ^{3}He$-^4$He gas mixture flows through the system, and by continuously pumping on the dilute phase via the still, ^{3}He is extracted until it evaporates. To maintain the most energetically favorable state, ^{3}He from the concentrated phase moves into the dilute phase, creating a cooling effect. A more detailed view into the inner circuit of the dilution refrigerator is drawn in Fig. 3.6 (b). With the Kelvinox system, temperatures as low as 15 mK can be reached, depending on the sample holder, while the maximum stable temperature is around 1 K. In order to generate magnetic fields up to 19 T, the Kelvinox TLM includes a superconducting coil within the ^{4}He bath. In this work, the maximum applied magnetic field was 17 T, however mostly magnetic fields of up to 8 T were applied. A feature of this system is that samples can be directly inserted into the mixing chamber using a specialized rotating sample holder, enabling measurements in in- and out-of-plane alignment of the magnetic field within the same measurement cycle. Electric lines are routed to the sample via the sample holder. The rotating sample holder includes a switch panel located

directly above the sample. This allows filter devices to be connected between the room-temperature devices and the sample in the ^{3}He – ^{4}He bath. The used filter device is described in the following section.

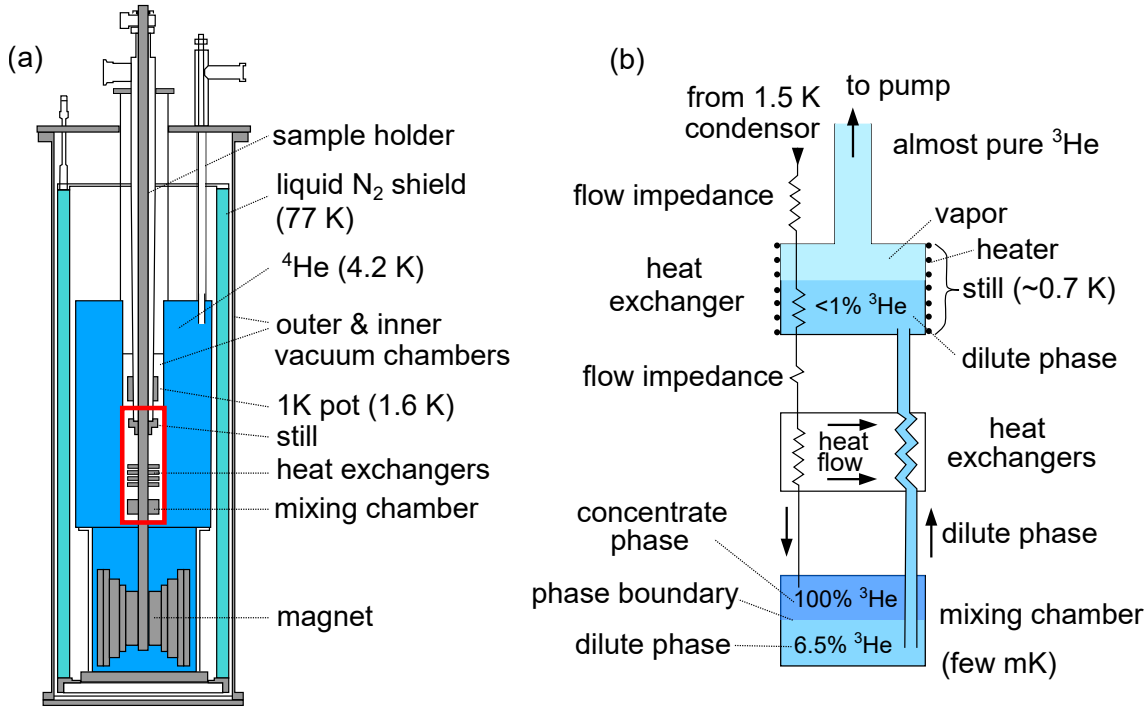

Fig. 3.6: (a) Sketch of a wet top-loading dilution refrigerator. Wet dilution refrigerator systems use evaporative cooling from liquid helium as a pre-cooling stage at 4.2 K. By pumping liquid helium through the 1 K-pot, a second pre-cooling stage at 1.5 K is achieved. The ^{3}He – ^{4}He mixture flows into the dilution unit, passes by the ^{4}He bath and 1 K-pot, where it cools to below 2 K and liquefies. The mK cooling process occurs in the inner circuit area, highlighted in red in (a) and described in (b). The mixing chamber and the surrounding regions above of it are enclosed by an inner vacuum chamber, a ^{4}He reservoir, a nitrogen shield, and an outer vacuum chamber. The sample holder is directly inserted into the mixing chamber. (b) Principle of operation for the inner circuit of a ^{3}He-^{4}He dilution unit (detail from (a) in red). ^{3}He is continuously drawn out of the dilute phase via the still (distiller). Thus, ^{3}He from the concentrate phase enters the dilute phase to maintain the most favorable concentration, which leads to a cooling effect. Adapted from [49, 112].

3.2.2 Electronic measurement setup

Measurements were carried out with standard AC lock-in techniques at a frequency of $f = 13$ Hz or lower in four-point configuration with Signal Recovery DSP 7265 lock-in amplifiers. These devices were also used as an AC current source. A pre-resistance of several orders of magnitude higher than the resistance of the sample is added ($R_{\mathrm{pre}} = 10$ or 100 MΩ), leading to a constant current given by $I = V_{AC}/R_{\mathrm{pre}}$ through the sample. The applied current amplitude was within the range of $I = 1$ and 10 nA. The value of the current was chosen in a way to avoid excessive heating. A Yokogawa 7651 voltage source supplies a topgate voltage. Voltage pre-amplifiers (Femto DLPVA-100-F-D) are used in order to amplify the voltage signals measured across the devices and to obtain a high input impedance. The measurement setup used at the dilution refrigerator is sketched in Fig. 3.7.

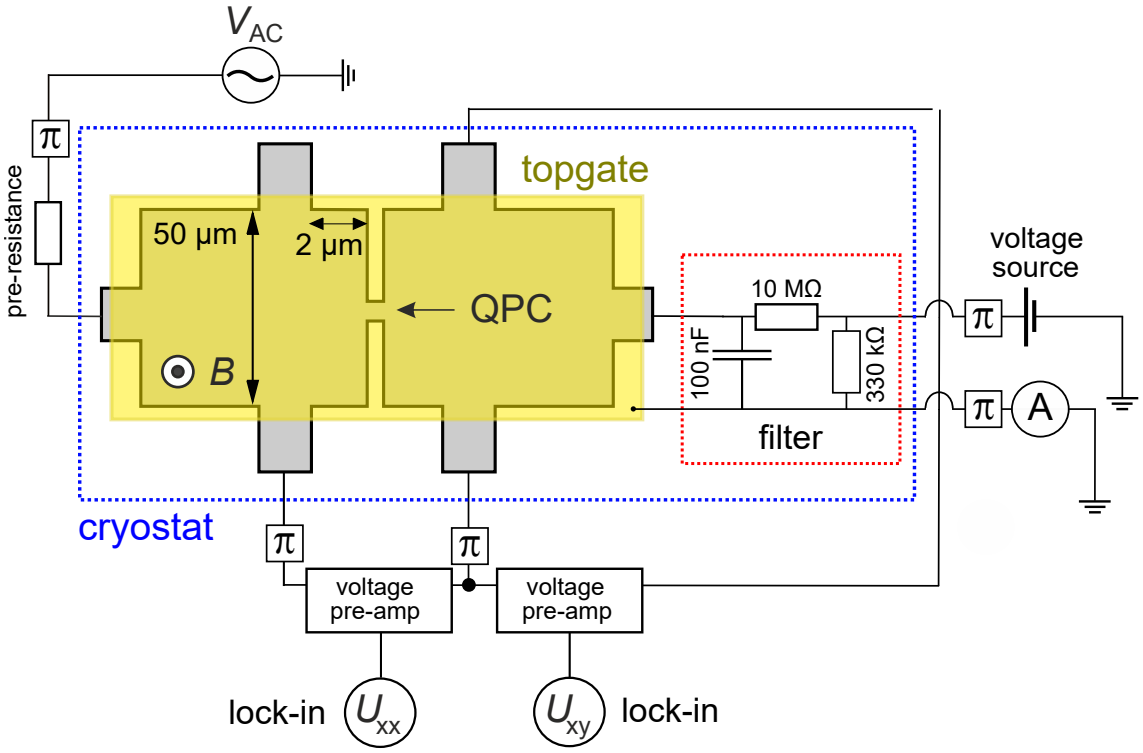

Fig. 3.7: Measurement setup for nanostructures in four-point geometry, where both the longitudinal signal through the QPC (U_{xx}) and the Hall signal (U_{xy}) are measured. The standard AC lock-in setup is extended by voltage pre-amplifiers (to amplify the weak measured signals) and π-filters (to filter high frequency noise and thereby prevent the measured structures from an increase of the electronic temperature). The signal is susceptible to fluctuations of the topgate potential, which makes a low-pass filter necessary (see 'filter' within dotted red line), placed directly in the cold environment inside the sample rod, as in previous work filtering outside the cryostat has not proven to be sufficient [49].

A four-point geometry itself is not sufficient to measure without undesirable effects, addressed in the following. Two types of low pass filters were added in this context. First, in order to eliminate fluctuations of the topgate potential by noise in the measured signal, which used to be insufficient outside the cryostat, we use a low-pass filter. It is placed in the cold He mixture environment inside the sample rod, as illustrated in Fig. 3.7 by the red-dotted box. This filter device was already introduced in previous work [49], where it is described in more detail. The main idea of the filter is to combine a current divider and a low-pass filter. The current divider consists of two resistors, which reduce the amplitude of the high-frequency noise signal by the ratio of the two resistors. Then, the low-pass filter uses a resistor and a capacitor to attenuate unwanted signal components above the cut-off frequency by not immediately charging the gate when applying a voltage, but increasing the charge gradually via the capacitor. The gate is then also protected from large voltage drops, which preserves the sensitive topgate against electrical breakdown.

Second, so-called π filters were used at each contact connected. They will be discussed in more detail later in this section. The main purpose of a π filter is to reduce high-frequency noise and residual noise in a power supply in order to provide sensitive electronic components with a clean and stable signal. π filters are electronic filter circuits consisting of a series connection of a capacitor, an inductor, and another capacitor, arranged in the form of the Greek letter π. They act as low-pass filters, where the range of filtered frequencies has to be chosen accordingly.

3.2.3 Sources of coupling effects

In the following, by identifying possible disturbance signals, we will exclude the possibility that our measurements, especially those of the conductance, could be influenced due to artifacts from a non-ideal measurement setup with insufficiently optimized measurement parameters.

If the measured resistance becomes too high, i.e., due to contact resistances R_c (values of contact resistances in our system range in the order of several kΩ) in addition to the sample resistance R_{sample}, the AC current will look for other paths to flow through. This can lead to the formation of capacitive couplings at a number of parts of the measurement setup. In the following, possible sources of coupling in our setup are considered. These capacitances make the effective circuit more complex by additional contributions to the impedance, which leads to distortions of the measurement signal. The setup highlighting coupling sources is schematized in Fig. 3.8. With $C = 5.5$ nF, π filters increase the overall capacitance in the system the most compared to the other parts presented, which is one order of magnitude higher than the rest of the unintended capacitance sources. These include especially voltage pre-amplifiers, but also cables, which contribute with an estimated $C = 500$ pF to the capacitance in the system [17].

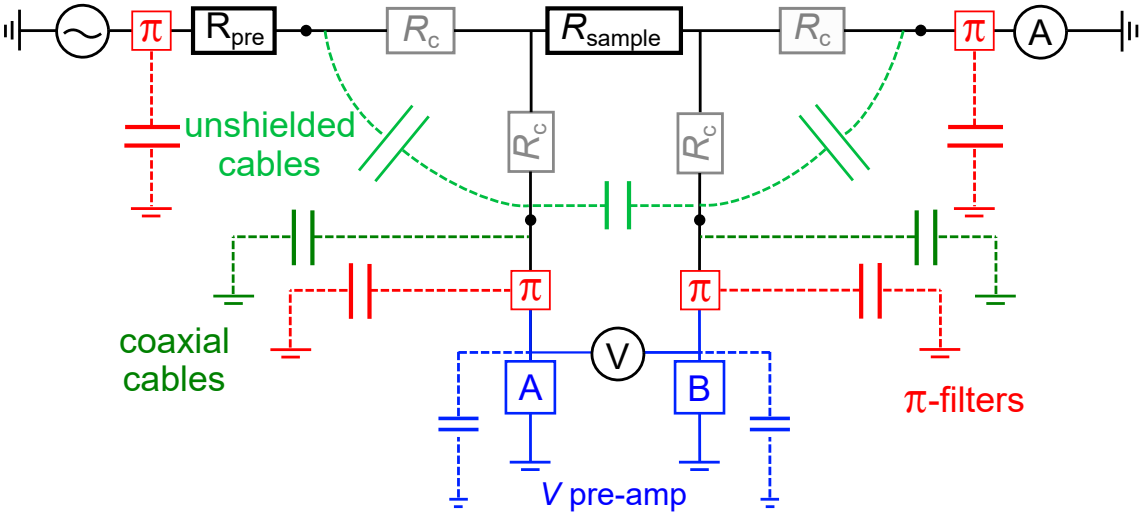

Fig. 3.8: Schematic measurement setup highlighting possible sources of capacitive coupling, which may distort the measured signal [60]. In the ideal scenario, $I_{\text{sample}} = V_{\text{out}}/R_{\text{pre}} = I_{\text{probe}}$ applies. The ideal current flow then only occurs through the sample (with sample resistance R_{sample}. The corresponding current path is schematized in the upper line from left to right (black, intended current flow). Deviations from the ideal case are caused by the presence of various capacitances marked in gray, red, green and blue. In detail, these are (listed by colors): Red: π filters (each one yielding $C = 5.5$ nF, making these the main capacitive coupling source). Blue: voltage pre-amplifier with inputs A and B (with internal capacitance $C = 25$ pF). Green: cables among each other (estimated with $C = 500$ pF for the entire system). Here, we distinguish between coaxial cables outside the sample rod (dark green), and unshielded cables inside the sample rod (light green). The black points illustrate the connections between unshielded and (shielded) coaxial cables. Gray: R_c denotes the resistance of the contacts, which also influences the measured conductance signal. We do not specify R_c in this work. Therefore, in this case, their C contribution is difficult to estimate. In order to avoid its influence on the measured signal, we choose a high input resistance of the voltage pre-amplifier and low measurement frequencies.

3.2.4 Impact of capacitive coupling effects on measurement quality and possible solutions

We have introduced an overview of sources of unintended capacitive coupling. In reality, the resistance of the sample varies with V_g and B. This leads to non-constant amplifications in the measured signal, manifested by distortions in the signal. In Fig. 3.9, a scheme of how these distortions may look is illustrated. Conductance steps in different regions of the band structure are displayed, comparable to those in the experiment shown in Fig. 2.9. This example is relevant at this point because of the results that will be presented later in the experimental part, where non-quantized conductance plateaus will play a major role. By eliminating as many components of the setup as possible that are not absolutely necessary (i.e., the simplest example, using short cables) and optimizing essential measurement parameters, we can approach the ideal case.

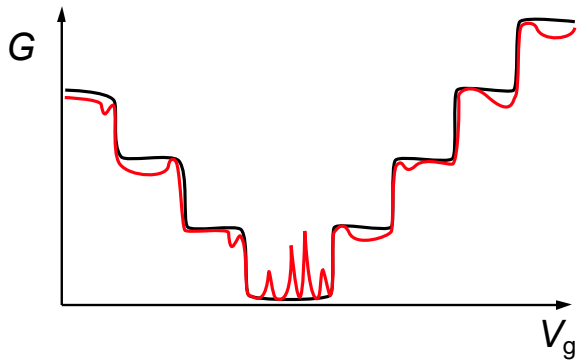

Fig. 3.9: Effect of capacitive coupling on measurement quality. The ideal measurement result without distortions is shown in black. The measured conductance curve (red) is distorted by coupling effects. The distortion comes from the fact that R_{sample} depends on V_g and B. As a result, the ratio of R to Z changes (shown in Fig. 3.10). As a result, the capacitive coupling distorts the measured curve in a different way for different B and, here, V_g. Especially areas of high resistance (band gap region) may experience significant distortion. In connection with this, the current measured within this region is very small as a consequence of the high resistance of the QPC device, which reinforces the effect. In the gap region, the condition of applying a constant current defined by the pre-resistance and an AC voltage is no longer fulfilled, as the current flow is impeded through the highly resistive QPC. As a result, the measured current is significantly lower than intended.

In the following, we will try to improve the measurement quality by minimizing parasitic coupling effects. Therefore, we will discuss the choice of crucial measurement parameters such as the frequency. The impedance Z of an ideal capacitor with capacitance C and resistance R in a parallel circuit is given by

$$\frac{1}{Z} = \frac{1}{R} + i2\pi fC \tag{3.1}$$

where i is the imaginary unit and f is the frequency of the applied voltage. At higher (lock-in) frequencies, the impedance of each capacitor becomes smaller, as $2\pi fC$. This provokes smaller resistance, and hence larger current. Capacitive coupling may then become a relevant factor. At lower frequencies, capacitive coupling does not play a notable role. Applying low frequencies leads to high impedance and, consequently, to smaller currents. This in turn eliminates capacitive couplings. However, measurements will experience higher noise. In Fig. 3.10 (a), we display an example of a measurement illustrating why relatively high frequencies (i.e., less noise) are preferred, but at the same time we have to keep in mind that low frequencies are advantageous because they produce less coupling. Using π filters, it is possible to operate at even lower frequencies, which is due to their high internal capacitance. This is shown in Fig. 3.10 (b). By inserting the input resistance of the voltage pre-amplifier $R = 1$ TΩ and $C = 500$ pF without π filters (we estimate this value as the sum of the capacitance stemming from the cables) or $C = 5500 + 500$ pF with π filters (the sum of the capacitance of the π filters and the cables), respectively, into Eq. (3.1), the impedance of the system is decreased if π filters are used (red curve). This enables a lower range of measurement frequency while maintaining the amount of parasitic coupling on one side and noise on the other side. To conclude, the frequency has to be chosen in a way that generates minimum capacitive coupling effects, which means that it should be as low as possible, but not too low. In our setup, it ranges between $f > 1$ Hz and < 30 Hz, approximately.

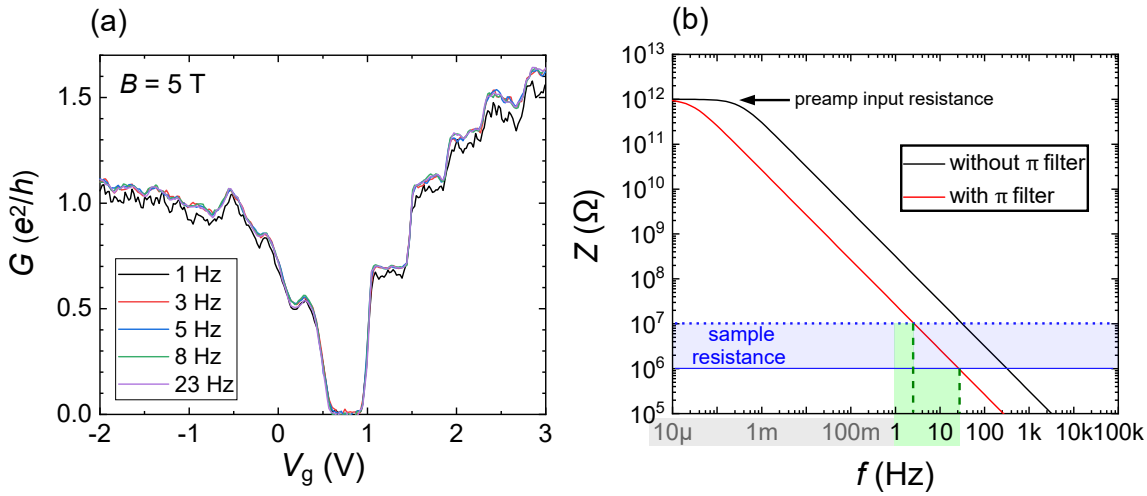

Fig. 3.10: (a) An example of the frequency dependence of the measurements proceeded. Conductance for mesoscopic device A3 is shown for frequencies between $f = 1$ and 23 Hz ($I = 1$ nA). High frequencies are advantageous because of lower noise, but at the same time low frequencies are favorable because of producing less capacitive coupling. While measurements taken at frequencies between 3 and 23 Hz look almost identical, the curve for 1 Hz is decreased in its signal by random noise. The lower f limit is then given by $f > 1$ Hz. (b) Calculated absolute value of the input impedance of voltmeter A (see Fig. 3.8) in comparison to the sample resistance in our system. The black curve is calculated using Eq. (3.1) without including π-filters, while the red curve is calculated including π-filters. First, we observe that by the use of π-filters (with $C = 5.5$ nF), lower lock-in amplifier frequencies can be applied. Further, the graph allows us to determine the ideal frequency range in which we should measure. It was calculated from an estimated $C = 500$ pF for 5 m of cables. The voltage pre-amplifier input impedance is 1 TΩ [113]. The usual sample resistance is estimated with 1 MΩ (full blue line) in the majority of the measured (V_g, B)-range, but it may rise to e.g. 10 MΩ in the gap region (dotted blue line). The corresponding ideal lock-in amplifier frequency range is highlighted in green. In its lower limit (frequency range marked in gray), $1/f$-noise may appear, which should be avoided. In its upper limit, parasitic coupling effects may occur. Comparing the two blue lines, we see that the higher the sample resistance becomes, the more limited the accurate frequency range is (higher limit indicated by dashed green line, for both sample resistances). The frequency range below 1 Hz is shown mainly in order to include the maximum voltage pre-amplifier input resistance. In real measurements, this frequency range is irrelevant.

4. Material characterization

In the first chapter of the experimental part, we will analyze the characteristic transport properties of wafer 191004 with a HgTe thickness of $h = 30$ nm, measured at the macroscopic part of sample e23. The mesoscopic reference devices A1 and B1 (for details, see App. B.2), which will be studied in Chapters 5 and 6, are both placed on sample e23. Our purpose was to fabricate devices with thinner height than the 80 nm used for previous studies [49], but that would still preserve the properties of a 3D TI. With such thin layers, we obtain smaller cross-sectional areas at the QPC. The latter is supposed to be engineered in a way that single-mode transport can be accomplished by narrowing the constriction. This potentially enables us to measure the quantized conductance in 3D TI QPCs. Another advantage of thinner layers was to be able to fabricate with more ease, as it was technically demanding to obtain wires of approx. 100 nm width in a reproducible way. Hence, with a thinner layer, the width could be increased while the cross-section was kept constant.

The following characterization includes the determination of the valence and conduction band edges, as well as charge carrier densities and mobilities in various gate voltage regions, where different types of charge carriers contribute to the transport. The charge carriers also differ by their response to changes in gate voltage: Different charge carrier groups exhibit different partial filling rates, depending on their distance from the gate and their density of states. However, the total filling rate remains nearly constant [106] and is determined by the geometric capacitance of the system. (The slight variation of the total filling rate is due to the variation of the quantum capacitance, affecting the total capacitance by approximately 1 % [106].) Each charge carrier group then forms its own distinct Landau level fan. At the end of the chapter, a two-dimensional map of the conductivity is presented in dependence of the gate voltage and magnetic field, where a complex pattern of Shubnikov–de Haas oscillations is observed as a result of the interplay of different charge carriers.

The entire evaluation presented is based on measurements of the longitudinal resistivity $\rho_{xx} = \frac{U_{xx}}{I}\frac{W}{L}$ (with W being the width of the macroscopic mesa and L its length) and Hall resistivity $\rho_{xy} = U_{xy}/I$, obtained from 4-point measurements at the reference Hall bar of the device, designed as introduced in Chapter 3. For characterization data used for other devices in this work, see Ref. [107] for $h = 80$ nm, and Ref. [49] for $h = 50$ nm. The evaluation of the measurement data follows Ref. [48, 54, 114].

4.1 Determination of the conduction and valence band edge

The basic characterization begins with identifying points on the gate dependence that correspond to specific positions of the Fermi level in the band diagram: the bottom of the conduction band, the top of the valence band, and the charge neutrality point (CNP), where the charge of bulk holes is compensated by the charge of surface electrons. In Fig. 4.1, ρ_{xx} is shown in (a), along with its normalized value with respect to the trace at $B_\perp = 0$ in (b). The latter depicts the band edges with more clarity than in (a). The edges of the bulk bands are located approximately at $V_g^{\mathrm{VB}} = 0.7$ V and $V_g^{\mathrm{CB}} = 2.7$ V. Here, we assign the base of the respective peak to these values, which is particularly easy to recognize in Fig. 4.1 (b). The CNP, which is characterized by a peak in the resistivity, lies at $V_g^{\mathrm{CNP}} = 0.2$ V. In the energy gap (from 0.7 to 2.7 V), we measure a small magnetoresistance, which we trace back to the sole presence of surface states. The magnetoresistance increases in the presence of several groups of charge carriers with significantly different mobility. Since both bulk electrons and bulk holes have a much lower mobility than topological electrons, the magnetoresistance growth indicates the boundaries of bulk zones. The behavior is in accordance with Fig. 2.22 in Chapter 2, with bulk holes and electrons present in the VB and CB, resp., and a few Dirac surface states as the only charge carriers in the band gap. Interestingly, for the material system under study, the conduction band is only weakly pronounced with a small peak in the resistivity, which is better visible in the normalized resistivity in Fig. 4.1 (b), as mentioned previously.

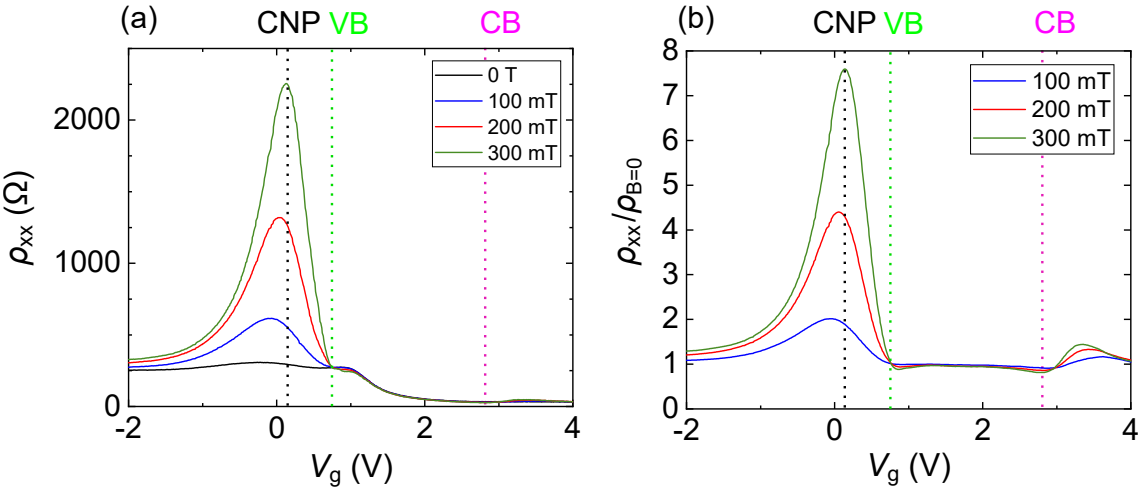

Fig. 4.1: (a) Longitudinal resistivity ρ_{xx} and (b) normalized longitudinal magnetoresistance $\rho_{xx}/\rho_{xx,B=0}$ of the macroscopic part of reference sample e23 in dependence of V_g at low magnetic fields up to $B_\perp = 300$ mT. The CNP (at 0.2 V), the valence band edge (at 0.7 V) and conduction band edge (at 2.7 V) are highlighted. In the present case, the CB edge and the band gap become apparent rather in (b) than in (a).

4.2 Quantum Hall and Shubnikov-de Haas effect

We proceed in the investigation of the charge carrier densities n_s and mobilities μ, which differ for every type of charge carrier in the system and change with respect to gate voltage and magnetic field. This study enables us to obtain insight into the ballisticity of our system via the mean free path length, which we obtain from n_s and μ. For the following study, we recall the theoretical considerations described in Sec. 2.1.2: In a 3D TI, the QHE is formed by the two separate 2DEGs of top and bottom surface, as well as by the bulk, which effectively acts as a third, squeezed 2DEG [114]. This means that the total Hall conductance $\sigma_{xy}^{\text{total}}$ is given by the sum of the Hall conductance of the top surface σ_{xy}^{top}, bulk $\sigma_{xy}^{\text{bulk}}$ and bottom surface $\sigma_{xy}^{\text{bottom}}$. By applying high magnetic fields of several T, the density of states is split into spin non-degenerate Landau levels. This enables us to characterize the sample by the quantum Hall effect at high magnetic fields, in addition to classical transport results at lower fields. Traces for ρ_{xx} and $G_{xy} = 1/\rho_{xy}$ as a function of the gate voltage V_g for different magnetic fields B are shown in Fig. 4.2.

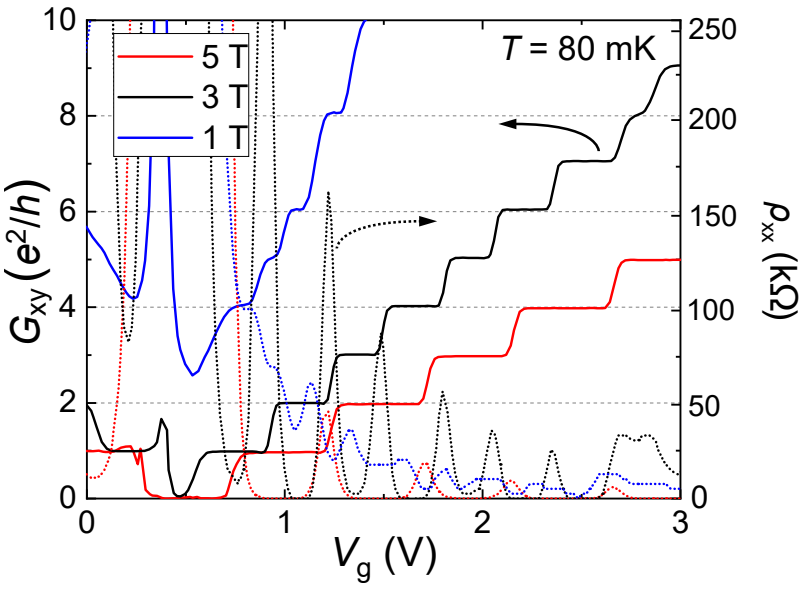

Fig. 4.2: Hall conductance $G_{\text{xy}}(V_{\text{g}})$ in units of e^2/h (full lines) and longitudinal resistivity $\rho_{\text{xx}}(V_{\text{g}})$ (dotted lines) for $B_\perp = 1$, 3 and 5 T. Minima in the longitudinal resistivity appear at the position of the Hall plateaus. Peaks in ρ_{xx} appear at the Hall step transitions. The system shows full quantization.

We observe that for $B_\perp = 1$ T (blue trace), Hall plateaus begin to form at multiples of the conductance quantum $G_{xy} = \nu[e^2/h]$. They occur simultaneously to minima in the corresponding longitudinal resistivity. Correspondingly, a maximum appears at each transition between the Hall steps. However, the traces measured

at $B_\perp = 1$ T demonstrate the G_{xy} plateaus and ρ_{xx} minima missing for some filling factors (e.g., $\nu = 7$ and $\nu = 9$). That is an indicator of the fact that the two Landau levels, originating from different groups of carriers, are too close to each other (or even crossing), collapsing the gap between them. At $B_\perp = 3$ T (black), the Hall steps and resistivity minima reaching zero are fully developed. This indicates that every Landau level becomes well separated from the other ones. At this magnetic field strength, the Hall conductance G_{xy} is clearly quantized in units of e^2/h, with pronounced equidistant Hall steps. For $B_\perp = 5$ T (red), the length of the Hall plateaus and the spacings of the resistivity minima are clearly increased.

In Fig. 4.3, measurements of the Hall resistivity in dependence of $B_\perp$ are shown for the range between $V_g = -1$ V and 3 V. Here, we want to focus on the evolution of the Hall slope with respect to the position of the Fermi energy, i.e., the gate voltage.

Again, sharp Hall plateaus appear at fractions of the von-Klitzing constant ($R_K = h/e^2 = 25\,813\ \Omega$). Curves with positive slopes (for $V_g = 0.6$ V and higher) are assigned to the charge state of the system, where electrons dominate the transport. These slopes are linear, which is a consequence of hosting only one type of charge carrier, i.e., electrons [54]. At $V_g = 0.4$ V, a change of sign takes place, leading to a nonlinear slope for lower gate voltages. The nonlinearity of the slope at this and lower gate voltage points to the coexistence of surface electrons and bulk holes in the valence band. We expect the CNP to be approximately in this region. Fig. 4.2 is more suitable for its determination: the connecting line through the middle of the Hall plateaus and its crossing with $G = 0$ indicates a CNP at $V_g = 0.5$ V. If we continue to decrease the gate voltage and shift deeper into the VB, at 0.2 V already, the local slope remains positive in the vicinity of $B_\perp = 0$, whereas the total slope (with respect to high magnetic fields) switches to negative values. In the part of the VB, where the amount of holes is smaller than the one of the electrons, the Hall resistance will be slightly non-linear in the region of small magnetic fields due to the presence of surface electrons. For lower V_g, where the amount of holes in comparison with the electrons increases, this trend is reinforced, and the nonlinear region around $B_\perp = 0$ becomes less pronounced. Yet, it does not vanish.

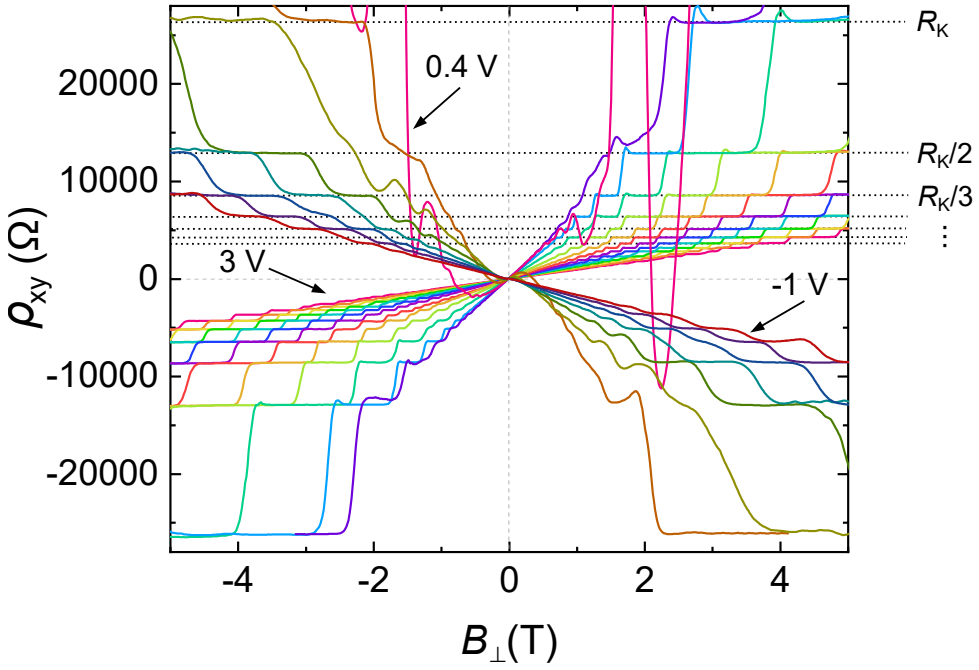

Fig. 4.3: Hall resistance ρ_{xy} as a function of the magnetic field $B_\perp = -5....5$ T at different gate voltages between $V_g = -1$ V and 3 V, in intervals of 0.2 V (each indicated by a different color). At low fields the traces are linear, while at higher fields, Hall plateaus appear at fractions of R_K (highlighted by dotted lines). They start to develop at relatively low magnetic fields, i.e., $B_\perp = 0.75$ T, which points to low disorder in the system. The traces with positive slopes are assigned to gate voltages in the band gap and the conduction band. At $V_g = 0.4$ V (magenta line), a sign change occurs. For this and lower gate voltages, the linear dependence changes to nonlinear (s-shaped around 0), which points to the co-existence of electrons and holes. At this point, the hole density becomes higher than electrons one, as the slope at quantizing fields is determined by a total charge, ie. $n_s - p_s$). Hence, the top of the VB is located at approximately 0.8 V. In both gate voltage directions, the slopes reach a saturation. This is traced back to a saturation of the material 'capacity' to accommodate charge carriers. For this purpose, the interval of 0.2 V of the shown traces is not reduced in this region, in order to emphasize this effect.

4.3 Determination of charge carrier densities and mobilities

In the following, we will determine the different charge carrier densities and mobilities. In a 3D TI, transport is given by bulk electrons in the CB or holes in the VB, respectively, together with the top and bottom surface states. All states at a particular gate voltage form an ensemble of charge carriers. Each of them has its own partial filling rate, which can be summed up to a filling rate, comparable to filling rates of a plate capacitor model [106]. The total filling rate $\alpha_{\text{total}} = dN/dV$ is related to the capacitance as $\alpha_{\text{total}} = C/q$. It is given by the sum of the partial filling rates[1] of each type of charge carrier, which we deduce from the slopes of the V_g-dependent charge carrier densities [114]:

$$\alpha_{\text{total}} = \frac{\partial n_s^{\text{top}}}{\partial V_g} + \frac{\partial n_s^{\text{bulk}}}{\partial V_g} + \frac{\partial n_s^{\text{bottom}}}{\partial V_g}. \tag{4.1}$$

As we know that the QHE is determined by all charge carriers, it gives us only the total density of charge carriers. From the charge transport point of view (though it is not the case if one liked to analyze the electrostatics normal to the sample plane), the bulk charge carriers can be treated as fully two-dimensional charge carriers [114]. In order to extract the partial densities and mobilities, we will use the following experimental techniques. We start with the simpler case of the conduction band and the bulk band gap, where only electrons contribute to transport:

- The Hall carrier density n_{Hall} is calculated in a classical way, from the slope of ρ_{xy} around $B_\perp = 0$ T. This method can only be applied outside the VB because of the linear behavior of the Hall slope in this region. In the conduction band, where surface states coexist with bulk electrons, the Hall slope is determined by a total electron density. In general, several groups of electrons may also give a non-linear Hall slope, but in our system the non-linearity is too weak to allow a quantitative analysis.

- The total charge carrier density n_{QHE} is determined from the SdH oscillations at high magnetic fields. The magnetic field values, for which ρ_{xy} shows Hall plateaus at integer fractions of R_K, are determined. By plotting the filling factor against the inverse magnetic field $1/B$, the charge carrier density n_{QHE} is extracted from the resulting slope. The obtained charge carrier densities correspond to those of n_{Hall}.

In the valence band, the situation is more complex. As seen in Fig. 4.3, the co-existence of Dirac electrons and bulk holes leads to nonlinear Hall resistances, which fortunately allows us to distinguish the contribution of electrons and holes

[1] For more detail on the partial filling rates, see the Supplementary of [67].

[115]. The Drude formalism for two types of charge carriers is applied, in order to extract the charge carrier densities n_s and mobilities μ. In our analysis, we preferred the conductivity σ over resistivity ρ, due to less variation of the final n_s and μ values. The conductivities σ_{xx} and σ_{xy} were obtained by tensor inversion from the measured resistivities ρ_{xx} and ρ_{xy}. In the VB, the longitudinal conductivity σ_{xx} and Hall conductivity σ_{xy} are given by the sum of the conductivities of holes σ_h and electrons σ_e:

$$\sigma_{xx} = \sigma_{xx,\,e} + \sigma_{xx,\,h}, \quad \sigma_{xy} = \sigma_{xy,\,e} + \sigma_{xy,\,h} \tag{4.2}$$

with the resulting two-carrier Drude fit function

$$\sigma_{e(h)} \text{ equal to } \begin{cases} \sigma_{xx,\,e(h)} = \frac{q\ n_{e(h)}\mu_{e(h)}}{1+(\mu_{e(h)}B)^2} & \text{for } B_\perp \geq 0, \\ \sigma_{xy,\,e(h)} = \mu_{e(h)}B\frac{q\ n_{e(h)}\mu_{e(h)}}{1+(\mu_{e(h)}B)^2} & \text{for } B_\perp < 0 \end{cases} \tag{4.3}$$

from which the charge carrier densities and mobilities for the VB are extracted [54]. From a physical point of view, the formulas of Eq. (4.3) apply for both polarities of the B-field, however, here, the combined graph of $\sigma_{xx}(B_\perp)$ for $B_\perp \geq 0$ and $\sigma_{xy}(B_\perp)$ for $B_\perp < 0$ is created in order to fit it with the two-carrier Drude fit. An example of such is shown in Fig. 4.4.

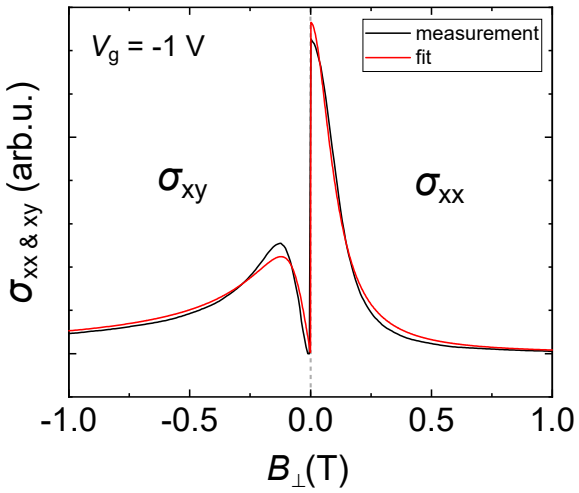

Fig. 4.4: Example of a two-carrier Drude fit (red) of the measured conductivity (black) with the help of the two carrier Drude model for the VB at $V_g = -1$ V. For $B_\perp < 0$, the Hall conductivity σ_{xy} is used, while for $B_\perp \geq 0$, we use the longitudinal conductivity σ_{xx}. The combined graph of σ_{xx} and σ_{xy} is then fitted with the Drude fit function, given in Eq. (4.3), yielding the values of n_e, p_h, μ_e, μ_h in the VB.

Finally, the resulting charge carrier densities and mobilities from VB to CB are shown in Fig. 4.5 (a) and (b), respectively. Considering the graph for the charge carrier densities in (a) from left to right, i.e., increasing the gate voltage, we observe the following: In the valence band, the number of bulk holes continuously decreases until almost vanishing completely at around 0.8 V. This estimate is based on the observation that the behavior obtained of p_h in the range of $0 - 0.4$ V is obviously distorted and these fit values may be omitted, because the two-carrier Drude fit is not a reliable evaluation method, as a comparable amount of electrons and holes with changing ratio is present within this region. Meanwhile, at lower gate voltages, the density of electrons is almost constant in the valence band. The CNP is located at the intersection of these two Drude-determined curves (red and blue), at approx. 0.5 V. This is in accordance with the QHE data presented in Fig. 4.2. Entering the band gap, the Drude electron curve transitions into the Hall-described charge carrier density (black). It is identical to the charge carrier density determined from the quantum Hall effect (green).

The mobilities show an analogous behavior, marking the entrances into the band gap: The electron mobility μ_e has two maxima, at 0.8 V and 2.7 V (black and red graph), which indicate the lower and upper limits of the bulk gap. When entering the VB at $V_g = 0.8$ V, μ_e drops with V_g, with values as low as $130 \cdot 10^3$ cm^2 at -1.5 V, deep within the VB. Hole mobilities are much lower in comparison to μ_e, and increase up to $100 \cdot 10^3$ cm^2 as we move deeper into the VB. In the CB, μ_e represents the average electron mobility of surface and bulk electrons. At the band gap, it rises because there are no low-mobility bulk carriers in the gap, which otherwise reduce the average electron mobility. Electron mobilities μ_e reach values of $400 - 800 \cdot 10^3$ cm^2 in the band gap. At the CB edge, μ_e decreases again due to the lower partial filling rate of the particular electron species among each other.

From these values, we are now able to estimate the mean free path length of the different types of charge carriers $l_e = \mu\hbar k_F/e$, where $k_F = \sqrt{c\pi n_s}$, with $c = 2$ for bulk carriers or $c = 4$ for surface carriers[2]. The result is depicted in Fig. 4.6. The mean free path length of electrons l_e reaches between 2 and 3 µm in the bulk gap. At high V_g (in our system at around $V_g > 3$ V), the average l_e decreases, because the fraction of low-mobility bulk electrons increases.

[2]The relation between g_s and c is determined by the length of the Fermi vector in the k-space. For $g_s = 1$, $n_s = k^2/(4\pi)$, which means that $c = 4$. For $g_s = 2$, $n_s = k^2/(2\pi)$, leading to $c = 2$ [45].

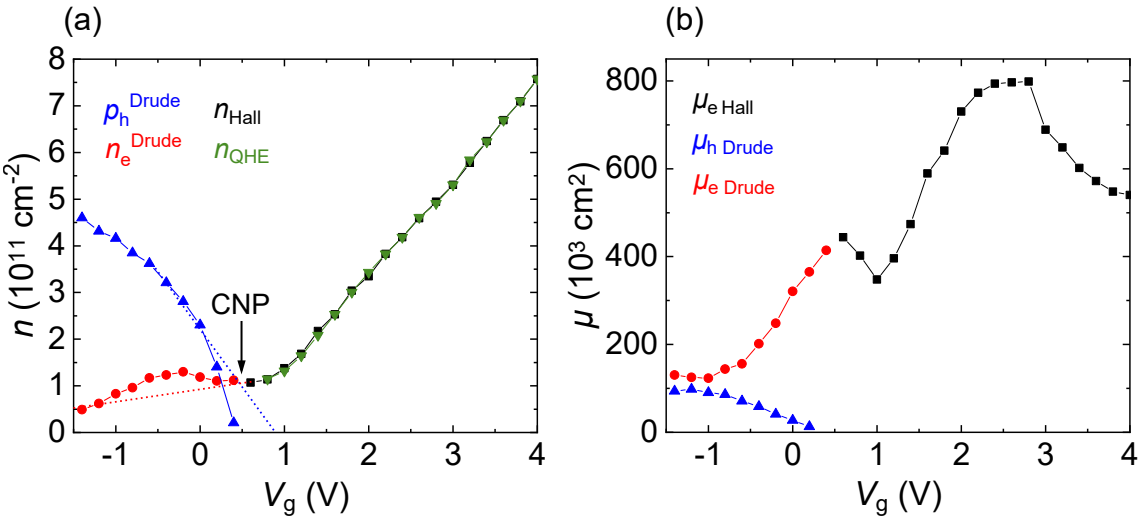

Fig. 4.5: (a) Charge carrier densities of the reference devices A1 and B1 from sample e23. In the VB, surface electrons and bulk holes co-exist. The two-carrier Drude model is used to obtain n_e^{Drude} and p_h^{Drude}. The CNP is located at the intersection of the curves for holes and electrons in the VB. The idealized curves for n_e^{Drude} and p_h^{Drude} are obtained by visually extrapolating the line by eye for the region below 0 V, i.e., in the deeper VB. They are indicated with dotted lines, as the measured values are distorted. In fact, the curves should be linear. The position of the CNP is confirmed here by the extraction of the same from the conductance measured in the QHE. n_{Hall}, n_{QHE} describes the charge carrier densities of surface electrons in the band gap, and surface and bulk electrons in the CB, respectively. The total amount of electrons is derived by evaluating the Hall slope n_{Hall}, the position of Hall plateaus and the SdH oscillations (n_{QHE}). (b) Corresponding mobilities of electrons μ_e and holes μ_p. The mobilities of bulk holes are in general lower than the mobilities of electrons, which is due to their much higher effective mass.

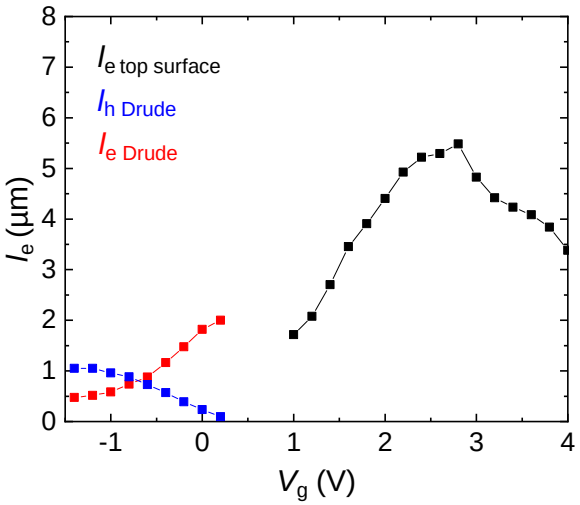

Fig. 4.6: Mean free path lengths calculated from charge carrier densities and mobilities from Fig. 4.5. With several µm of mean free path in the band gap and conduction band, we can consider our system as ballistic. n_s is not known precisely for bulk and bottom electrons and would have to be estimated. For details in the estimate of weighting the charge carrier densities, see the Supplementary of Ref. [114].

4.4 Landau level fan chart

In the previous section, we evaluated the properties of the different types of charge carriers. However, by analyzing Fig. 4.7, we will take a look at a large spectrum of V_g and B, ranging from deeply inside the VB to the beginning of the CB, and a magnetic field from zero to strong magnetic fields up to 5 T. Here, we observe that the charge carriers co-existing in distinct regions lead to a complex pattern in the Landau fan chart. In Ref. [114], several regions in the Landau fan are described. The respective data uncover a complex oscillation pattern with splitting, kinks, and crossings of Landau levels. These features occur in different sections of the (V_g, B)-parameter space, indicating that several groups of carriers are involved in the formation of Landau levels. The combined analysis of experimental data and simulations allows for a classification of six distinct regions within the $\sigma_{xx}(V_g, B)$-map. The regions differ by the type of carriers forming Landau levels, as well as by the magnitude of the magnetic field. The division into regions as described in [114] can now be transferred to our system. The plot for device e23 is shown in Fig. 4.7, where the second derivative $\partial^2\sigma_{xx}/\partial V_g^2$ is depicted for $0 \leq B \leq 5$ T and $-2 \leq V_g \leq 3$ V. The second derivative of the conductivity was chosen in order to increase resolution and visibility in the low-field region. In the following, the six regions are introduced. In fact, they fully reflect the previous discussion and thus confirm our findings. The

numbering of these regions refers to the one given in Ref. [114]. Here, we introduce the different regions in a modified order, which is more consistent with the approach chosen for this chapter.

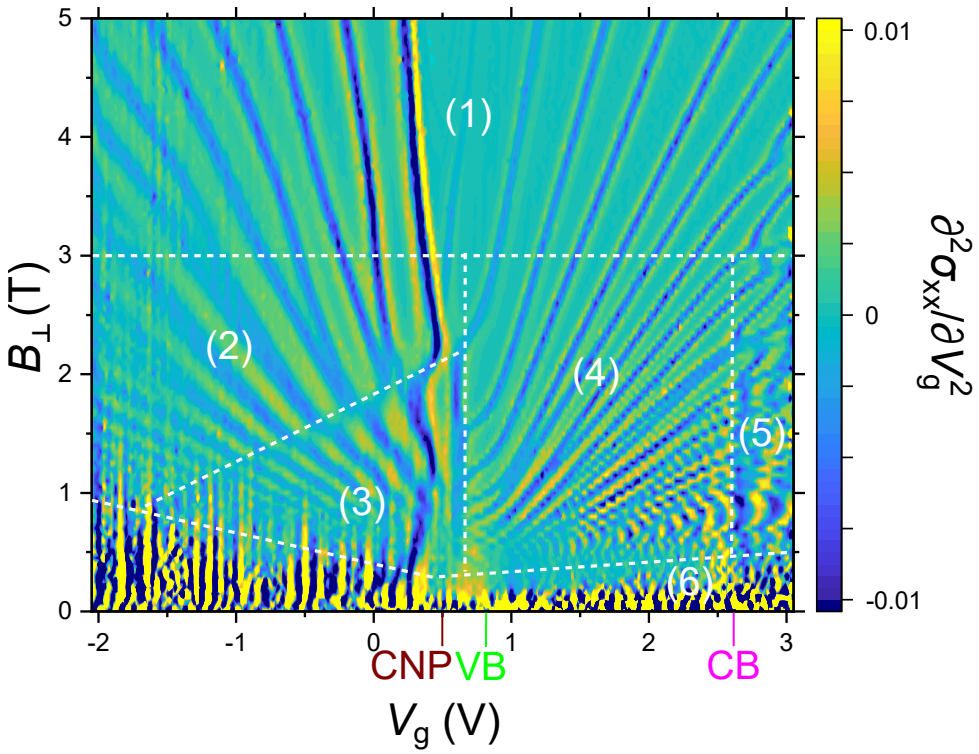

Fig. 4.7: Color map of the second derivative of the longitudinal conductivity $\sigma_{xx}(V_g, B)$ for $B_\perp = 0 - 5$ T in steps of 50 mT. Conductivity maxima appear as dark blue lines. The different charge carrier regions, as investigated in [114], are highlighted with white dashed lines. The valence (VB) and conduction band (CB) edges, and the charge neutrality point (CNP) are marked. The regions are assigned with numbers: (1): High magnetic field regime with hybridized states. (2): VB with less surface electrons than bulk holes contribution to transport. (3): Same as (2), with the difference of an intricate checkerboard pattern in region 3 caused by the co-existing surface electron and bulk holes to similar extent. (4): Energy band gap with only surface electrons contributing to transport. (5): CB with influence of surface and bulk electrons. (6): Drude regime with diffusive transport.

For $B_\perp > 3$ T (region 1), all charge carriers begin to form a hybridized QHE state with the filling factors determined only by the total charge density in the system $(n_s - p_s)$. The next region is the energy gap (region 4), where E_F lies in the energy gap so that only topological states on the top and bottom surfaces are present at the Fermi level, but no bulk states. At very small magnetic fields, i.e., in region 6, the Landau level separation is smaller than the Landau level broadening

and transport is fully diffusive. In this regime, the classical multi-component Drude model characterizes transport. No pattern can be distinguished within this area.

For all other regions ($B_\perp < 3$ T), several groups of carriers contribute partially to transport. In the valence band (regions 2 and 3), not only bulk holes determine transport, but also top and bottom surface electrons are present. However, only the top surface electrons participate in the formation of the observed oscillations. The bottom electrons have a fixed and small density (experimentally indistinguishable from zero). However, they do contribute to transport. In these two regions, bulk holes dominate the Landau spectrum, but coexist with surface electrons. This causes a complex checkerboard pattern in region 3. Interestingly, in region 2, the pattern is dominated by only one type of charge carrier, which is presumably represented by bulk holes. This can also be deduced from the broadened conductivity peaks, a consequence of a higher effective mass of holes. From Ref. [114], it follows that the separating line between regions 2 and 3 stems from the Landau fan originating from the top surface electrons.

In the conduction band (region 5), surface electrons and bulk electrons contribute to the spectrum. Thus, we observe two different sets of Landau levels, showing a checkerboard pattern, comparable to the one in region 3. This indicates the presence of several types of charge carriers, with none of them being negligible.

To conclude, the data confirm that each type of charge carrier type manifests itself in its own set of Landau fans. Depending on the regions, the Landau fans can cross and give rise to complex patterns. With these findings, we can now begin with the actual study of mesoscopic devices, which, as we will see, is largely influenced by the macroscopic behavior.

5. Conductance of QPCs in perpendicular magnetic fields

5.1 Motivation

In this chapter, point contacts made of a 3D TI, i.e., strained HgTe, are explored. In addition to the usual valence and conduction band charge carriers, transport in 3D TIs is determined by Dirac-type surface states that form a 2DEG "wrapped" around the bulk of the TI. The surface states are not spin degenerate and the spin of an electron is locked to its wave vector k [46]. Point contacts made in a 2D TI have been explored, demonstrating the typical sequence of conductance steps observed in a normal point contact in a 2DEG, except for an anomaly at the lowest conductance step [8]. Previous work on the conductance of long topological nanowires has demonstrated the existence of robust topological surface states [67]. However, point contacts in 3D TIs and potential quantization effects have not been explored yet.

For this purpose, QPCs with different geometrical parameters were studied systematically. The occurrence of anomalous, non-integer steps in the conductance is present in all QPCs investigated. Apart from that, a grouping of devices in preferred sequences of conductance steps suggests that these values are not due to coincidence. These findings are discussed both experimentally and theoretically. For the simulations of the experimental results, we cooperated with the group of Klaus Richter. The calculations presented in this work were performed by Michael Barth. A toy model describing the transmission and reflection of the number of transmitted modes is developed. For this purpose, the Landauer-Büttiker formalism is applied to the QPC system, describing the different contributions to the conductance. Finally, we elucidate the behavior for wide point contacts, approaching macroscopic dimensions. The most important findings of Secs. 5.2 to 5.5.4 have been published in Ref. [43]. Concerning the terminology in this chapter, we refer to the constant values in the conductance at QPCs as steps and in quantized macroscopic 2D systems as plateaus. However, these terms can be understood as synonymous. Unless otherwise specified, the conductance G refers to the longitudinal conductance measured at the QPC. It corresponds to G_{xx}, which we use, however, to express the conductance of the macroscopic part of the sample.

5.2 Anomalous, non-integer conductance steps

The results of 4-terminal longitudinal QPC conductance G measurements versus gate voltage V_g at $T = 80\,\text{mK}$, conducted over a wide range of magnetic fields (from 0 to 5 T) for device A1, are shown in Fig. 5.1. Throughout Chapters 5 and 6, we will refer to device A1 as the most representative device. Information about the devices are detailed in the Appendix B.2. At zero magnetic field, the measured conductance exhibits a value on the order of e^2/h, weak dependence on the gate voltage and an absence of quantized values. A reproducible yet orderless modulation is observed. Evidently, the structure under study is characterized by pronounced scattering. We attribute the latter to the sharp lithographic boundaries of the constriction or disorder.

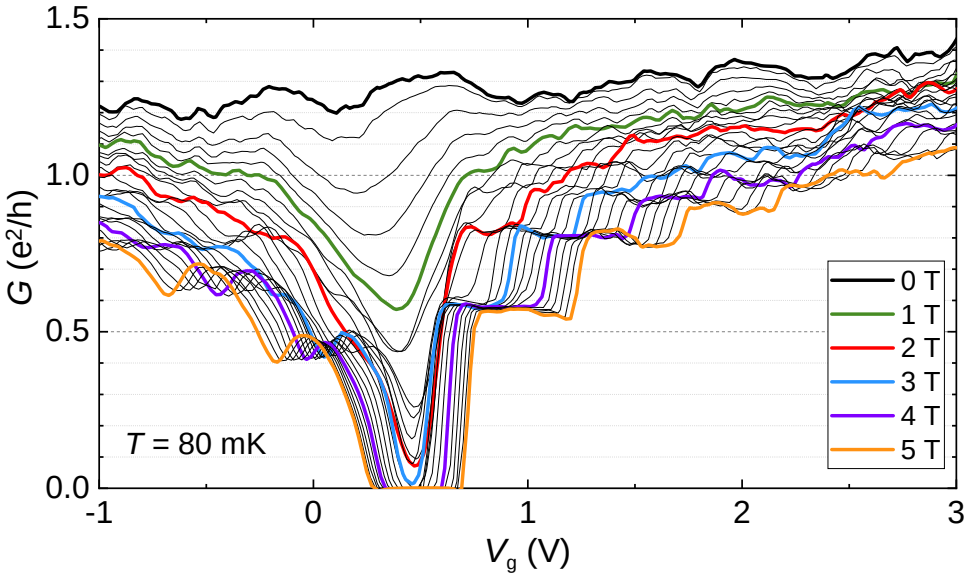

Fig. 5.1: QPC conductance $G(V_g)$ of device A1 for $B_\perp = 0 - 5$ T in steps of 200 mT. At $B_\perp = 0$, the conductance exhibits a value on the order of 1 e^2/h, weak dependence on the gate voltage and an absence of quantized values. For large magnetic fields, a sequence of steps emerges at anomalous, non-integer conductance values of 0.6 (step 1), 0.8 (step 2) and 0.9 e^2/h (step 3).

A common method to mitigate backscattering, both in the QPC and its vicinity, is to apply an out-of-plane magnetic field $B_\perp$ [116]. This is due to the prohibition of backscattering in magnetic fields, which can be understood using the edge channel model of the Landauer-Büttiker formalism. As the applied magnetic field increases, the measured conductance systematically decreases, while also displaying a clear dependence on the gate voltage. At $B_\perp = 3\,\text{T}$, when the macroscopic part of the

sample has already entered the QHE mode, distinct steps have developed in the conductance across the QPC on the electron side. Surprisingly, the steps do not appear at integer values of e^2/h, but rather at non-integer values of $0.6\,e^2/h$ for the first step and $0.8\,e^2/h$ for the second.

The presented curves demonstrate that the values of these steps remain consistent from their initial appearance to the maximum magnetic field of 5 T. This consistency suggests the presence of a scattering mechanism within the QPC, enabling a fixed fraction of electrons to traverse the device irrespective of the magnetic field strength. Although less pronounced, similar steps are observed on the hole side, where the current is primarily carried by valence band holes. However, we focus our analysis on the electron side in the following.

5.2.1 Robustness of steps

Previously, in Chapter 4, we have measured the Hall conductance G_{xy} in the macroscopic part of the sample, i.e., apart from the QPC. Together with the longitudinal resistivity, it was presented in Fig. 4.2. The perfectly quantized Hall curves confirmed the preservation of the high mobility and homogeneity of the 2DEG formed by the surface states, which dominate transport in the band gap and the CB. Fig. 4.2 has shown a well-developed QHE state already at $B_\perp = 3\,\mathrm{T}$ with precise G_{xy} quantization and all filling factors resolved, proving the high quality of the sample in the macroscopic reference area.

Now, we examine the response of the QPC conductance to temperature changes. The data presented in Fig. 5.2 (a) clearly show that a temperature change from 80 mK to 800 mK maintains the step position. Measurements on sample A3 up to 10 K (see Fig. 5.2 (b)) additionally confirmed the weak temperature dependence of the steps. A significant effect of temperature was only observed at $T > 5\,\mathrm{K}$, when the steps begin to smear, and the conductance at the charge neutrality point at about 0.5 V also increases due to trivial activation. The latter is caused by the smearing of the Fermi-Dirac distribution function with increasing T [45].

The insensitivity of the observed steps to temperature changes suggests a lack of connection with the 0.7-anomaly [117], which depends on T. If we observed the 0.7-anomaly in our system, the non-quantized conductance steps would become more pronounced by increasing T, whereas the integer conduction plateaus would be blurred by thermal smearing [118]. In the present case, however, although conductance fluctuations vanish with heating, the steps remain clearly visible. This implies the probable single-electron nature of the scattering responsible for the anomalous conductance quantization.

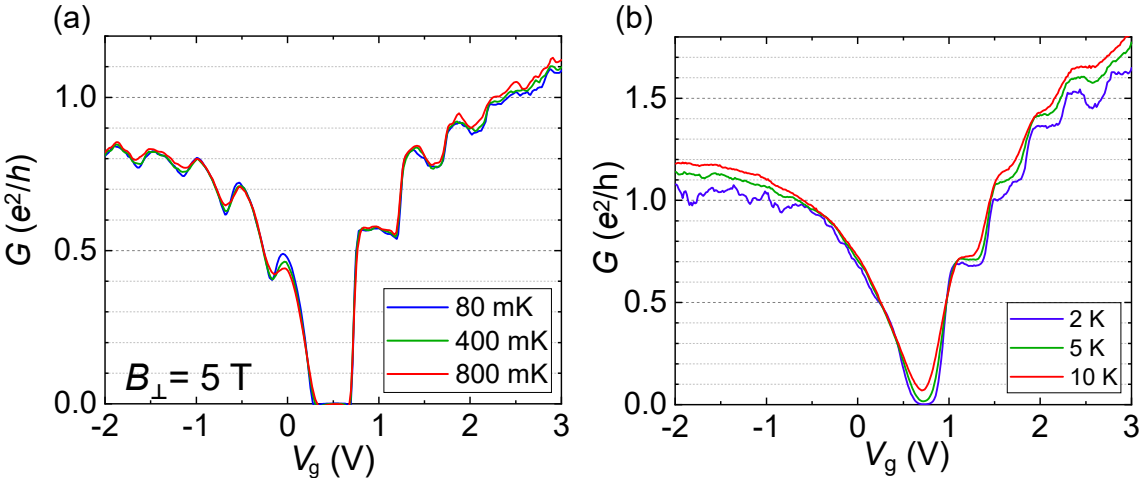

Fig. 5.2: Conductance for different temperatures between (a) 80 mK and 800 mK for device A1, and (b) 2 and 10 K for device A3, both at $B_\perp = 5$ T. The insensitivity of the step position to temperature indicates the single-electron nature of the phenomenon. Due to trivial activation, only at $T \geq 5\,\mathrm{K}$, the steps begin to smear, and the conductance at the CNP at about 0.5 V also increases.

5.3 Grouping of devices

5.3.1 Situation at zero magnetic field

Approximately a dozen QPCs with cross sections varying by more than one order of magnitude was studied throughout this thesis. In Fig. 5.3, the measured conductance without applying a (perpendicular) magnetic field is shown. The conductance of the devices at zero magnetic field ranges from 1 to $100\,e^2/h$. However, no signs of quantization are present. Interestingly, the measured $G(V_\mathrm{g})$ dependences are not uniformly distributed across the conductance range, but rather appear in groups. Here, we introduce three distinct groups based on their conductance values: For group A, we observe a grouping at conductance of approx. $1-2\ e^2/h$, for group B approx. $4-10\ e^2/h$, and for group C approx. an averaged $30\ e^2/h$ and more. We assign the colors red to group A, blue to group B and purple to group C. Each examined device can be assigned to one of these groups, with none falling into the gaps between them. Two cases can be regarded as exceptions (devices C1 and C2), which are not classic QPCs but long wires with lengths of 1.5 and 2.5 µm. These behave differently at $B_\perp = 0$, their conductance increases significantly from approx. 10 to $\approx 50\ e^2/h$ in the measured V_g range. Later, when a magnetic field is applied, their assignment to group C becomes more evident. For the moment, we consider them as a limiting case.

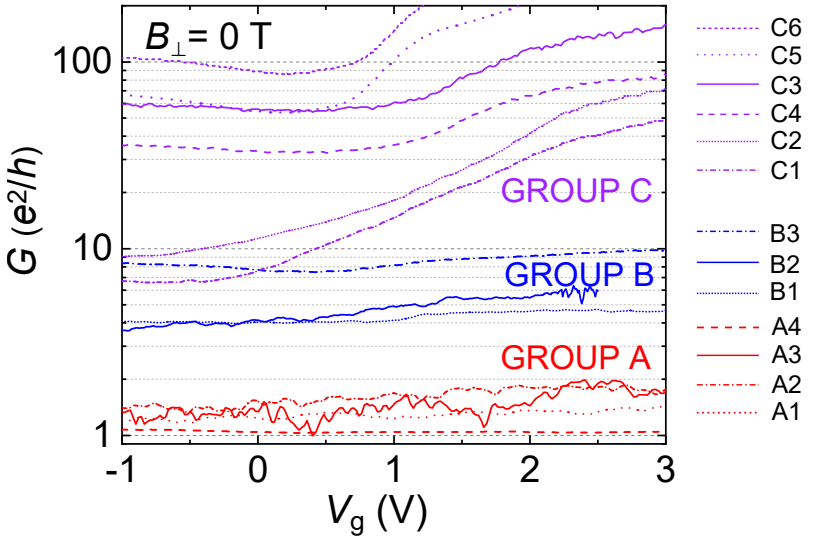

Fig. 5.3: Conductance $G(V_g)$ of the devices under study at $B_\perp = 0$. The observed $G(V_g)$ dependences are categorized into three distinct groups based on the conductance value: Group A (red, $G = 1 - 2\,e^2/h$), B (green, $4 - 10\,e^2/h$), and C (purple, $> 30\,e^2/h$). Each device analyzed unequivocally belongs to one of these groups, with none falling into the intermediate regions. Only the devices C1 and C2 behave slightly different, as they represent a transition between group B and C. In these cases, the wires are long wires instead of short QPCs. $T = 80$ mK -1.5 K for the different devices.

A list of the devices under study, indicating their later classification into groups (e.g., device A1, with A indicating the belonging into group A), is given together with their geometrical parameters in Fig. 5.4 (a). The area of the cross section is calculated from height and width of the QPCs at the narrowest point (for simplicity, we assume a rectangular shape). A distribution of the cross section areas highlighting the affiliation to the corresponding groups is shown in (b). Here, we observe that no clear separation with respect to the cross section is visible. Rather, it shows a distribution with overlap between the groups.

(a)

device	w (nm)	h (nm)	A (nm^2)
A1	580	30	17 400
A2	140	50	7 000
A3	95	50	4 750
A4	85	50	4 250
B1	710	30	21 300
B2	200	50	10 000
B3	135	80	10 800
(C1	580	50	29 000)
(C2	580	50	29 000)
C3	1 000	50	50 000
C4	2 000	50	100 000
C5	5 000	80	400 000
C6	10 000	80	800 000

(b)

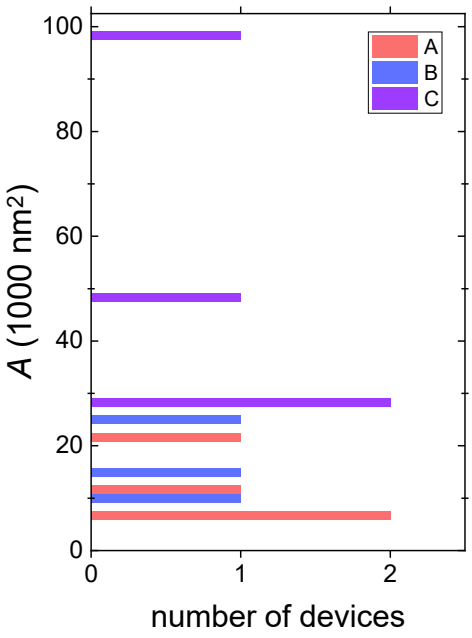

Fig. 5.4: (a) List of the QPC devices under study with geometrical parameters width w, height h and cross section A. Devices C1 and C2 do not represent point contacts, but rather long wires with $l \approx 2$ µm. (b) Histogram showing the attribution of devices to groups A, B and C in dependence of the cross section A. Only devices up to $A = 100\,000$ nm^2 are included. The groups show overlaps in the size ranges. Nevertheless, there is a recognizable trend that groups A, B and C have a preferred range of values regarding A.

5.3.2 Comparison of different devices in a perpendicular magnetic field

Fig. 5.5 shows the dependence of $G(V_g)$ in a magnetic field ranging from 0 to 5 T for device B1 from group B. What distinguishes group B QPCs from group A, is the sequence of step heights in a magnetic field. Apart from this, the steps show an oscillation-like pattern, which was less pronounced for group A devices (see Fig. 5.1). This pattern is a hint towards the beginning of the formation of SdH-like peaks, as observed for macroscopic devices. Later in Sec. 5.6, when studying wide point contact devices, we will see very clear oscillation-like behavior. Therefore, we can consider group B as an intermediate state between group A, showing no oscillations, and group C, showing rather oscillations than steps in the conductance.

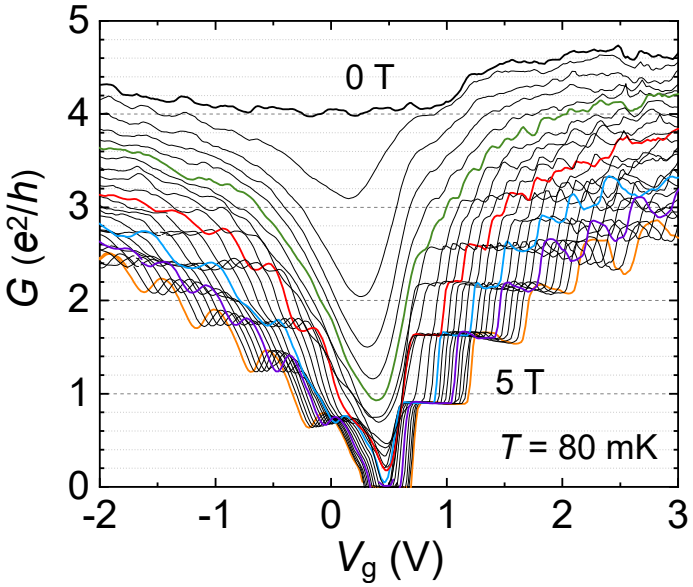

Fig. 5.5: Longitudinal conductance $G(V_g)$ for device B1 fom group B, measured for magnetic field values ranging from $B_\perp = 0$ to 5 T in increments of 200 mT. At $B_\perp = 0$, the conductance exhibits a value on the order of $4 - 5\ e^2/h$, again as device A1 already weak dependence on the gate voltage and an absence of quantized values. For large magnetic fields, a sequence of steps emerges at anomalous, non-integer conductance values of approximately 0.85 (step 1), 1.5 (step 2) and $2.2\,e^2/h$ (step 3). For the study of wide point contacts in Sec. 5.6, it is of interest that a slight oscillation-like behavior begins to emerge.

While the grouping at zero magnetic field may have seemed unconvincing, the presence and distinction of the groups become clear at $B_\perp > 0$. In the following, we will compare the devices from group A and B among each other at $B_\perp = 5$ T. Fig. 5.6 (a) compares the step sequence of a representative device from group A, A1, with that of a representative from group B, B1. These distinct step sequences are representative of the behavior of all devices in groups A and B. The comparison of $G(V_g)$ at $B_\perp = 5\,\mathrm{T}$ shows that the step heights for device B1 are significantly higher than those for device A1.

In Fig. 5.6 (b), curves for different devices, all belonging to group A, are shown for comparison, at strong magnetic field ($B_\perp = 5$ T). It should be mentioned that two of these devices (red and blue curve, A2 and A3) stem from the same sample, e23, sharing the same parameters except their width. In particular, they are connected by the same Hallbar, so that the material system can be regarded as truly identical, also with respect to the fabrication history. The third device, A1 (black), although having a different height and much larger width than the first two devices (with an approx. four times larger cross section), replicates the behavior in a very similar sequence of conductance steps. While it is less surprising for devices A2 and A3, which stem from the same MBE-grown material system, the observed behavior for

device A1 clearly demonstrates a preferred scattering mechanism which can not be traced back only to the geometry, especially the size of the cross section of the QPCs. It should be noted that the positions of the valence and conductance band edges differ, as we compare different material systems.

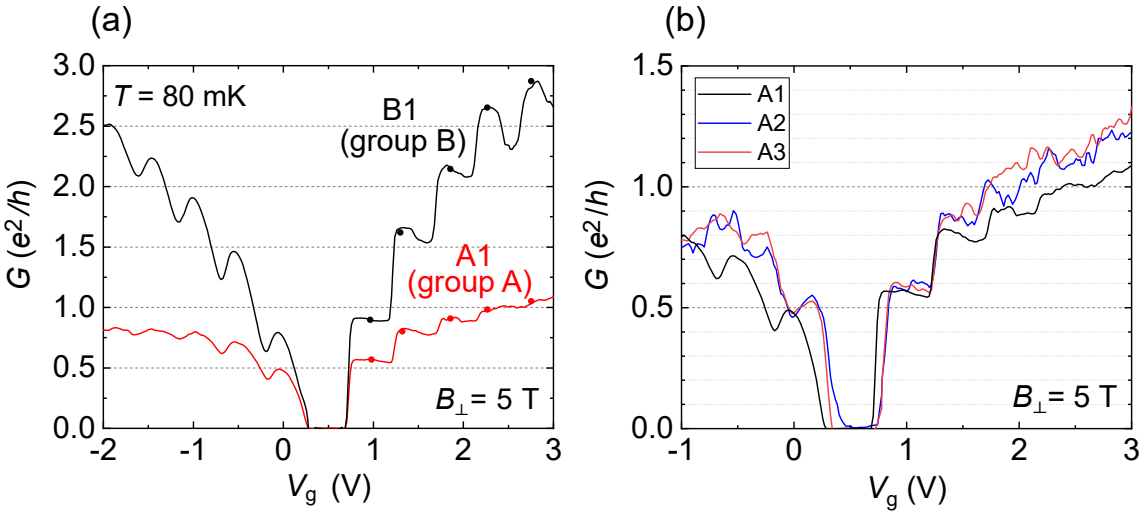

Fig. 5.6: Comparison of conductance step sequences of group A and B: (a) Comparison of $G(V_g)$ for devices A1 and B1, measured at $B_\perp = 5$ T. (b) Comparison of three devices from the same group (A): A1 ($w = 580$ nm, $h = 30$ nm), A2 ($w = 95$ nm, $h = 50$ nm), and A3 ($w = 140$ nm, $h = 50$ nm).

For better comparability between the devices from different material systems, we plot the conductance step heights as a function of the step number instead of V_g. Here, the separation into groups becomes even more evident. This is shown in Fig. 5.7.

- Of all the devices studied, the ones in group A (red) exhibit their first conductance step at approx. $0.55 - 0.6\ e^2/h$, second at $0.85\ e^2/h$, third at $1\ e^2/h$ and fourth at $1.1\ \mathrm{e}^2/\mathrm{h}$, in large magnetic fields.

- Group B (green) devices have their first conductance step at approx. $0.85\ \mathrm{e}^2/\mathrm{h}$, the second one at $1.5\ e^2/h$, the third one at $2.2\ e^2/h$ and the fourth one at $2.6\ e^2/h$.

- Group C (violet), which will be discussed in more detail in Sec. 5.6, covers a wide range, showing rather oscillation-like behavior typical of macroscopic devices. The first conductance step starts at approx. $1.3\ e^2/h$, second at $2.8\ e^2/h$, and third at $5\ e^2/h$. These devices share a width exceeding 700 nm.

At latest here, the grouping tendency becomes very clear: the difference in step height between samples in group A and group B is an order of magnitude larger than the difference within each group. Thus, all small and medium-sized QPCs do not exhibit a wide range of conductance values but rather fall into one of two groups, each with predetermined behavior in a magnetic field. Falling into either group A or B seems to correlate with the QPC cross-section. However, unlike the behavior of the conductance within each group, there is a notable uncertainty and overlap between the groups: samples in group A are characterized by cross-sections ranging from $0.5 \cdot 10^4$ to $1.8 \cdot 10^4\,\mathrm{nm}^2$, while in group B the cross-section varies from 10^4 to $2 \cdot 10^4\,\mathrm{nm}^2$. The specific distribution of electrical charge within the QPC can act as a random and unpredictable factor influencing the tendency to belong to one of the groups.

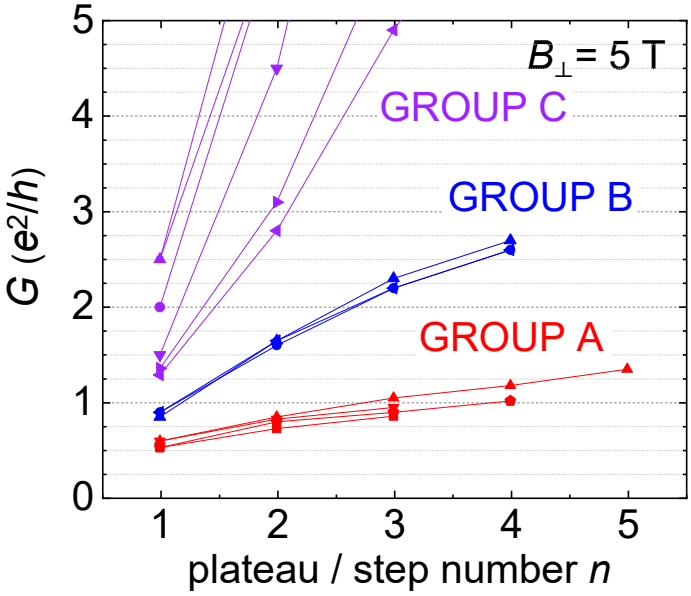

Fig. 5.7: Dependence of the conductance step G on the step number. The devices are categorized into three groups. A grouping at preferred values is observed for all devices from groups A and B. For group C, oscillation-like behavior prevails, with residues of conductance steps at the oscillation minima. The latter were used here as the value of the conductance step. The temperature ranges between $T = 80$ mK and 1.5 K for the different devices.

Group C is distinguished not only by step heights larger than e^2/h, but also by significant variation in this value (see Fig. 5.7). However, devices in this group possess such high conductance that they no longer adhere to the characteristics of QPCs. Rather, they mark a transition to a macroscopic 2D system with a constriction. This transition is reflected in the altered form of $G(V_\mathrm{g})$, showcasing oscillations reminiscent of Shubnikov-de Haas phenomena rather than magnetic field-induced steps (see Sec. 5.6). In the following, our focus remains on samples from groups A and B in Secs. 5.4 to 5.5.4 exclusively.

5.4 Partial transmission of modes through the QPC

In the following, we analyze the correlation between the conductance step values across the QPC and the quantum Hall steps outside the QPC as a function of $B_\perp$ and V_g in Fig. 5.8 (a). The steplike behavior of $G(V_\mathrm{g}, B_\perp)$ is evident from the abrupt color changes in Fig. 5.8 (a), with the step numbers indicated by the white labels. The differently colored segments form a fan that originates at the charge neutrality point. Although the conductance values differ, this fan closely matches the one shown in Fig. 5.8 (b), which visualizes the quantum Hall steps. For $B_\perp > 3\,\mathrm{T}$, the Hall conductance exhibits quantized values given by $\nu e^2/h$, thus reflecting the filling factor ν. This demonstrates that the step number in the QPC conductance reflects the number of filled Landau levels in the macroscopic regions outside the QPC, and, accordingly, the number of edge channels potentially flowing through the QPC. Since each edge QHE state has a conductance of e^2/h, and the height of the steps in G is always smaller than e^2/h, it indicates that the QPC acts as a filter, partially transmitting the edge states from one side of the QPC to the other, i.e., from the left-hand side macroscopic reservoir to the right-hand side, or vice versa. Simultaneously, this transmission coefficient of this filter remains practically unchanged within one step, i.e., in the magnetic field range from 3 to 8 T.

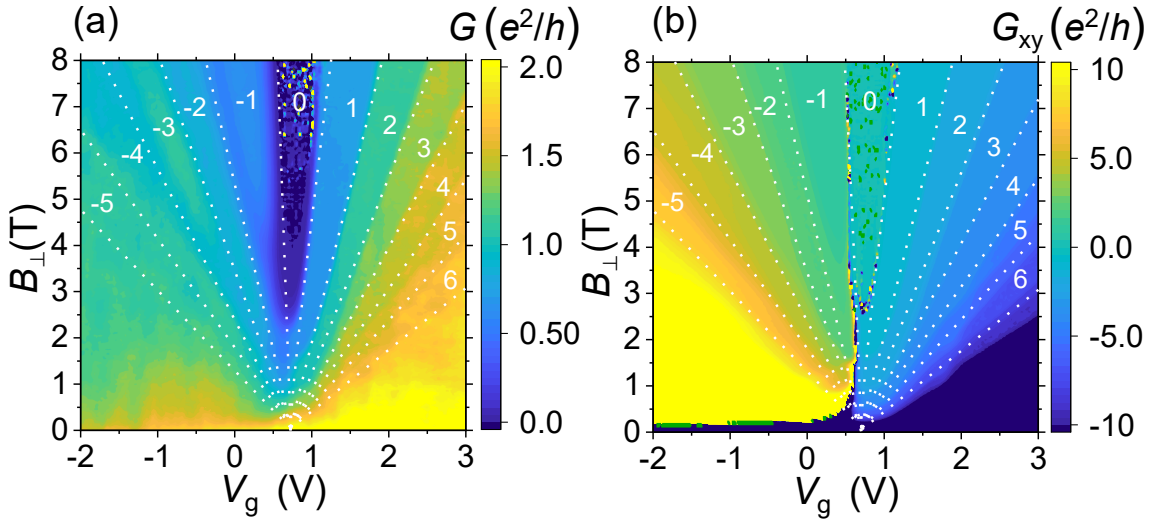

Fig. 5.8: The QPC as a filter. Color plots of (a) the longitudinal conductance of device A3 and (b) the macroscopic Hall conductance. The conductance is measured in dependence of V_g for $B_\perp = 0 - 8$ T in steps of 50 mT. Comparing the conductance across the QPC in (a) with the conductance of the macroscopic part in (b), we observe that transitions between steps occur at the same positions in both the QPC and the macroscopic part, determined by the filling factor of the bulk. This suggests that the QPC acts as a filter, allowing only a portion of the individual edge states from the macroscopic part of the sample to pass through.

In a first attempt to model the unusual sequence of steps, we resort to the Landauer-Büttiker (LB) formalism. In this formalism, the conductance of a multiterminal system in quantizing magnetic fields is expressed in terms of the transmission and reflection coefficients of the individual edge channels. The transmission coefficient t of a QPC represents the number of one-dimensional states that successfully pass through it. For our case, we consider the 6-terminal device shown in Fig. 5.9. The contacts are numbered from 1 to 6, where contacts 1 and 4 serve as the source and drain, respectively, while the remaining contacts function as voltage probes. For integer QHE filling factors, transport occurs along edge states, with the number of edge states denoted as N. Each edge state has a conductance of e^2/h. In one magnetic field orientation (either up or down in perpendicular direction with respect to the sample plane), these states propagate along the sample edges in a clockwise or counterclockwise direction. Consequently, N states flow from source 1 to contact 6. From contact 6, these N states move towards the QPC, where they are split into t states that pass through the QPC and r states that are reflected towards contact 2, with the condition $N = t + r$. The deviation of the conductance steps from integer multiples of e^2/h, as in our experiments, indicates that t (and consequently r) are not integers.

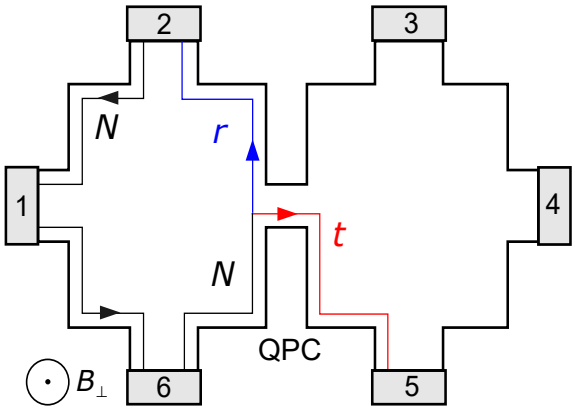

Fig. 5.9: Diagram of the multi-terminal device (not to scale) used to calculate the transmission coefficient t in the Landauer-Büttiker formalism. Out of N incoming edge states (black), an amount t is transmitted (red) while r edge states are reflected (blue). The mechanism is shown only on one side of the QPC (from left to right).

Within the LB formalism, the conductance across the QPC is given by

$$G = \frac{e^2}{h}\frac{Nt}{N-t} = \frac{e^2}{h}\frac{Nt}{r}. \tag{5.1}$$

For the deduction, see Appendix C.1. From this, we can derive the transmission coefficient

$$t = \frac{g \cdot N}{N+g}, \tag{5.2}$$

where $g = G/(e^2/h)$. Using $N = G_{xy}/(e^2/h)$, we can derive t from the experimental data. This is depicted for sample A1 in Fig. 5.10. The plot shows that the transmission at the first step is $t \approx 0.38$ for device A1, and $t \approx 0.46$ for device B1. This means that (in the case of device A1) of one single edge channel, 38 % is transmitted and 62 % is reflected at the QPC. If we insert t of each step and device, respectively, into Eq. (5.1), we obtain the correct values of G, which confirms the accuracy of the model. As the number of steps increases, the transmission is not proportional to the number of steps, but grows sublinearly.

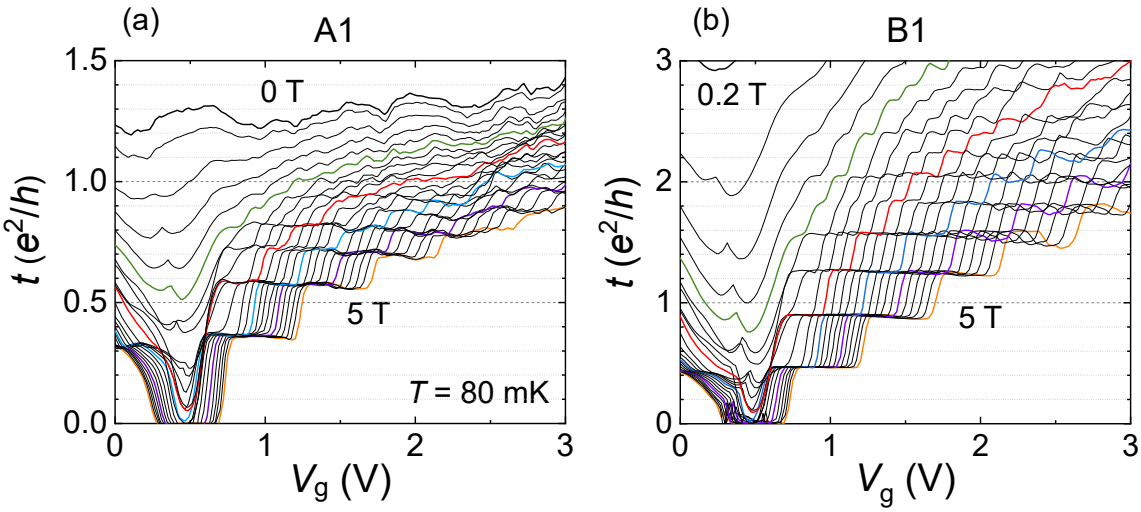

Fig. 5.10: The transmission coefficient $t(V_g)$ for (a) device A1 and (b) device B1, calculated from the measured values of $G(V_g)$ and $G_{xy}(V_g)$ over the range $B_\perp = 0{-}5$ T in steps of 200 mT. $B_\perp = 1, 2, ...5$ T is highlighted. (For device B1, $B_\perp = 0$ T is not shown, in order to keep the range of the y-axis detailed enough.) t indicates the actual number of transmitted modes rather than, as might intuitively be assumed, the conductance.

Experimentally, t can also be determined by measuring the diagonal conductance which is given by

$$G_d = \frac{e^2}{h} t. \tag{5.3}$$

This can be deduced from the Landauer-Büttiker model for our system (for details, see Appendix C.1). In Fig. 5.9, the diagonal signal is measured between contacts 6 and 3. The resulting picture is not intuitive at all. It demonstrates that, in fact, G does not illustrate the number of modes transmitted. Instead, this is done by t, or G_d, respectively. The conductance G, in contrast, describes transport in the form of Eq. (C.3) for a multi-terminal system, based on the Landauer-Büttiker formalism. It measures the relation $G = I_{14}/U_{23}$ of the current I_{14} between source and drain (contacts 1 and 4) to the voltage drop U_{23} between contacts 2 and 3. In its limit of zero voltage drop, it would reach infinity. Therefore, the conductance stands in

contrast with the conductivity $\sigma_{xx} = \frac{\rho_{xx}}{\rho_{xx}^2+\rho_{xy}^2}$, which describes transport considering a bulk conductivity of the system.

5.5 Simulations

5.5.1 The two-dimensional effective model

In order to gain insight into the possible origins of the non-integer quantized conductance steps, numerical tight-binding calculations were performed by Michael Barth, presented in the following. For this purpose, the Python package KWANT was employed [119]. Note that a full 3D model is not tractable in transport simulations for the experimentally studied system dimensions, where a schematic illustration is shown in Fig. 5.9. As the experiment exhibits signatures of the 2D quantum Hall effect in strong magnetic fields, we employ a simplified effective model which describes a 2D electron conduction band. The valence band will not be taken into account. The Hamiltonian which we consider is given by

$$H = \frac{\hbar^2}{2m_e}\left(k_x^2 + k_y^2 - \mu + V(x,y)\right)\sigma_0 + \alpha_R(k_x\sigma_y - k_y\sigma_x) + \frac{1}{2}g^*\mu_B B_\perp, \tag{5.4}$$

where we include a Rashba-type spin-orbit coupling term, a Zeeman term and a spatially dependent scattering potential, $V(x, y)$. For all of the shown calculations, we fixed $m_e = 0.06m_0$ with m_0 being the free electron mass, the Rashba coefficient is set to $\alpha_R = -0.015$ meV nm and the effective g^*-factor to $g^* = 22.7$ [96, 120, 121]. The Hamiltonian H is then discretized via the finite difference method on a discrete square lattice with width w' and length L. This lattice is constricted by the QPC, as illustrated in Fig. 5.11.

In the following, we will introduce all relevant geometric parameters, most of them depicted in Fig. 5.11. The lattice constant is fixed to $a = 2$ nm throughout this work. This value stems from the effective tight-binding description, which is not based on the physical atomic lattice. It refers purely to the numerical lattice, where the lattice constant is arbitrary. Next, we attach four vertical and two horizontal leads to construct a six-terminal setup, as shown in Fig. 5.9. The latter have the same width as the central scattering region, while the former are separated from the horizontal leads by the distance d_v and have a width w_v. Additionally, we include the perpendicular magnetic field $B_\perp$ via standard Peierl's substitution [122], where we fix the gauge to $\mathbf{A} = (0, B_\perp x, 0)$. Finally, we define the etched QPC region by defining elliptic areas stretching from the edges in the central part of the scattering region. This is done by simply deleting sites that meet the conditions

$$\frac{(x - L/2)^2}{(\xi_x)^2} + \frac{y^2}{(\xi_y)^2} < 1, \tag{5.5}$$

and

$$\frac{(x - L/2)^2}{(\xi_x)^2} + \frac{(y - w)^2}{(\xi_y)^2} < 1. \tag{5.6}$$

The parameters ξ_x and ξ_y tune the spatial extent of the etched regions. The width of the central QPC region is then given by $w_{\mathrm{QPC}} = w' - 2\xi_y$. We will use w_{QPC} only in this section in the context of simulations. In the rest of this work, we refer to the experimentally measured width of the QPCs as w.

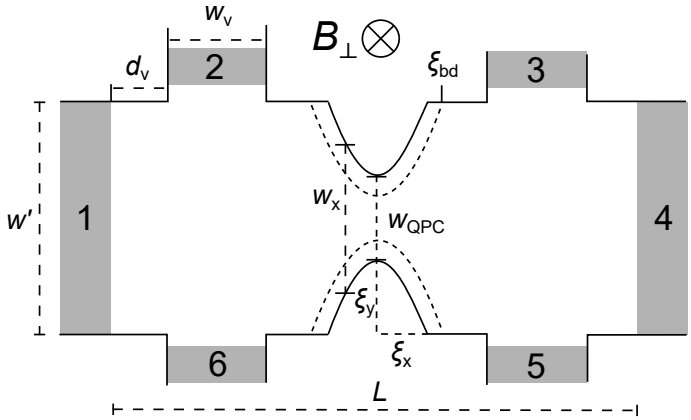

Fig. 5.11: Hall bar schematic considered in the tight-binding simulations illustrating the important lengths and geometric parameters: w_{QPC} is the width of the central QPC region; ξ_x and ξ_y define the spatial extent of the etched regions. The leads to the six-terminal setup are given by their width w_v for the horizontal leads $(2, 3, 5, 6)$ and w' for the vertical leads (1 and 4). The vertical leads are separated from the horizontal leads by the distance d_v. ξ_{bd} defines the penetration depth of the etching-induced disorder close to the boundaries. The parameters were introduced by Michael Barth.

However, for the studied QPC widths, the coupling induced by the pure geometric confinement between the emerging edge states is not sufficient to show any scattering and therefore a finite longitudinal resistance. Therefore, we make the assumption that the etching procedure not only shapes the device but also affects the potential landscape of the QPC zone. For simplicity and to be as general as possible, we include such an effect using white noise random on-site potential $V(x, y)$. An on-site potential is an additional energy value that can be set to each grid point in the simulation. In the simplest case, it is a random value drawn normally distributed from an interval. Such a term breaks translation invariance and accordingly leads to scattering. Thus, it is added to the Hamiltonian and enters the tight-binding calculation.

We allow for the disorder to consist of two distinct parts. On the one hand, $V_{\mathrm{bulk}}(x, y)$ describes the disorder which is already present in the material before the etching procedure and its magnitude is tuned by the value K_{bulk}. This component

is probably very small, as the studied mesas exhibit very long phase coherence lengths [49]. The second component, namely $V_{\text{edge}}(x, y)$, describes the disorder which is induced by the sample production and the strength is tuned by K_{edge}. We want to highlight that the above choice of the disorder potential is only done by assuming a smooth scaling of white noise when approaching the etched areas. Still, it suffices to show that simple on-site disorder can lead to the formation of robust steps in the longitudinal conductance. The potential $V(x, y)$ is defined as

$$V(x, y) = V_{\text{edge}}(x, y) f_y(x, y) f_x(x) + V_{\text{bulk}}(x, y), \tag{5.7}$$

with

$$\begin{aligned} f_y(x, y) = 0.5\{&- \tanh[s_y(y - e(x, y) - \xi_{bd})] + \\ &\tanh[s_y(y + e(x, y) - w_x + \xi_{bd})]\} + 1, \end{aligned} \tag{5.8}$$

$$\begin{aligned} f_x(x) = 0.5\{&\tanh[s_x(x - L/2 + \xi_x)] - \\ &\tanh[s_x(x - L/2 - \xi_x)]\}, \end{aligned} \tag{5.9}$$

with w_x describing the x-dependent width of the geometry, as etching narrows the system in the x-direction, and

$$V_{\text{edge}}(x, y) = K_{\text{edge}} n(x, y) \tag{5.10}$$

$$V_{\text{bulk}}(x, y) = K_{\text{bulk}} n(x, y). \tag{5.11}$$

The parameters s_x and s_y tune the smoothness of the potential scaling, while ξ_{bd} defines a quantity that can be best described as the penetration depth of the etching-induced disorder close to the boundaries. Additionally, $e(x, y)$ is an offset determined by the edge parametrization given Eq. (5.5). Finally, $n(x, y)$ corresponds to random numbers which are drawn from a uniform distribution in $[0, 1)$.

We also implemented a more system-specific model for HgTe quantum wells, the so-called Bernevig-Hughes-Zhang (BHZ) model [93], which would allow to study topological states in a bulk band gap. The effective model describes a pure electron band without an associated valence band and without topological properties. The BHZ model is closer to a real 2D HgTe system. Qualitatively, however, the differences in terms of Hall conductivity are minor. Since no traces of such states were observed in experiment and both models give qualitatively similar results, we focus on the simpler system given by Eq. (5.4). In Sec. 5.5.3, we will briefly consider the results from the BHZ model and compare it to the 2D effective model, and explain in more detail why we have chosen not to consider it further as an adequate model. In the following, we continue with the effective model.

Now, we calculate the conductance components by solving numerically the equation

$$\mathbf{I} = \langle \hat{\mathbf{G}} \rangle_D \mathbf{V}, \tag{5.12}$$

where $\mathbf{I}$ and $\mathbf{V}$ are vectors containing all currents and voltages in the setup. A detailed deduction for all contributions to the conductance is given in the Appendix C.1. We define leads 4 and 5 as current probes, such that $\mathbf{I} = (I, 0, 0, -I, 0, 0)$ and set $V_4 = 0$. Furthermore, $\langle . \rangle_D$ denotes an averaging over D disorder sets. It is actually important to average first the full conductance matrix and solve then Eq. (5.12). Otherwise, by solving first the equation for each disorder set and averaging then the extracted longitudinal conductance leads to numerical divergences for small numbers of edge states. The reason for that lies in the relation $G_{I,U} = G_{14,56} = G_{xx} = \frac{e^2}{h} \frac{Nt}{N-t}$ [123] (for conduction band edge states), where t corresponds to the number of edge states which are transmitted through the QPC. This equation is equivalent to the expression for $G(N, t)$, introduced previously in Eq. 5.1. We observe that whenever t is close to N, we obtain a very small denominator, leading to a divergence of G_{xx}. Those contributions cannot be removed by an adequate number of disorder averages. Here, it also becomes obvious that $N = t$ cannot be fulfilled in real QPC systems. The denominator of Eq. (5.1) would then become 0, leading to an infinitely high conductance. This has no physical basis, but is the result of artificially introducing the quantity G on the basis of the LB formalism. As the QPC introduces an additional potential to the macroscopic system, not all of the N edge states can be transmitted. In fact, this is the intrinsic motivation of a QPC device.

5.5.2 Numerical modeling

For the numerical simulations, we first fix the following geometric system parameters that are valid for all the results shown. We will consider a setup with a width of $w = 500$ nm and a length of $L = 1600$ nm. Then, we attach vertical leads of width $w_v = 250$ nm and $d_v = 200$ nm. Next, we define the QPC region by fixing $\xi_x = 50$ nm and $\xi_y = 150$ nm such that we obtain a QPC width of $w_{\mathrm{QPC}} = 200$ nm. This value was chosen because it is closer to the overall experiment and represents an approximate mean value among the devices in group A. Basically, it is of little significance which width is chosen, as in this case only the magnetic field has to be chosen stronger or weaker. Simulations for $w = 100$ nm yielded very similar results. We set the magnetic field strength to $B_\perp = 5$ T, which results in a magnetic length of $l_B = \frac{\hbar}{eB_\perp} = 11.47$ nm. Therefore, we expect the emergence of quantum Hall states in the QPC area. For the etching-induced disorder, we set $\xi_{bd} = 110$ nm, $s_x = 0.1$, $s_y = 0.05$, and $K_{\mathrm{edge}} = 0.95\ t$ with $t = \hbar^2/(2m_e)$. The bulk disorder contribution is defined by setting $K_{\mathrm{bulk}} = 0.002\ t$. In Fig. 5.12, we display an example disorder profile.

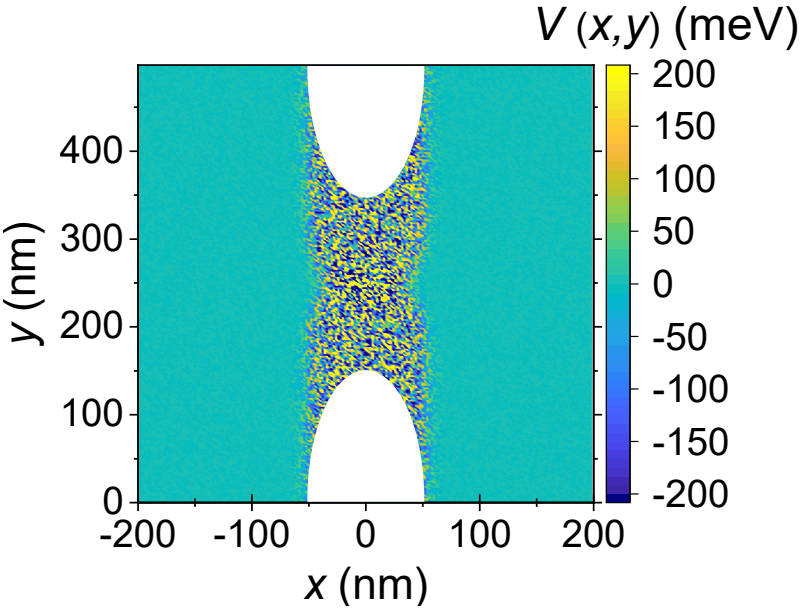

Fig. 5.12: An example of the electrostatic potential disorder distribution in the QPC region with the width $w_{\mathrm{QPC}} = 200$ nm, used for the conductance simulations. It is assumed to be generated by the etching procedure. Calculations performed by Michael Barth.

In the following, we consider group A devices in the calculations. However, the modeling is possible also for group B. For this group, the amplitude or the spatial extent of the disorder potential would have to be reduced so that everything becomes more homogeneous and thus the scattering also decreases. Finally, disorder averaging over 200 disorder sets to avoid conductance signatures related to an individual disorder potential was performed by Michael Barth. The results of these transport simulations are illustrated in Fig. 5.13, where different conductance components vs. the chemical potential μ are plotted. We show the absolute value of transversal Hall conductance, $|G_{xy}| = |G_{14,35}|$ (black), the longitudinal conductance $G_{xx} = G_{14,23}$ (blue), and the diagonal conductance $G_d = G_{14,25}$ (green). The results exhibit well-quantized quantum Hall plateaus in $|G_{xy}|$ with multiples of $\frac{e^2}{h}$. Concerning the longitudinal conductance, G_{xx}, we observe plateau-like structures, where the conductance is quantized in non-integer values of $\frac{e^2}{h}$. Furthermore, the increase in conductance from step to step is not given by a fixed constant. Small remaining fluctuations reflect the finite number of 200 disorder averages, which would be reduced further by including more disorder sets. Still, the scattering of edge states in the energy range between two Landau levels appears to be independent of the chemical potential μ (proportional to the gate voltage) in the numerical data. Analogously, the diagonal conductance shows step-like features, and, as mentioned above, it is equivalent to the number of transmitted edge states t. Therefore, our results demonstrate that, indeed, transmission is increasing in steps. Summarizing, we see that disorder in the QPC

area can lead to clear step-like conductance features with non-integer quantization in terms of e^2/h, reproducing the measurements.

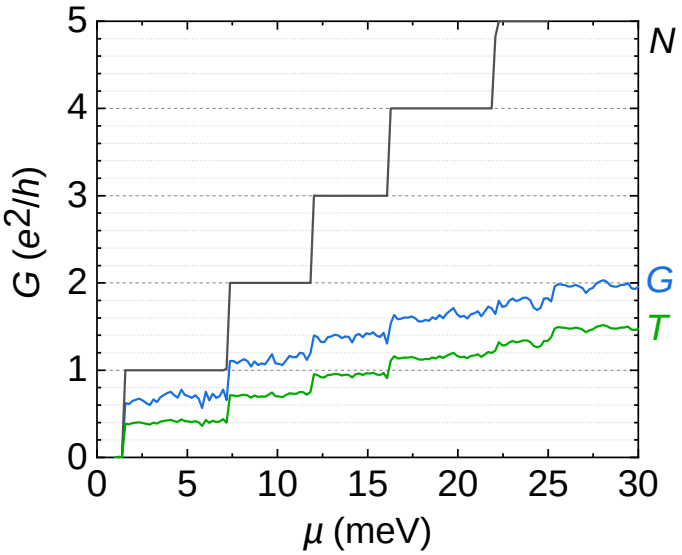

Fig. 5.13: Numerically computed conductances employing the effective 2D model in Eq. (5.4) for the Hall bar setup with $w = 200$ nm as illustrated in Fig. 5.9 vs. chemical potential μ at $B_\perp = 5$ T. The Hall conductance $G_{xy} = N$ (black), the longitudinal conductance at the QPC $G = G_{\mathrm{QPC}}$ (blue), and the diagonal conductance $G_d = t$ (green) are depicted. G_{xy} shows a non-spin-degenerate step-like structure with integer multiples of e^2/h (denoted as N). Calculations performed by Michael Barth.

5.5.3 Simulations based on the 2D Bernevig-Hughes-Zhang model

As mentioned previously, we also implemented a more system-specific model for HgTe quantum wells, the two-dimensional Bernevig-Hughes-Zhang (BHZ) model [93], which allows to study topological states in a bulk band gap. However, no traces of such states were observed in this work (in contrast to the work of Johannes Ziegler [49], which showed the presence of topological surface states in HgTe wires). Furthermore, both, the 2D BHZ model and the 2D effective model, yield qualitatively similar results. For these reasons, we decided to focus on the simpler 2D effective model. However, the results of the simulations based on the 2D BHZ model will be briefly addressed.

The BHZ model is characterized by the following features: Its advantage lies in the opportunity of taking into account a system with all present protagonists of quantum transport: the valence and conduction band as well as topological states in the bulk band gap. Further, the bulk 3D TI layer is squeezed into two dimensions as described in [114].

In the following, an example of the simulated band structure and conductance traces using the 2D BHZ Hamiltonian, as given in Appendix C.3, will be discussed. The calculations were performed by Michael Barth. The results, averaged over 200 disorder sets in the same way as was done for the effective model, are shown for $w_{\mathrm{QPC}} = 200$ nm in Fig. 5.14.

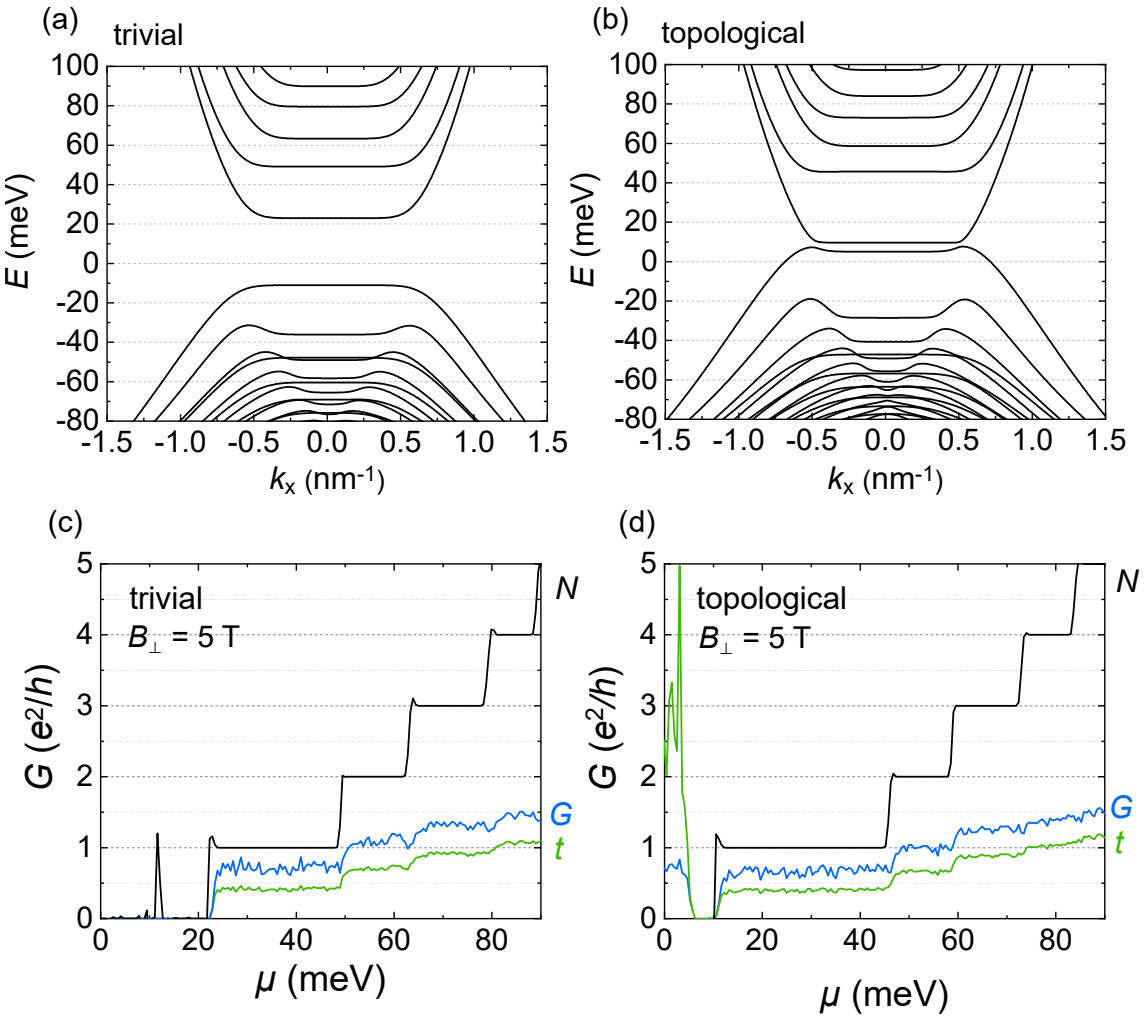

Fig. 5.14: (a) and (b): Band structures of a point contact as shown in Fig. 5.11 with a width of $w_{\mathrm{QPC}} = 200$ nm at $B_\perp = 5$ T for a (a) trivial ($M/b < 0$) and (b) topological ($M/b > 0$) choice of the parameter set, respectively. (c) and (d): Numerically computed conductance vs. chemical potential μ for (c) trivial and (d) topological choice of parameters at $B_\perp = 5$ T. The choice of colors is analogous to Fig. 5.13: The Hall conductance $G_{xy} = N$ is depicted in black, the longitudinal conductance at the QPC $G = G_{\mathrm{QPC}}$ in blue, and the diagonal conductance $G_d = t$ in green. Calculations performed by Michael Barth.

Here, we consider a HgTe sample in the trivial regime in (a), as well as in the topological regime [93] in (b), where we plot the different conductance components vs. the chemical potential. Here, we introduce the quantity M, which is the mass or gap parameter, describing the energy difference between the first electron-like level E_1 and first hole-like level H_1 at the Γ point (see Sec. 2.4.4) [93]. Further, we introduce b, which is an expansion parameter that depends on the heterostructure [93]. In the topological case, $M/b > 0$ applies, while in the trivial case, $M/b < 0$.

In analogy to Fig. 5.13, we show in Fig. 5.14 (c) and (d) the absolute value of the (transversal) Hall conductance $|G_{xy}| = |G_{14,35}|$ (black), the longitudinal conductance $G_{xx} = G_{14,23}$ (blue), and the diagonal conductance $G_d = G_{14,25}$ (green) for both cases, trivial and topological.

Comparing the simulation results of the 2D BHZ model to those of the 2D effective model, we observe the following: In general, the steps are better pronounced in the 2D effective model than in the BHZ model, in the sense that a clear transition from step 2 to 3, 3 to 4 and so on can be observed. Another striking difference is the fact that the first conductance step, which in the 2D effective model had the same length (with respect to V_g) as step 2, 3,..., is much longer in the BHZ simulation, i.e., it spans over a larger range of μ ($2-3$ times longer than the following steps). These observations may be related to the fact that in the BHZ-model-based simulations, a certain coupling between the conduction and valence bands is always given, whereas in the effective model, only the conduction band is considered. The scattering potential may then have a different effect on the modes. Further, the Landau levels in the BHZ model localize at higher energies, contrasting the effective model. Comparing the μ-scale in Fig. 5.13 to those in Fig. 5.14 (c) and (d), we observe that step 5 in N emerges at approximately 25 meV compared to 90 meV. This is related to the effective mass/Fermi velocity. It can be derived directly from the formula for Landau levels of parabolic bands.

Now, we will compare the results of the simulations based on the BHZ model, for the trivial set of parameters with ($M/b < 0$) in Fig. 5.14 (c) and the topological set with ($M/b > 0$) in Fig. 5.14 (d). At first glance, they resemble each other very strongly. Again, the length of the first step is very distinct, much longer in the topological regime than in the trivial one. This is evident from the band structures shown in (a) and (b). In the trivial case, the bandgap is much larger, and the spacing between first and second subband in the CB smaller than in the topological analog. Therefore, the first conductance step, situated in this region, is shorter. For the topological case, the opposite is the case. Besides that, both cases exhibit numerical artifacts in the Hall conductance. These were calculated by inverting numerical values. Thus, if the numerator is small and the denominator also contains small numbers, the calculation is no longer valid. However, these observations need to be put into perspective as the results strongly depend on the Hamiltonian parameters used.

All these points make the simpler 2D effective model appear in a better light.

However, the principal reason why we focused on the latter when developing a theoretical model, is that a topological treatment was not necessary here, as based on our experiment, we could not favor one model over the other.

5.5.4 The QPC as a separate part of the macroscopic system

The numerical simulations, presented in Sec. 5.5.2, show that steps with non-integer conductance values can be observed at a certain level of disorder, consistent with experimental data. However, despite the appeal of these calculations, the disorder amplitude remains merely an arbitrary fitting parameter. Since disorder in the junction appears to be the dominant factor, we adopted a modified Landauer-Büttiker-type toy model. In this model, we assume that the QPC input and output are relevant scattering centers, while the conductivity remains largely unaffected by scattering or dissipation outside these regions. In the Landauer-Büttiker model, additional scattering is represented by introducing two virtual 'contacts' near the QPC (contacts 7 and 8 in Fig. 5.15). The resulting LB matrix can be found in Appendix C.2.

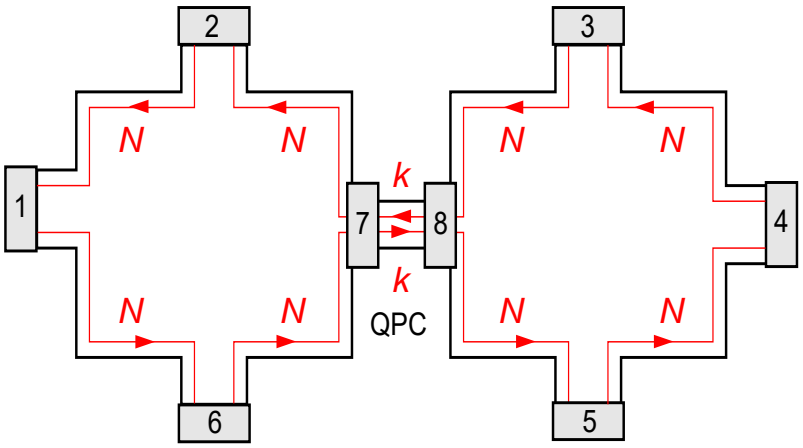

Fig. 5.15: Introduction of two additional thermalization points at the entrance and the exit of the QPC (contacts 7 and 8) in the Landauer-Büttiker model. N is the number of edge channels in the macroscopic device, while k denotes the number of modes inside the QPC.

Including these virtual contacts leads to several consequences. On the one hand, it enables the mixing of channels, which means that our previous assumption that the channels show no interaction, is not fulfilled anymore. On the other hand, thermalization becomes possible within the contacts, which means that the exchange of electrons, leading to a change in the chemical potential, brings all electrons come into equilibrium. It then bypasses the $N = t + r$ constraint from charge conservation. As a result, t and r are replaced by a single coefficient k, determining the number

of modes in the QPC, and thus its conductance, while charge conservation remains intact. The 4-terminal conductance obtained for the given device geometry is defined by the formula

$$G = \frac{N \cdot k}{N + k} \frac{e^2}{h}, \tag{5.13}$$

which we obtain from the 8-terminal LB formalism, in analogy to the 6-terminal LB formalism (see Appendix C.1), but including the virtual contacts 7 and 8. In addition to that, we introduce the transmission coefficient

$$t = \frac{N \cdot k}{N + 2k}. \tag{5.14}$$

In principle, k can take any value independent of N. However, when using a fixed value of k close to the value of the conductivity G of the QPC at zero magnetic field (see Fig. 5.3), the results obtained from this Landauer-Büttiker-type of model are in good agreement with the experiment. Now, we determine the values of k for the investigated devices. Fig. 5.16 (a) shows that all experimental data for group A lie between the two calculated curves obtained for $k = 1$ and $k = 2$. Similarly, in Fig. 5.16 (b), the data for group B falls within the calculated dependences for $k = 6$ and $k = 10$. These values correspond to the minimum and maximum conductivity, respectively, in units of e^2/h for all QPCs in each group.

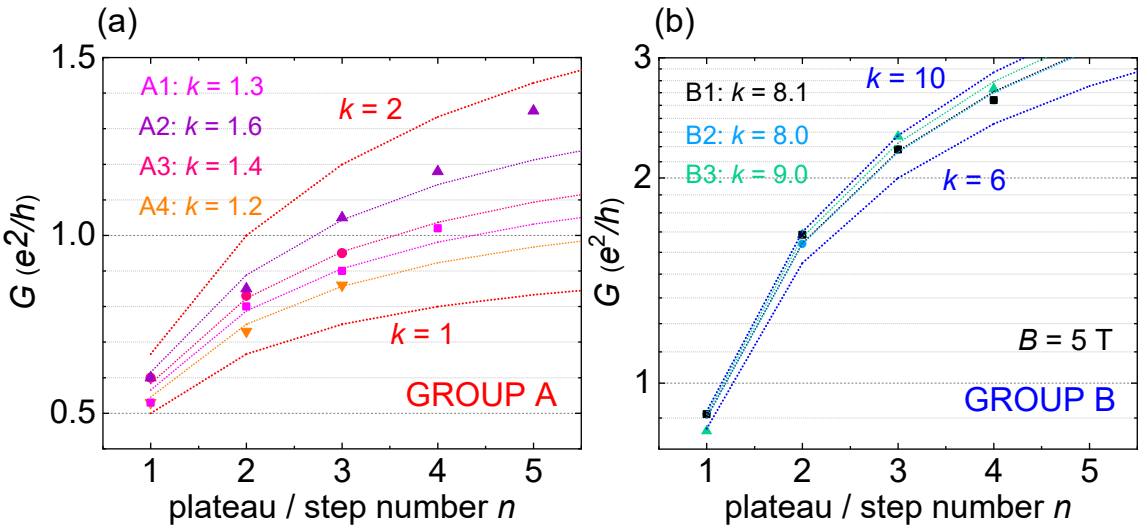

Fig. 5.16: Conductance step values (bold symbols) together with the individually fitted value of k (dotted lines) for each device of (a) group A, and (b) for group B, at $B_\perp = 5$ T. k was obtained from Eq. (5.13 with the conductance $G = \frac{N \cdot k}{N+k} \frac{e^2}{h}$. For the calculated conductance, we use $k = 1$ and $k = 2$ (for group A) and $k = 6$ and $k = 10$ (for group B). All experimental data fall between the calculated dependencies for each of the groups. The logarithmic scale in (b) was chosen in order to distinguish the devices from each other in a better way.

This finding suggests a complementary perspective: the system can be viewed as a series connection of two quantum Hall conductors with a magnetic field-independent resistor (i.e., the point contact) in between, the conductance of which is not quantized and is approximated by $k \cdot e^2/h$. In the Landauer-Büttiker model, the resistance R_{27} between contacts 2 and 7 at a plateau corresponds to the quantum Hall resistance $\frac{h}{e^2}\frac{1}{N}$, $R_{38} = 0$ (noting that R_{27} and R_{38} interchange when the magnetic field is reversed), and $R_{78} = \frac{h}{e^2}\frac{1}{k}$, representing the zero-field resistance of the QPC. Note that k can be non-integer.

When summing these resistances to obtain the total resistance across the point contact and converting it into a conductance, we obtain $G = \frac{N \cdot k}{N+k}\frac{e^2}{h}$, which matches Eq. (5.13). This perspective suggests that arbitrary plateau sequences can be generated as long as the resistance of the point contacts is (nearly) independent of the applied magnetic field. While this view overlooks the energy bands in the 3D topological insulator-based QPCs and the material's topological nature, it accurately captures the most prominent features.

Finally, we will compare the values obtained for $k(B_\perp = 5\ \mathrm{T})$ to the average conductance $G(B_\perp = 0)$, shown in Fig. 5.17. The values for k are obtained from measurement fits (shown in Fig. 5.16). Here, we recall the character and significance of k (see Eq. (5.13)), as a value that is equivalent to $G(B = 0)$, but obtained from measurements at $B_\perp = 5$ T, where steps appear and enable an extraction of the value k. It should be noted that k is not directly accessible for $B_\perp = 0$, as k cannot be extracted from any conductance steps, as they do not appear at $B = 0$. For both groups, $k(B_\perp = 5\ \mathrm{T})$ is in good agreement with the values of $G(B_\perp = 0)$, especially for group A, where $k = G\ [e^2/h] = 1 - 2$. This reproduces our findings from earlier in this chapter, where we discussed the grouping at $B_\perp = 0$ (see Fig. 5.3). For group B, this coincidence of values is not as strongly pronounced as for group A, but still, the values are very similar, with $k = 8 - 9$ and $G\ [e^2/h] = 4 - 10$. In total, we can conclude that k at strong magnetic fields equals the conductance at zero magnetic field in good agreement.

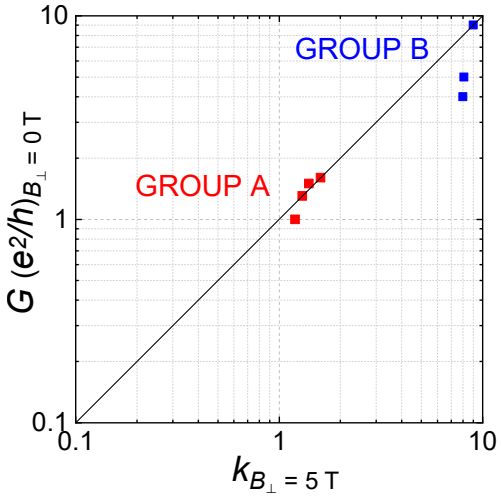

Fig. 5.17: Comparison of grouping at zero and strong magnetic field. The conductance G at $B_\perp = 0$ T and $V_g = 1$ V is plotted against the fitted values of k at $B_\perp = 5$ T, which corresponds to the number of transmitted modes (see Fig. 5.16). The diagonal line is supposed to indicated the condition where $G(B = 0) = k(B \neq 0)$. The devices follow this line in good agreement, which confirms our finding that k, the number of modes inside the QPC, equals the conductance in units of e^2/h at zero magnetic field. The logarithmic scale was chosen in analogy to Fig. 5.16.

5.6 Wide point contacts (group C)

The third group of devices, group C, will be analyzed in the following. We refer to the devices C3 - C6 of this group simply as point contacts instead of QPCs, as their width is not on the nanoscale anymore, but instead ranges between 1 and 10 µm. Devices C1 and C2 represent long wires ($l \approx 2$ µm) instead of the short point contacts, but will be considered as group C devices due to identical features appearing in the measured conductance. The width of devices C1 and C2 (with approximately $w = 600$ nm) can be roughly categorized as the limit between group B and C.

We focus on device C3 ($w = 1$ µm), which stands representatively for the devices of group C. A typical conductance trace at $B_\perp = 5$ T is shown in Fig. 5.18. Two effects are observed: an increase in the absolute value of the conductance in general, and a clear transition from step-like to oscillation-like curves with huge peaks, which was still rudimentary, but initiated in group B (see Fig. 5.5). Only small residues of conductance steps are recognizable, while oscillations clearly prevail with maxima reaching conductance values of several 10 e^2/h. However, fully pronounced oscillations with minima down to zero measured signal do not develop, as would be the case for macroscopic systems when the QHE is measured. Instead, the minima continue to grow with each further step of the sequence in form of what we refer to as residual steps.

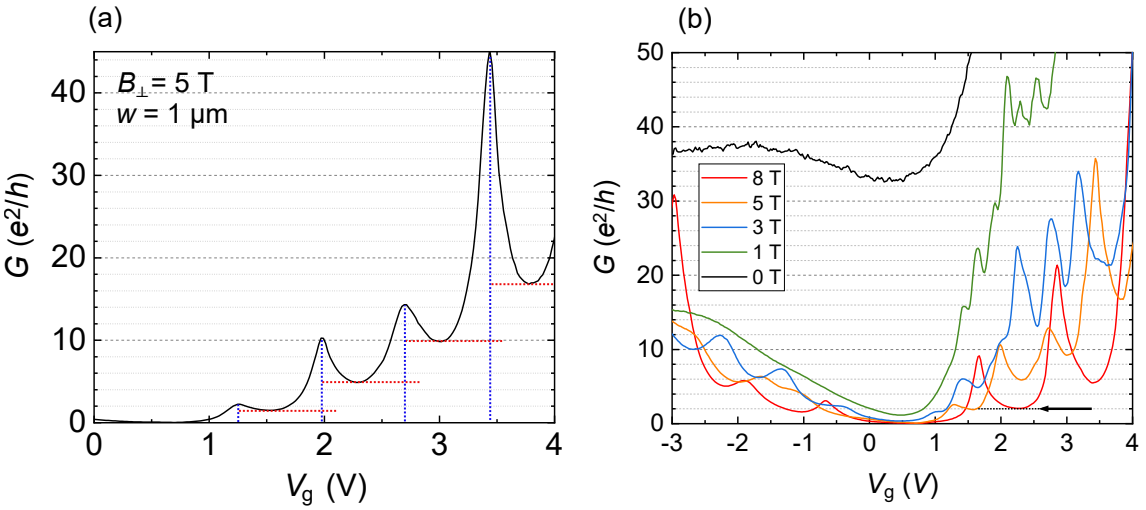

Fig. 5.18: (a) Conductance G of device C3 as a function of V_g with $w = 1$ µm at $B_\perp = 5$ T and $T = 1.5$ K. At this width, an oscillation-like mixture of peaks and steps can be distinguished instead of pure steps. We refer to these as residual steps, indicated by red lines, and the peaks, highlighted by blue lines. (b) Conductance G for selected magnetic fields between $B_\perp = 0$ and 8 T for device C3. At $B_\perp = 0$, the conductance is very high ($\approx 40\ e^2/h$), but at high magnetic fields ($B_\perp =\geq 5$ T), it drops to a minimum/step of approximately 2 e^2/h (highlighted by an arrow).

Now, we analyze the situation for different magnetic field strengths. In Fig. 5.18 (b), conductance traces are depicted for $B_\perp = 0 - 8$ T for device C3. In the absence of a magnetic field, no signs of quantization are visible. Instead, very high values of the conductance appear ($\approx 40\ e^2/h$). At strong magnetic fields of $B_\perp \geq 5$ T, the conductance shows a stable (residual) step at $G \approx 2\ e^2/h$ (highlighted by an arrow in Fig. 5.18 (b)), which remains consistent over a wide range of magnetic fields up to the maximum applied value of 8 T, similar to the observations discussed in Fig. 5.1 for device A1.

As there are two key features characterizing the conductance behavior of group C - the steps and the oscillations - the question of how to correctly classify the devices from group C arises, when referring to the step positions. This can either be done with respect to the peak maxima, or the minima. Previously, in Fig. 5.7 discussed in Sec. 5.3, we have classified the devices of group C by the values of the minima, which correspond better to the steps as seen for groups A and B, and shows more clearly the QPC-like character of the wide point contacts than the peak maxima, which we interpret as a feature of macroscopic devices. Depending on which aspect we want to concentrate on in the interpretation, we can analyze the (residual) steps - when studying the QPC-like character - or, we can analyze the peaks - if studying the macroscopic characteristics of the point contacts.

In Fig. 5.19, the values of the maxima of the oscillations (full symbols) and

the minima (empty symbols), i.e., the residual steps, are shown. For more clarity, the devices are split into two graphs, showing the relatively narrow, but long wires (devices C1 and C2) in (a), and the point contacts C3 - C6 ($w = 1 - 10$ µm) in (b), both at $B_\perp = 5$ T. The general trend of the step sequence (i.e., the dependence on the step number n) is a growth of both characteristic features - maxima and minima. In some cases, the maxima and minima values of a device coincide, which means that only a step (without a peak) is formed. It appears that the residual steps show a more monotonous behavior than the peaks, which is evident from the almost linear growth if we look only at the values of the minima.

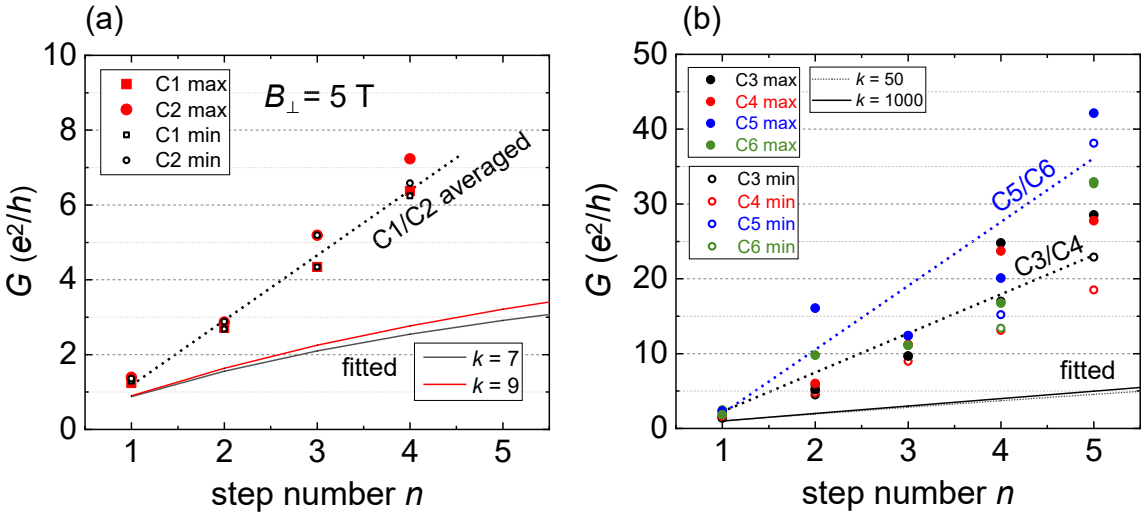

Fig. 5.19: Conductance of devices from group C at $B_\perp = 5$ T in dependence of the step number. Symbols denote the measured local maxima (bold) and minima (empty) of each oscillation. (a) Devices C1-C2 with $w \approx 600$ nm are shown. (b) Devices C3-C6 with w between 1 and 10 µm are shown. It is possible to classify group C devices by both - maxima and minima of the oscillations/steps. In some cases, the maxima and minima of a device coincide, which means that only a step (without a peak) is formed. A general trend for each sample, averaged over both, maxima and minima, estimated by eye, is indicated by dotted lines. A grouping within group C, i.e., of the devices with entirely identical fabrication parameters is observed. The device pairs C1/C2, C3/C4 and C5/C6 exhibit nearly identical traces despite having different widths. This points to a subordinate role of the dimensions, in favor of an individual disorder for each sample. Further, the graphs show the limits of the use of the coefficient k, previously used for fitting the experimentally measured values for groups A and B at strong $B_\perp$: In both graphs, the expected value of k is included, derived from G at $B_\perp = 0$. However, the fitting with the parameter k does not apply for the devices of group C. The fitted values of k are too low. Even a fitting with the very large value $k = 1000$ (included in (b)) does not reproduce the number of modes inside the devices anymore.

However, we further observe that, although the devices cover a wide range within one order of magnitude in their width and cross section, their conductance does not increase in linear proportionality with respect to their geometrical parameters, as one might expect for larger-scale devices. The lack of a simple correlation between conductance and width becomes particularly evident when comparing devices from the same sample to those from other samples fabricated in different cycles, i.e., sample s83 (devices C1/C2), sample e32 (devices C3/C4), and sample j4 (devices C5/C6). All three samples of group C were each fabricated in an individual fabrication cycle. A set of measured curves for devices C3, C4, C5 and C6 is depicted in Fig. 5.20. At first glance, the traces show a loose grouping. However, at second glance, the conductance behavior is better characterized by a pairwise grouping of the traces from devices C3/C4 and C5/C6.

Adding Fig. 5.19 into our considerations, if we compare an averaged conductance trend (one average value for both, maxima and minima, indicated by dotted lines) for the ensemble of the two devices of each sample (chip), the conductance of devices made on the same chip does not scale with the width, but rather shows a grouping among identically fabricated devices of the same sample. In particular, this can be seen in Fig. 5.19 (a), for instance, at the first two steps. These show almost identical values for the devices C1 and C2, although they differ in width by a factor of two.

The observations made in both figures point to a strong influence of disorder, which impacts the governance of the number of transmitted modes together with the size. This behavior is in accordance with groups A and B, where an essential finding was that the amount of conductance (or transmitted modes) is not only defined by the dimensions of the constrictions. Instead, we hypothesize that also in the case of group C, disorder dominates the conductance behavior. Presumably, also for this group of devices, it originates at the boundaries of the point contacts, i.e., their respective entrance and exit.

Drawing any quantitative conclusion is speculative. However, what can be deduced with certainty from the traces presented in Figs. 5.19 and 5.20, is that the strong influence of disorder does not only apply to groups A and B, but also to group C. For groups A and B, we concluded that the disorder might stem from the lithographic etching processing, giving rise to additional scattering centers. This hypothesis is now reinforced in group C by the fact that, formally, the fabrication process may be identical for all samples, but in real systems, every fabrication cycle creates an individual disorder profile.

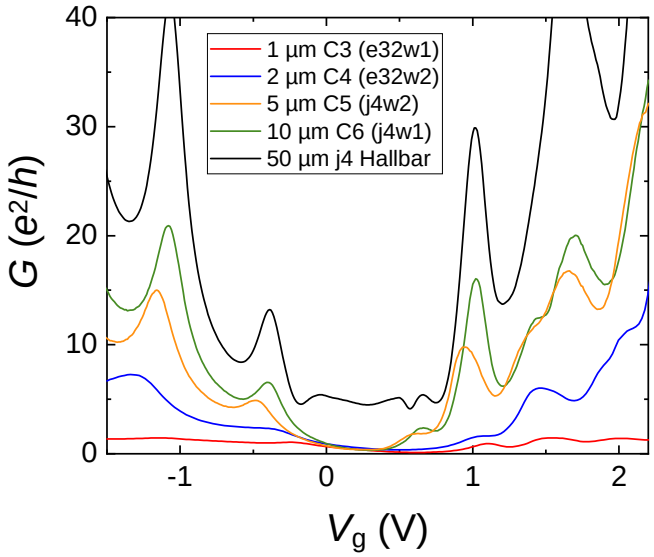

Fig. 5.20: Conductance G for wide point contacts with widths between $w = 1$ and 10 µm, and the macroscopic Hall bar with $w = 50$ µm, at $B_\perp = 3$ T, $T = 1.5$ K. At this magnetic field strength, the conductance of the Hall bar does not reach (almost) zero, as we operate in an intermediate state between classical and quantum transport (see discussion referring to Fig. 4.7). The conductivity peaks, clearly pronounced for the macroscopic device, are obtained also for all devices shown. At $V_g = 1$ V, it is clearly visible especially for the large constrictions with $w = 5$ and 10 µm. However, also for 1 µm, a small peak appears. The trace of the narrowest device with 1 µm resembles most the step-like conductance sequence known from groups A and B. Hence, a transition into a macroscopic 2D system can be observed. It scales with the constriction size, but also the scattering potential in the vicinity of the QPC shows an impact, as the increase in peaks/steps is not fully proportional to the size, but especially devices fabricated in the same series show more similar traces. This hints at a strong impact of the individual scattering mechanism, most probably obtained from the lithographic etching.

To draw a conclusion on the transition towards fully macroscopic systems, we consult Fig. 5.20. The gradual transition to macroscopic behavior becomes particularly evident if we compare the entire range of measured widths (between $w = 1$ and 10 µm) to a measurement of the longitudinal resistance of the macroscopic device ($w = 50$ µm). The latter shows typical SdH-like oscillations, and does not reach zero or almost zero conductance in the band gap, which the point contacts (almost) do, even at width $w = 10$ µm (at around $V_g = 0.3$ V). This can be explained by the fact that at $B_\perp = 3$ T, we are located in an intermediate regime between classical transport (where we expect a non-zero conductance according to Fig. 4.1 (a)) and

quantum transport (where, at high magnetic fields, almost zero conductance can be expected). In this range of magnetic fields, full quantization may not be given yet. As some filling factors are more developed than others, the system can be partially quantized. In the present case, apparently, the gap associated with a filling factor equal to 0 is not fully opened [60]. Another, more intuitive explanation, is that for a macroscopic device, we expect higher conductance than for the smaller point contacts. In summary, it becomes evident that the devices transition into a macroscopic 2D system with a constriction, the larger the width of the constriction is. This trend is manifested in both features of group C, the conductance maxima and the minima.

Finally, returning to Fig. 5.19, we discuss the validity of the coefficient k for group C. As the conductance at $B = 0$ is very large in this group, at around 50 e^2/h (here, we use an averaged value for all group C devices), we assume that $k = 50$. With this, we verify the formula obtained for G, given in Eq. (5.13), by fitting it to the experimental data for the steps shown in Fig. 5.19. For all devices studied, it is too low. Intuitively increasing the value of k does not have the desired effect, as the fit for $k = 1000$ (shown in Fig. 5.19 (b)) clearly indicates by falling significantly below the range of the measured values. Here, it becomes obvious that k does not reproduce G anymore. This becomes the case as soon as G becomes larger than $1e^2/h$ for the first conductance step, which applies to all group C devices. The more we approach macroscopic systems, the less k is an applicable parameter for the description of the conductance, or transport in general. At this point, the limit of k becomes evident This is, however, what one would expect, as k originates in a LB-based description of a multi-terminal system with a 1D constriction. The devices of group C, however, cannot be treated as such anymore, as they do not pertain to 1D devices, and a characterization of the conductivity by means of k becomes impossible.

5.7 Summary

To conclude this chapter, we have observed that none of the investigated quantum point contacts has shown conductance quantization in zero magnetic field. However, when subjected to a magnetic field, they exhibited quasi-quantization of the conductance at non-integer values. These anomalous conductance values persisted over a wide range of parameters, i.e., the magnetic field, gate voltage, and temperature, which implies an underlying preferred scattering mechanism within the QPCs. We categorize the devices into three groups (A, B and C), defined by the values of the preferred conductance step sequences, starting at values of 0.6 e^2/h for group A, and 0.85 e^2/h for group B for the first conductance step, respectively. When developing a theoretical model describing the transmission behavior, we focused on devices from groups A and B, which showed two stable conductance step sequences, and can be regarded as true QPCs, in contrast to group C. In this group, the geometry is formed

by larger constrictions of typically several µm of width, which no longer allows us to classify these devices as QPCs, which are characterized by a width in the order of only a few 100 nm.

The occurrence of steps in group A and B can be reproduced by numerical tight-binding calculations using the Python package Kwant. The calculations, performed by Michael Barth, are based on an effective model describing a 2D conduction band while neglecting the valence band. The results suggest that disorder in the point contact plays the leading role in the atypical quantization sequences. It was refrained from the use of a TI-specific, but too complex 3D model. Instead, calculations based on the 2D Bernevig-Hughes-Zhang model [93] were performed for comparison to the simplified effective model, with similar results. As the experiment did not show any signs of topological behavior, we concentrate our study on the 2D effective model. Modeling the disorder phenomenologically using a Landauer-Büttiker model, we find that the conductance steps can be described by Eq. (5.13), where N is the number of edge modes, corresponding to the filling factor, in the wide regions outside the QPC, and k represents the number of modes inside the QPC, which is equal to the conductance in units of e^2/h at zero magnetic field. In this model, the QPC acts as a selective filter that partially transmits the QHE edge states. The constancy of the transmission coefficient of this filter is a striking and unusual result, particularly for one-dimensional systems. A possible explanation of the lack of quantization is the non-adiabaticity of QPC boundaries, a consequence of their fabrication using wet-chemical etching.

In the last part of this chapter, we discussed the behavior of the conductance for wide point contacts from group C. Throughout the devices, the conductance was much larger than for groups A and B. In addition to that, the conductance of these point contacts exhibited features rather reminiscent of macroscopic devices, i.e., peaks, or SdH-type oscillations, in the resistivity in addition to sublinearly growing minima in the conductance, which we identified as residues of conductance steps. Further, the major influence of a probably fabrication-induced disorder, observed also for groups A and B devices, manifests itself in a grouping of equally fabricated devices within group C. In summary, the devices from group C mark a transition to a macroscopic 2D system with a constriction.

6. Conductance of QPCs in tilted magnetic fields

6.1 Motivation

In the previous chapter, the effect of a magnetic field directed into perpendicular direction to the sample plane on the conductance of a QPC was studied. It was shown that the quantization of the QPC conductance correlates with the formation of the quantum Hall effect in the regions adjacent to the QPC with a two-dimensional electron-hole gas. In a sense, the conductance of the QPC reflects the reaction of the two-dimensional electron-hole gas on a quantizing magnetic field. It is interesting to investigate whether this pattern will be preserved under conditions of an inclined magnetic field, i.e., having both an out-of-plane and an in-plane component of the magnetic field. In macroscopic two-dimensional systems, the influence of a magnetic field can be broadly categorized into, first, orbital effects, which pertain to the motion of electrons along cyclotron orbits and are therefore determined solely by the perpendicular component of the magnetic field, and, second, spin effects, which reflect the impact of the total magnetic field on spin polarization through the Zeeman effect and modifications originating from spin-orbital interaction. Other possible effects, such as those associated with the redistribution of the wave function within the quantum well by the magnetic field, have a lesser impact and are thus not considered. In classical two-dimensional systems, such as GaAs or Si quantum wells and heterostructures, Zeeman splitting is significantly smaller than the cyclotron energy. As a result, even a strong parallel magnetic field has a limited effect on conductivity. In contrast, HgTe is characterized by a strong spin-orbit interaction and a large g^*-factor, making the study of the behavior of QPCs based on HgTe particularly interesting. Additional contributions may come from topological electrons on the side surfaces of HgTe, for whom the parallel magnetic field is effectively perpendicular, potentially leading to unique transport behaviors.

6.2 Description of observations: The parity effect

We study the evolution of conductance steps in dependence of an inclined magnetic field and the gate voltage, at constant perpendicular magnetic field $B_\perp$ and increasing in-plane magnetic field $B_\parallel$. The experiment is conducted in a way that the tilt angle θ between the applied magnetic field and the surface normal of the devices is varied from 0° to almost 90° with respect to the wire axis, depending on the total amount of applied magnetic field and limited by the technically applicable magnetic field of the cryostat. The total magnetic field is given by

$$B_{\text{total}} = \frac{B_\perp}{\cos\theta}. \tag{6.1}$$

In the case of $B_\perp = 5$ T, as shown in Fig. 6.1, the maximum technically possible tilt angle is 67.5°, which corresponds to a total magnetic field of $B_{\text{total}} \approx 13$ T. Conductance traces at inclined magnetic fields in dependence of the gate voltage are shown for device A1 in Fig. 6.1 (a) and (b), and for device B1 in Fig. 6.1 (c) and (d), respectively. In general, devices A1 and B1 show qualitatively the same behavior. However, as these stand representatively for the two groups of devices, A and B, and because some features are more pronounced for sample B1, both of them are shown. As mentioned previously in Chapter 5, the $G(V_g)$ dependence exhibits an asymmetry between electrons and holes: on the electron side, well-defined steps are observed, whereas on the hole side, the steps appear distorted and resemble Shubnikov–de Haas oscillations. This behavior is attributed to the difference in effective mass, as electrons are nearly an order of magnitude lighter (for calculations see Ref. [64], estimated numbers for the system under study will be discussed later in Tab. 6.1). From this, it follows that the spacing between Landau levels is larger on the electron side, and consequently, the more pronounced QHE within this region.

However, this is not the only difference between the electron and hole side. Let us compare the dependences $G(V_g)$ obtained for different tilt angles. Since the perpendicular component of the magnetic field $B_\perp$ remains unchanged, these dependencies can also be interpreted as dependences on the parallel component of the magnetic field $B_\parallel$. As the tilt angle increases (i.e., $B_\parallel$ increases), in the conduction band (i.e., for $V_g \geq 1$ V), the position and shape of the steps remain largely unaffected. In contrast, in the valence band, the shape of the steps is sensitive to the tilt angle, and an unintuitive observation is made. As the tilt angle increases, the shape of steps with odd numbers smooths out (and steps even disappear at large θ), while steps with even numbers, on the contrary, besides not disappearing, become even more pronounced. If the tilt angle is further increased, the disappeared steps are restored. The behavior of each step in the valence band is determined by its parity. This section is devoted to analyzing this parity effect.

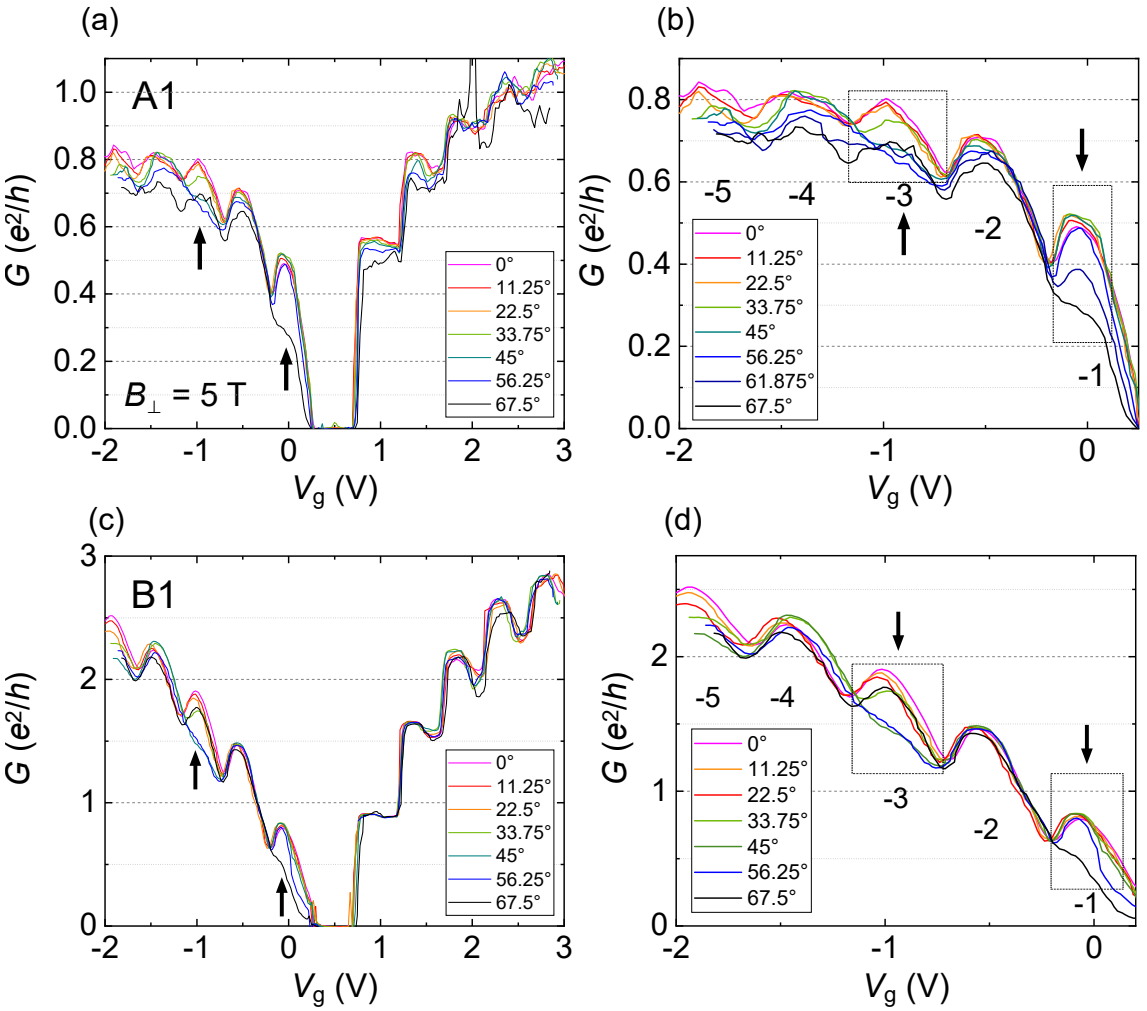

Fig. 6.1: Conductance G for the QPC from device A1 and B1 as a function of V_g for constant $B_\perp = 5$ T for different tilt angles from $\theta = 0°$ (for out of plane) to 67.5°. Filling factors ν are assigned by numbers, which are determined from ρ_{xy} in the unpatterned region 2 in Fig. 4.7. (a) G for entire measured V_g-range (device A1). The black arrows highlight missing steps for increased tilt angles ($\theta = 45°$ and 56.25°), giving rise to a parity effect, especially in the valence band (VB). At larger tilt angle $\theta = 67.5°$, the step re-appears. Also the conduction band (CB) shows changes, visible for very large tilt angles, in this case esp. at $\theta = 67.5°$ (black trace). Here, the measured G is decreased. (b) Zoom into the VB of device A1. The parity effect is better visible: odd-numbered steps disappear and only the even-numbered steps remain. The arrows from (a) highlight the first and third missing steps in rectangular boxes. Every second conductance step is skipped, so that only $\nu = -2$ and $\nu = -4$ show clear step maxima. For $\nu < -4$, the behavior is less pronounced due to lower signal-to-noise ratio (low resistance measured) and low sensitivity. (c) Entire measured V_g-range (device B1). The parity effect is clearly recognizable also for this device in first place in the VB. In the CB in particular, device B1 shows a more pronounced change in conductance steps in comparison to device A1, evident at $\nu = -3$ and $\nu = -4$. (d) Zoom into the VB of device B1. Again, the parity effect is clearly visible: odd-numbered steps disappear at $\theta = 45°$ and only the even-numbered steps remain, until re-appearing again at larger tilt angle ($\theta = 67.5°$).

Since the behavior of $G(V_g)$ steps is largely determined by the properties of the macroscopic adjacent regions with two-dimensional electrons and holes, the analysis of the parity effect should begin with the peculiarities of the formation of Landau levels of two-dimensional carriers and their manifestations in the (macroscopic) conductivity σ_{xx}. In the following, we recall the various regions within a Landau fan chart, discussed previously in Chapter 4.4. Here, we address these regions with respect to the effect of a tilted magnetic field. The regions are illustrated in Fig. 6.2, highlighting the parameter region which covers the measurement region shown in Fig. 6.1 in orange.

For $B_\perp > 3$ T (region 1), all charge carriers begin to form a hybridized QHE state with the filling factors determined only by the total charge density in the system $(n_s - p_s)$. A tilted magnetic field might not show any obvious effect, because every SdH oscillation minimum is fully developed. Therefore, we are interested in smaller B fields, because oscillations in the conductivity are necessary for our analysis. It is much easier to observe an effect, if we have an inequality in the SdH oscillation (discussed later in more detail in Fig. 6.8).

In region 4, E_F lies in the energy gap so that only topological states on the top and bottom surfaces are present at the Fermi level, but no bulk states. We do not expect any effect of $B_\parallel$, because the conductivity decreases to almost zero. At very small magnetic fields, i.e., in region 6, the Landau level separation is smaller than the Landau level broadening and transport is fully diffusive.

For $B_\perp < 3$ T, several groups of carriers partially contribute to transport. In regions 3 and 5, the Landau fan pattern is quite complicated and makes it difficult to draw any conclusion for our system. Here, several groups of carriers yield a contribution. The conduction band (region 5) hosts several charge carrier types, i.e., bulk and (top and bottom) surface electrons. Thus, the surface states coexist with bulk electrons that are filled if $E_F > E_C$.

In regions 2 and 3 in the valence band, bulk holes dominate the Landau spectrum, but coexist with surface electrons. The coexisting surface electron and bulk hole Landau fans cause a complex checkerboard pattern in region 3. Within this region, both types of charge carriers are present, each characterized by its own set of Landau levels. However, only the top surface electrons participate in the formation of the observed oscillations. The bottom electrons have a fixed and small density (experimentally indistinguishable from zero), contributing to transport. We will hence continue by considering only bulk holes and top-surface electrons.

Meanwhile, in region 2, the number of electrons is so small that they are completely placed at one Landau level and they do not influence the observed oscillation pattern further. The pattern is therefore fully determined by bulk holes. Therefore, only region 2 in the valence band can be considered for our evaluation, yielding the simplest case with least charge carrier types.

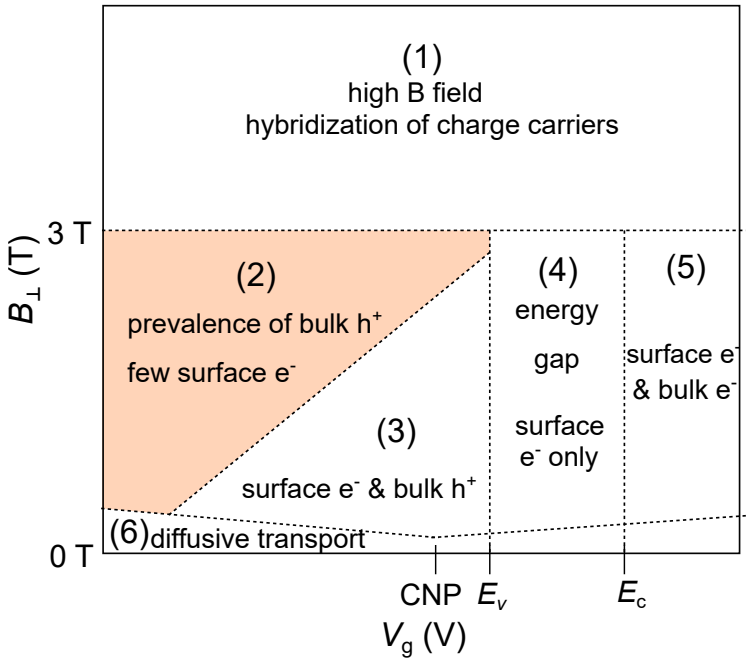

Fig. 6.2: Schematic of the areas in a Landau fan chart of a 3D TI HgTe-based system, as investigated in Ref. [114]. We choose region 2 (highlighted in orange color) for our evaluation because of the best chances for a correct assignment of the charge carrier types. We exclude the following regions from our considerations: Region 1, because $B_\parallel$ (minor compared to $B_\perp$) might not show any obvious effect, as every SdH oscillation minimum is fully developed then, i.e., the σ_{xx} minima are too deep. Therefore, we are interested in smaller B fields, because oscillations in the conductivity are necessary for our analysis. However, the findings can be transferred to the measurements taken at $B_\perp = 5$ T, as we refer to the corresponding Landau levels, which are identical. In region 3 and 5, surface and bulk charge carriers are present to similar extent, leading to a complicated pattern of the Landau fan chart in these regions. Within region 4, which is in the band gap, conductivity is given only by surface carriers. Region 6 is fully diffusive and cannot be considered. Hence, only region 2 remains, with surface electrons and bulk holes as possible charge carriers, but with the latter clearly prevailing. For the corresponding macroscopic Landau fan chart, see Fig. 4.7.

Together with our considerations made in Sec. 4.4, we can estimate the response to the parallel component of the magnetic field, and which is key to explain the parity effect. As mentioned earlier in this section, the conduction band shows a slight dependence on the inclined magnetic field, especially visible for device B1 in Fig. 6.1 (c). Except for this point, device B1 shows the same behavior as A1. However, the VB shows the parity effect in a by far more pronounced way, compared to the CB. Therefore, we will attempt to find an explanation of the effect in first place for the VB.

As we know from the previous chapter, the properties of charge carriers located in macroscopic adjacent regions significantly govern the behavior of the point contact. For a comparison with the macroscopic device, we consider quantum Hall measurements in the valence band of the latter in Fig. 6.3. For $B_\perp = 3$ T, Hall conductance traces are shown for different tilt angles. (We use $B_\perp = 3$ T instead of 5 T to show with more clarity the desired effect, as the plateaus were better pronounced in this measurement. However, the result obtained is fully applied to the conductances measured at the QPCs at $B_\perp = 5$ T.) It is demonstrated that the response of the ρ_{xy}-plateau shape to the parallel component of the magnetic field qualitatively repeats the same dependence for the conductance steps appearing at the QPCs. The width of the Hall plateaus changes with growing tilt angle, which is highlighted by colored boxes of trapezoidal shape: green for plateaus which become more pronounced and broader (even ν), gray for plateaus which become narrower or even disappear at large enough tilt angle θ (odd ν). The inclined magnetic field hence leads to a reduction, or even extinction, of the odd plateaus with increasing $B_\parallel$. Accordingly, the absence of every second step in the conductance of the point contacts can be traced back to the macroscopic device, which behaves analogously to the point contacts. In the following, we will analyze the observed parity effect in the conductance steps by taking into account theoretical considerations.

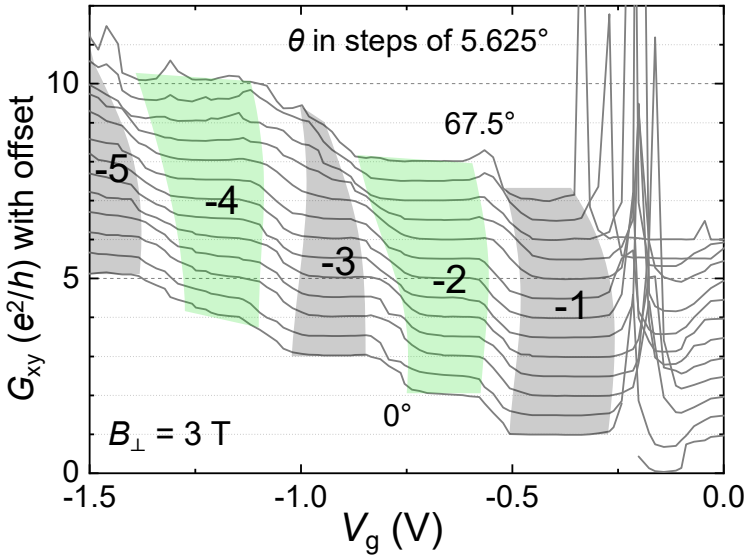

Fig. 6.3: Waterfall plot of the Hall conductance G_{xy} of the macroscopic part of sample e23 (where devices A1 and B1 stem from), shown for the valence band for $B_\perp = 3$ T. The width of the plateaus changes in dependence of the tilt angle θ, which is highlighted by either gray- (decreasing plateau width with growing θ) or green-colored boxes (increasing plateau width with growing θ). The assigned filling factors are denoted in each plateau region. The growth or reduction of the width of the Hall plateau governs the conductance behavior of the mesoscopic device, as the macroscopic device shows analogous behavior compared to the QPC devices. For measurements exceeding $B_\perp > 3$ T, the behavior is qualitatively equal. Due to its highest measurement quality, the graph for $B_\perp = 3$ T was selected representatively instead of $B_\perp = 5$ T.

Further, we model the behavior of Landau levels in tilted magnetic fields in two characteristic cases: for a case of weak Zeeman splitting ΔZ (see Eq. (2.49)), representing GaAs electrons with $\Delta Z_0/\hbar\omega_c = 0.012$ (with ΔZ_0 denoting the Zeeman splitting at $\theta = 0°$), serving as a comparison to conventional 2DEG systems, and strong splitting with $\Delta Z_0/\hbar\omega_c = 0.6$, representing HgTe bulk holes. We use the value of the spin splitting to cyclotron energy ratio of 0.6, based on the estimations in Ref. [114]. However, later in this chapter, we will show that a value around 1.5 is needed, i.e., where the Zeeman splitting exceeds the cyclotron energy, which is quite unusual, in order to describe the observed experimental data and match other experimental works [75, 82]. However, for the sake of clarity, we model the case of $\Delta Z_0/\hbar\omega_c = 0.6$ first. The obtained results are normalized to $\hbar\omega_c$ (in order to exclude the influence of the effective mass on the result) and shown in Fig. 6.4.

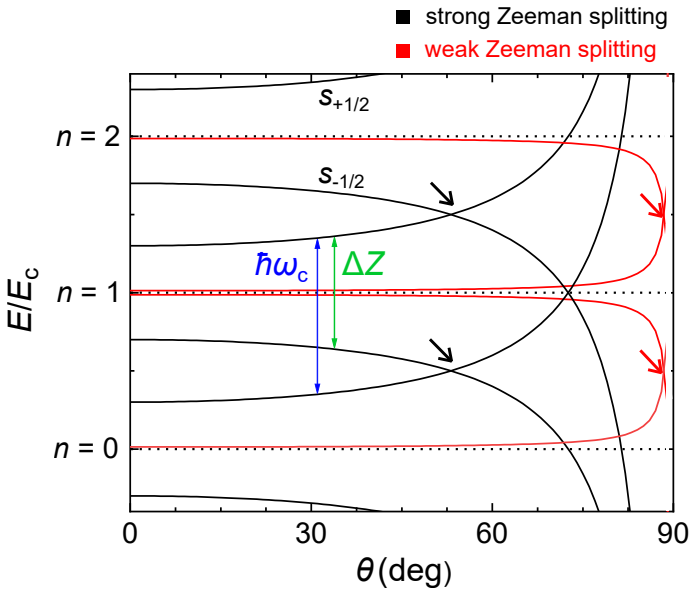

Fig. 6.4: Model dependence of the position of Landau levels at a fixed value of $B_\perp = 5$ T as a function of the tilt angle θ. The Landau levels were calculated using the equation $E = E_c \pm \frac{1}{2}\Delta Z = n\hbar\omega_c \pm \frac{1}{2}g\mu_B B_{\text{total}}$, which is a slight modification of Eq. (2.50). For simplicity, the shift of $+1/2$ in the term $(n + \frac{1}{2})\hbar\omega_c$ of the latter equation was neglected. The energy E was then normalized to $\hbar\omega_c$. The calculations are done for two model situations: weak Zeeman splitting (red curves, $\Delta Z_0 = 0.012\ \hbar\omega_c$, with ΔZ_0 denoting the Zeeman splitting at $\theta = 0°$), corresponding to electrons in GaAs, and strong Zeeman splitting (black curves, $\Delta Z_0 = 0.6\ \hbar\omega_c$), which may correspond to bulk holes in HgTe quantum wells. In the present example, for GaAs, $E_c = 8.6$ meV and $\Delta Z_0 = 0.11$ meV was used, and for HgTe, $E_c = 3.8$ meV and $\Delta Z_0 = 5.7$ meV, correspondingly (see also Tab. 6.2 later). Due to the difference in the ratio $\Delta Z_0/\hbar\omega_c$, oscillations with even filling factors will be more pronounced in $B_\perp$ for GaAs. On the contrary, the odd factors will be more pronounced for HgTe (For a detailed explanation of the oscillation behavior, see Fig. 6.8 discussed later). As the tilt angle increases, the spin up and spin down states of neighboring Landau levels n converge and inevitably cross, marked by the arrows (black for HgTe and red for GaAs). At this point, the energy gap collapses and the corresponding SdH oscillation disappears.

The first difference between the case of weak and strong Zeeman splitting is observed already at $\theta = 0°$: for the case of 2DEG GaAs (and any other system with a small ΔZ value, e.g., Si), oscillations with even filling factors are more pronounced because of the larger energy gaps in comparison to Zeeman gaps. In a weak magnetic field, according to Fig. 6.7 (a), which will be discussed later, the Zeeman splitting becomes so weak that oscillations with odd filling factors may completely disappear. On the contrary, in the model case with strong Zeeman splitting, the condition

$\Delta Z > \hbar\omega_c - \Delta Z$ is fulfilled, so that the situation is reversed and oscillations with odd filling factors become more pronounced than those with even ones.

As the tilt angle θ increases (and, accordingly, the $B_\parallel$-component), the magnitude of the spin splitting ΔZ increases proportionally to $1/\cos\theta$. Thus, the distance between the Landau levels with neighboring numbers n and different spin directions becomes smaller and inevitably crosses at the angle marked by the arrows in Fig. 6.4. Here, the second difference between the systems appears: in the case of HgTe, the crossing occurs at a much smaller angle (about 45°) than in GaAs, where the crossing occurs close to 90°. The crossing of the Landau levels is accompanied by the collapse of the energy gap and the disappearance of the oscillation with the corresponding filling factor (even, according to Fig. 6.4). At a further increase of the tilt angle (not available in our experiment due to the limited strength of B_{total}), a reverse opening of the gaps and a restored occurrence of oscillations should take place. This can be seen in the black trace ($\theta = 67.5°$) in Fig. 6.1 (b) for device A1 and (d) for device B1 at filling factor $\nu = -3$, respectively. The method based on the study of the amplitude of SdH oscillations in a tilted magnetic field is widely used to determine the value of the g^*-factor [75, 82, 124, 125].

6.3 The effect of a tilted magnetic field on 2D electron and hole systems

In this section, we will introduce theoretical considerations related to effects measured in parallel magnetic fields, which are too specific for Chapter 2. We start with the pure perpendicular magnetic field, and continue by adding an in-plane magnetic field component, discussing its impact on the HgTe material system in particular. Following this overview, we will analyze the experimental data based on the discussion of Fig. 6.4 and the knowledge presented in this section about the impact of a tilted magnetic field in Sec. 6.4.

6.3.1 2DEG in a quantizing perpendicular magnetic field

As discussed above, in the regime of high magnetic fields, the system is fully quantized, so that all Landau levels are resolved and the QHE is observed. Here, the total density $n_s - p_s$, which corresponds to the total amount of mobile charges in our system, determines the filling factors and the Landau level positions. At magnetic fields exceeding $B > 3$ T, states begin to hybridize. The density of electrons is $0.7 \cdot 10^{11}$ cm^{-2} at the beginning of the VB. If the charge carrier density was larger, the electrons could contribute to the Landau levels in the VB. However, in the present case of $B \geq 3$ T, only bulk holes contribute to transport. The change of the distance between Landau levels can be seen in the conductivity, as discussed in the previous section. Minima in the conductivity shift to higher or lower values, depending on

whether it is a cyclotron or a Zeeman gap. We keep in mind that the QHE is very pronounced, if at a large magnetic field, the Landau level separation $\hbar\omega_c$ is large compared to the Landau level broadening, i.e., if $\omega_c\tau_q \gg 1$.

6.3.2 The effect of pure parallel magnetic field to the 2D electron and hole system

The behavior of a classical 2DEG in a parallel magnetic field is largely determined by the Zeeman effect, which can also be modified by spin-orbital effects. Classical 2DEGs are often used in weak magnetic field experiments, where orbital effects prevail over spin effects due to their low g^*-factor and spin-orbit interaction (SOI). Hence, these systems provide a clean platform for exploring magnetotransport in regimes where spin interactions play a subordinate role. An example of a classical 2DEG system with a small g^*-factor and weak SOI is the GaAs/AlGaAs heterostructure. GaAs has a bulk electron g^*-factor of $g^* = -0.44$, which is significantly lower compared to other semiconductors like InAs ($g^* \approx -15$) or materials with stronger SOI such as HgTe, whose g^*-factor can be two orders higher and has to be estimated for each system depending on the exact design of the QW used (see Tab. 6.1) [45].

The SOI valid for electrons in GaAs/AlGaAs heterostructures is generally weaker compared to materials like InAs or InSb due to weaker coupling between the conduction and valence bands, and weaker structural inversion asymmetry (SIA) at the interface [126]. Since the Lorentz force requires a component of the magnetic field perpendicular to the 2DEG plane to alter electron trajectories, parallel magnetic fields do not directly impact the classical motion of electrons. Consequently, quantities such as conductivity, mobility, and magnetoresistance remain unaffected in the classical regime (Drude model). Hence, in weak parallel magnetic fields, the influence on the classical Drude conductivity is negligible. We neglect more subtle effects arising due to the modification of the wave function's shape across the quantum well.

However, a strong magnetic field can lead to spin polarization of an initially unpolarized and doubly degenerate electron gas. This occurs due to the Zeeman effect, as shown in Fig. 6.5. The latter shifts the corresponding conduction band bottom for each of the spin subsystems (sketched as the left and right gray bar, respectively) and creates thus a difference between them, equal to the Zeeman splitting. The critical magnetic field B_c describes the magnetic field, where the Zeeman splitting becomes equal to E_F, and is given by

$$B_\mathrm{c} = \frac{2E_F}{g^*\mu_B}. \tag{6.2}$$

The system will be completely spin-polarized, if ΔZ is larger than E_F. All electrons are then polarized along $B_\parallel$, from which a saturation follows. The development from $B_\parallel = 0$ to increasing parallel magnetic field is sketched in Fig. 6.5. Hence, the influence of $B_\parallel$ is limited [127]. For GaAs and HgTe, B_c is calculated in Tab. 6.1, showing that B_c is reached at much lower values for HgTe than for GaAs.

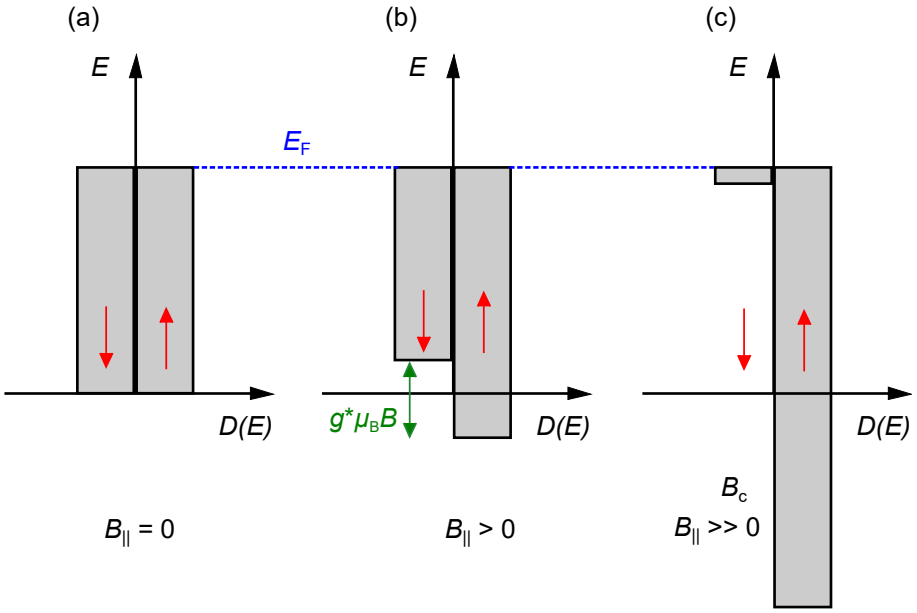

Fig. 6.5: Polarization of spin subsystems: transition from a doubly spin degenerate state to a fully polarized state with removed spin degeneracy. Energy is plotted against the DOS. The rectangles depict the states for spin systems filled from the bottom of the band up to E_F. (a) At $B_{\|} = 0$, both spins are represented equally. (b) At $B_{\|} > 0$, the amount of spin non-degenerate electrons increases due to Zeeman splitting (green). (c) At a magnetic field equal to or exceeding the critical field, all electrons are polarized along $B_{\|}$. For Si (which has a low g^*-factor and SOI comparable to GaAs), this behavior was reported in [127, 128]. The resistivity rises approximately twofold with $B_{\|}$ because of spin polarization. Then, it saturates at B_c, where $B_c = \frac{2E_F}{g^* \mu_B}$ is a very large value. Adapted from [60].

material and charge carrier type	g^*	m^*	calculated B_c
GaAs electrons	- 0.4	0.067 m_0	617.3 T
HgTe bulk electrons	20	0.03 m_0	27.5 T
HgTe bulk holes	4	0.15 m_0	27.5 T

Tab. 6.1: Parameters for different types of charge carriers: effective g-factor g^*, effective mass m^*, and resulting critical magnetic field B_c for GaAs and HgTe, where the Zeeman splitting becomes comparable to E_F. It determines the degree of polarization of the charge carriers with respect to their spin. For all listed charge carrier systems, we assume a charge carrier density of $n_s = 2 \cdot 10^{11} \mathrm{cm}^{-2}$. For HgTe, the values of g^* were estimated and valid for the case of 80 nm quantum wells, based on [114].

Complete spin polarization leads to a decrease in the density of states at the Fermi level, which in turn leads to an increase in the resistance of the two-dimensional system. The experimental fact that the magnetoresistance saturates above the critical magnetic field B_c, corresponding to a totally polarized electron system, is interpreted as a manifestation of the importance of the spin polarization. In Fig. 6.6, it is shown that the resistance rises twofold due to spin polarization, but then saturates at B_c, where $B_c = 2E_F/(g^*\mu_B)$ is very large [127].

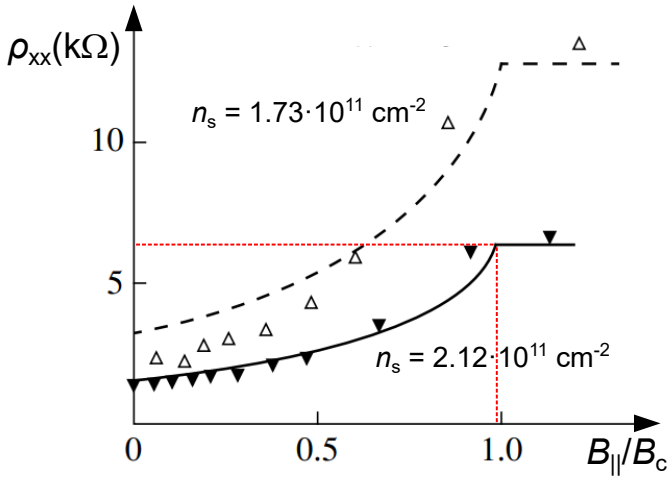

Fig. 6.6: Longitudinal resistivity ρ_{xx} as a function of $B_{\parallel}$ (normalized to the critical magnetic field B_c for complete spin polarization) for parameters corresponding to Si. The triangles are experimental results [129] for two different electron densities. The charge carrier density n_s, where B_c is reached, is marked with the red line. Adapted from [127].

6.3.3 Shubnikov-de Haas oscillations in tilted magnetic fields

A magnetic field applied perpendicularly to a 2D system leads to the formation of Landau levels. In a weak magnetic field, the distance between the levels does not exceed their broadening determined by the disorder in the system, and therefore, their presence does not manifest itself in the transport response. However, at sufficiently large values of $B_{\perp}$, the distance between them becomes larger than their width, leading to a modulation of the total density of states: its increase at the Landau level and its decrease in the gap between the levels. In turn, the modulation of the density of states at the Fermi level leads to a proportional and periodic change in conductivity, the Shubnikov-de Haas oscillations, directly measurable in experiment. By the amplitude of the oscillations (i.e., the depth of conductivity minima or the height of maxima), we can judge the size of the gap between neighboring levels.

Next, we consider the mechanism of the influence of the parallel component of the magnetic field on the oscillation pattern of bulk holes and, as a consequence, on the shape of the QPC conductance steps in the valence band. SdH oscillations were studied in 80 nm HgTe in tilted quantum wells. It is known that the dispersion is parabolic for bulk holes, which is confirmed by cyclotron resonance measurements [64]. For illustrative purposes, we begin with a comparison to the spectrum of Landau levels of a well-known classical system - electrons in GaAs, characterized, like holes in HgTe, by a parabolic dispersion, but, unlike them, by a much smaller value of Zeeman splitting. A schematic representation of the positions of Landau levels in a GaAs-based 2DEG as a function of the magnetic field is shown in Fig. 6.7 (a).

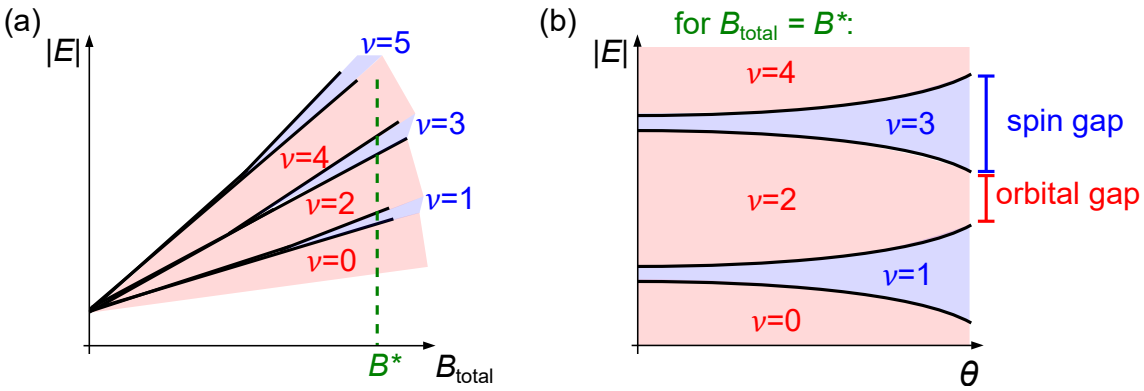

Fig. 6.7: Dispersion for ordinary parabolic systems such as GaAs and presumably the HgTe system: even filling factors are attributed to orbital/cyclotron gaps (red), odd ones to Zeeman gaps (blue). At low B fields, the effect of the Zeeman splitting is limited by Landau level broadening. (a) Energy of Landau levels in dependence of magnetic field. Spin degeneracy is present for lower magnetic field due to Landau level broadening. At strong B fields, the degeneracy is lifted by Zeeman splitting, giving rise to the odd filling factors. (b) Landau level order in an ordinary system in dependence of the tilt angle. The graph is shown for $B = B^*$ [60].

Due to the small value of the g^*-factor, in a weak magnetic field, each Landau level is doubly degenerate in spin, and therefore, only oscillations with even filling factors are observed in the system. In a strong magnetic field, the spin degeneracy is lifted and all filling factors are resolved, but because of the difference in the energy gap, the depth of minima for even and odd factors will differ significantly. Odd filling factors then correspond to spin gaps, and even ones to orbital gaps.

We recall that the total Zeeman splitting energy is defined by

$$\Delta Z = g^* \mu_B B = g^* \frac{\hbar q}{2m_e} B, \tag{6.3}$$

with m_e being the electron mass. If one keeps the the normal component of the

magnetic field constant, the Zeeman splitting energy at tilt angle θ is given by

$$\Delta Z = \Delta Z_0 \frac{1}{\cos\theta}. \tag{6.4}$$

Here, ΔZ_0 denotes the Zeeman splitting energy at $\theta = 0°$. The dependence on θ is illustrated in Fig. 6.7 (b). With increasing tilt angle, the energy of the first spin-split Landau level decreases. Evidently, the ratio between the orbital and spin gap is dependent on θ. Here, we introduce the factor $\frac{\Delta Z}{E_c}$. The ratio between the cyclotron energy E_c (see Eq. (2.23) in Chapter 2) and the Zeeman splitting energy ΔZ_0 is not known exactly and has to be estimated for our HgTe-based system. The energy parameters E_c and ΔZ for bulk electrons and holes in HgTe (estimated) and electrons in GaAs are presented in Tab. 6.2. For an increasing θ, Fig. 6.8 illustrates the change in the ratios between E_c and ΔZ and its resulting influence on conductivity.

If a gap increases (marked by the gray area in Fig. 6.8 (a) towards (b)), then the depth of the minimum of the oscillation corresponding to this gap increases as well (see Fig. 6.8 (c)). The Zeeman splitting increases due to a larger in-plane $B_\parallel$ field component, creating a larger gap. The corresponding σ_{xx} oscillation minimum in Fig. 6.8 (c) decreases and, consequently, can be assigned to a Zeeman gap. For a decreasing gap, the system behaves vice versa. The resulting σ_{xx} oscillation minimum increases and is assigned to an orbital gap.

material & charge carrier type	g^*	m^*	$E_c = \hbar\omega_c$	ΔZ_0	$\Delta Z_0/\hbar\omega_c$
GaAs electrons	- 0.4	0.067 m_0	8.6 meV	0.11 meV	0.012
HgTe bulk electrons	20	0.03 m_0	19.2 meV	28.8 meV	1.5
HgTe bulk holes	4	0.15 m_0	3.8 meV	5.7 meV	1.5

Tab. 6.2: Energy parameters for different types of charge carriers in GaAs (for comparison) and HgTe at $B_\perp = 5$ T: cyclotron energy E_c, (total) Zeeman splitting energy ΔZ_0 and the ratio between ΔZ_0 and E_c. We assume that $\Delta Z_0 = 1.5E_c$ for HgTe, an estimation based on previous works [114]. Considering the value of g^*, it should be mentioned that it is known from [130] and similar works, that the g^*-factor of HgTe shows an anisotropy with respect to the orientation of the B-field (perpendicular/parallel). However, within our simplified model, we neglect anisotropy for simplicity and suppose that g^* is a constant.

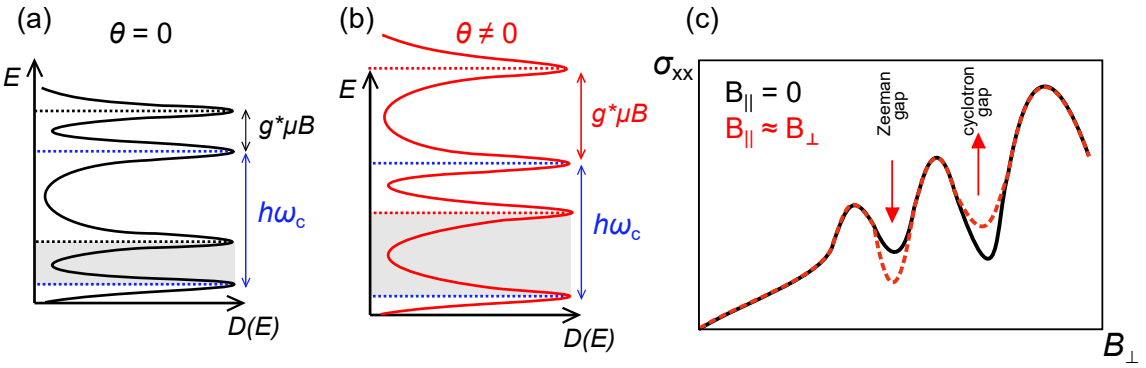

Fig. 6.8: The change of the ratio between orbital splitting and Zeeman splitting. (a) DOS for electrons in a purely perpendicular magnetic field. The DOS peaks are separated by $\hbar\omega_c$ (blue dashed lines). In addition, i.e., within this gap, the electron spin leads to a Zeeman splitting of Landau levels and to a lifting of the degeneracy by the term $g^*\mu_B B_{\text{total}}$. The gray area denotes an energy gap, which is formed by the Zeeman splitting. (b) Change of the ratio of distances between the DOS peaks due to an inclined magnetic field, influencing the magnitude of $g^*\mu_B B_{\text{total}}$. The energy gap has increased, leading to a decrease in conductivity. The spacing due to orbital splitting remains the same with respect to (a). (c) Resulting (longitudinal) conductivity σ_{xx} for (a) in black, showing SdH-type oscillations, and for (b) in red, showing an in- and decrease of odd and even minima, resp., highlighted by red arrows. The increase of the Zeeman gap (from (a) to (b)) correlates with the more pronounced minimum in σ_{xx}. Adapted from [45].

6.3.4 Effect of parallel magnetic field on the ballistic QPC conductance

In classical GaAs QPCs, the effect of a parallel magnetic field $B_\parallel$-component is very weak due to a negligible modification of the band structure of the QPC. While $B_\perp$ causes band depopulation, i.e., the amount of occupied 1D bands reduces as $B_\perp$ increases (see Fig. 2.13 in Chapter 2), in in-plane geometry, the effect is almost zero at $B_\parallel = 1.5$ T [131]. The observed effects are thus caused by the perpendicular component of the magnetic field only. Consequently, the effects arise exclusively from the 2-dimensional orbital motion of the electrons. Spin effects are irrelevant in this magnetic field range [131, 132]. Strong $B_\parallel$ removes spin degeneracy and resolves odd plateaus, as B is largely increased, giving rise to a strong Zeeman splitting. The general effect of $B_\parallel$ on the conductance steps is weakly pronounced in Ref. [19]. In Ref. [133], a rearrangement of bands at strong parallel magnetic fields is caused by Zeeman splitting. However, also here, the effect of $B_\parallel$ on the conductance is small, and is notable only for very high magnetic fields exceeding 10 T.

6.4 Experimental data analysis and discussion

6.4.1 Extraction of the energy gaps from conductivity minima

Now, we want to study the correlation between the QPC conductance and the behavior of the energy gaps of the 2DHG in the VB. For that, we analyze the conductivity σ_{xx} minima and its angular dependence.

In the QHE regime, the width of the ρ_{xy}-plateaus decreases and the ρ_{xx}-minima become less deep with increasing temperature T. In addition, the resistivity values at the minima in ρ_{xx} and, accordingly, maxima in σ_{xx} depend on T, reflecting a thermal activation of the charge carriers [45]. Thermal activation can be imagined as the phase in which a particle oscillates back and forth in the well. Within each period, there is a probability that the particle escapes the potential minimum over the barrier [47]. The conductance minima are then described by the Arrhenius law:

$$\sigma_{xx} = \sigma_0 \exp\left(\frac{-\Delta_{xx}}{2k_B T}\right), \tag{6.5}$$

with σ_0 the minimum conductivity for $\nu = 1, 2, 3, ...$ and Δ_{xx} the activation energy from the Fermi energy to the nearest unoccupied extended state near the center of the next higher Landau level [45]. Now, we would like to derive an equivalent to the activation energy from the measured conductivity. This equivalent term is given by the quotient

$$\lambda = \frac{\sigma_{xx\,\max}(\theta)}{\sigma_{xx\,\min}(\theta)} \approx \frac{\sigma_0}{\sigma_0 \exp\left(\frac{-\Delta_{xx}}{2k_B T}\right)} = \exp\left(\frac{\Delta_{xx}}{2k_B T}\right), \tag{6.6}$$

with the maximum conductivity $\sigma_{xx\,\max}$ of each SdH oscillation at given filling factor $\nu = i$, and $\sigma_{xx\,\min}$ the corresponding minimum. We assume the approximation $\sigma_0 \approx \sigma_{xx\,\max}$. The conductivity maxima are taken from neighboring half-integer filling factors. This expression can be transformed into

$$\ln \lambda = \frac{\Delta_{xx}}{2k_B T}, \tag{6.7}$$

which is a modification of the Arrhenius formula (from exponential to logarithmic function). Note that we performed our analysis on a data set obtained at a single temperature (same for all data). In order to emphasize that our technique is less precise in comparison to the temperature-dependent analysis, we refer to $\ln \lambda$ as the activation energy equivalent. This parameter depends on T, but it allows us to quantitatively compare the ratio between energy gaps of different filling factors.

In the following, we analyze the activation energy equivalent and its connection to the disappearance of oscillations in the conductivity. In Fig. 6.9 (a), the behavior of the resistance minima, originating from the QHE, is shown for selected tilt angles in

the VB. We observe a reduction of the oscillation minima at large enough tilt angles. Fig. 6.9 (b) shows the conductivity derived from (a) on a logarithmic scale and illustrates the activation energy (see Eq. (6.5)). The corresponding filling factor is attributed to each oscillation. Also, here, we notice the disappearance of oscillations, especially visible at $\nu = -3$ for instance. For simplicity, we focus on the absolute values of ν in the following considerations.

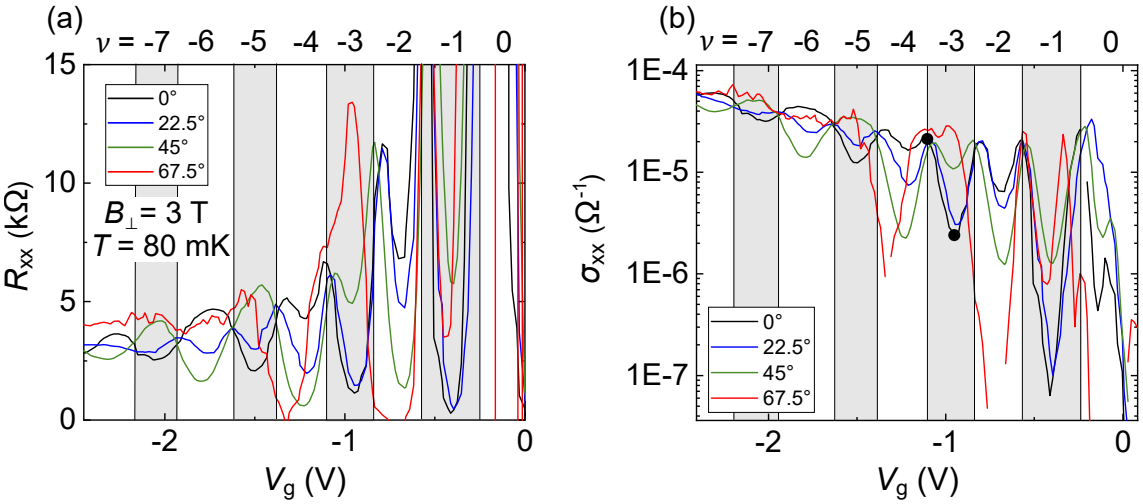

Fig. 6.9: (a) Longitudinal resistance of the macroscopic part of sample e23 for $\theta = 0°, 22.5°, 45°$ and $67.5°$ in dependence of V_g at $B_\perp = 3$ T, $T = 80$ mK. SdH oscillations in the VB are depicted. The odd minima turn into maxima with growing tilt angle, leading effectively to a reduction of oscillations. An example of this behavior is possible to see in particular at $\nu = -5$ for the black (0°) versus green (45°) curve, or at $\nu = -3$ for the black (0°) versus red (67.5°) curve. (b) Conductivity of the macroscopic part of the device for $B_\perp = 3$ T, shown in logarithmic scale. The activation energy equivalent, which will be discussed in Fig. 6.10, is extracted from measurements shown in the present graph. We use the following evaluation method in order to obtain a coefficient proportional to the activation energy: Minima of the SdH oscillations are subtracted from the maxima of traces at the same tilt angle (an example pair of a maximum and corresponding minimum is marked with black dots), yielding the value of the energy gaps for certain filling factors, measured in experiment. Some minima disappear (especially the 3rd and 5th). The resulting energy gaps are shown in Fig. 6.10.

In Fig. 6.10, the quotient λ, determined from Fig. 6.9 (b) for each ν, is plotted in logarithmic dependence of the tilt angle θ, showing a normalized energy proportional to the activation energy. An accurate determination of the gaps requires time-consuming temperature-dependent measurements. Therefore, our analysis has a rather qualitative character. Despite this, it still allows us to quantitatively compare the behavior of energy gaps corresponding to different Landau levels with each other. In the perpendicular magnetic field ($\theta = 0°$), the gaps with odd filling factors (1 and 3) appear larger than those with even ones (2 and 4). This observation corresponds to the calculations with the parameter $\Delta Z_0/\hbar\omega_c = 0.6$, presented in Fig. 6.4. However, further analysis reveals many discrepancies between Figs. 6.4 and 6.10. The gap magnitude for $\nu = 1$ at $\theta = 0°$ is approximately 2.5 times larger than all other gaps, which is unusual. Finally, there is a fundamental inconsistency in the dependence of the magnitude of the gaps on the tilt angle: while the calculations predict an increase in the energy gaps with odd factors (and a decrease in the even ones) as the tilt angle θ increases, the experimental data behave exactly the opposite way, i.e., the parity effect appears to be inverted. The possible factors leading to this will now be analyzed.

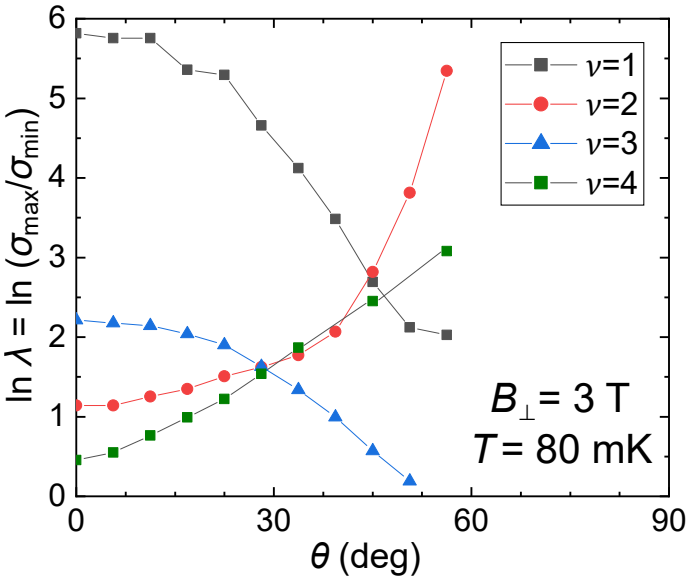

Fig. 6.10: The energy gaps with corresponding filling factors derived from measurements shown in Fig. 6.9 for the first four filling factors at $B_\perp = 3$ T in dependence of the tilt angle θ. The shown quantity is a coefficient proportional to the activation energy. The logarithm of λ (= the quotient of $\sigma_{xx,\,max}$ and $\sigma_{xx,\,max}$, y-axis) yields the activation energy equivalent. $\nu = 1$ (black) decreases with growing tilt angle, $\nu = 2$ increases, etc.. This inverted order of parity stands in contrast to the conventional GaAs-like system as introduced in Fig. 6.7, but is in line with the HgTe data, e.g., in Fig. 6.3.

6.4.2 Anomalously large magnitude of the Zeeman splitting

We recall that the value of the g^*-factor for holes in HgTe quantum wells can depend on many factors, such as the thickness of the well, the surface orientation, the charge carrier concentration, and even the applied gate voltage through the Rashba-like effect. Therefore, despite a sufficient number of publications dedicated to measuring this value [75, 76, 82, 124, 134], their results are not directly applicable to the system under study due to the differences in the parameters listed. Neither can numerical calculations serve as a reliable source of information, because they have difficulties with the exact calculation of the valence band and cannot even unambiguously explain the absence of valley degeneracy [135], which is lifted for unclear reasons and was not observed in any experiment known to us (and even the value of the effective mass of holes for 80 nm HgTe was not measured). Thus, the g^*-factor is a free fitting parameter. The primary estimate of the g^*-factor ($\Delta Z_0/\hbar\omega_c = 0.6$, experimentally derived in Fig. 6.9 (a) for $\theta = 0°$) was obtained from the analysis of the behavior of the SdH oscillations in a perpendicular magnetic field: since the minima with odd filling factors are deeper than those with even ones, the spin gaps have to be smaller than the orbital gaps. This indicates a relation between the spin gaps and the cyclotron gaps of $\Delta Z_0 \approx 1.5\ |\hbar\omega_c - \Delta Z_0|$, which is equal to $0.6\ \hbar\omega_c$. Here, the left side of the equation corresponds to the gap for odd filling factors (spin gaps $= \Delta Z_0$), and the right side indicates the even filling factors (cyclotron gaps $= \hbar\omega_c - \Delta Z_0$). The value of 1.5 is roughly estimated by eye from Fig. 6.9 (a): For the black curve (0°), the ratio between orbital to spin gaps is estimated to 1.5, or, if transformed into the ratio $\Delta Z_0/\hbar\omega_c$, to 0.6. Based on this observation, we choose the value $\Delta Z_0/\hbar\omega_c = 0.6$. This is also consistent with the estimates from Ref. [114] and the graph in Fig. 6.4. The latter were adapted to our system and are presented in Fig. 6.11 (a), with the spin gaps represented in blue and the orbital gaps in red. However, the calculations thus obtained qualitatively contradict the dependence on the tilt angle, which was shown in Fig. 6.10. It is also evident in Fig. 6.3, where the plateau shrinks for $\nu = -3$ with increasing tilt angle. In other words, for increasing tilt angles, this primary estimate of 0.6 no longer corresponds to the experimental data.

On the other hand, the requirement that spin gaps are larger than orbital gaps ($\Delta Z_0 > |\hbar\omega_c - \Delta Z_0|$) can be fulfilled at other, larger values of ΔZ_0, for example, at $\Delta Z_0/\hbar\omega_c = 1.5$. Note that this factor 1.5 may not be confused with the factor 1.5 in the discussion related to Fig. 6.11 (a). The calculations obtained at this spin splitting are presented in Fig. 6.11 (b). Due to the fact that the spin splitting even in a perpendicular magnetic field exceeds E_c, the sequence of Landau levels is broken, and one can no longer unambiguously associate even or odd filling factors with an orbital or spin gap. The formerly introduced assignment of colors in (a), with blue corresponding to spin gaps, does not apply to (b) anymore, as spin gaps cover the range of several filling factors. This is indicated by the span of ΔZ in green, which includes the filling factors $\nu = 4, 5, 6$ in this case. However, the break of the pattern

as shown in (a) is helpful for the description of our experimental observations. First, in a perpendicular magnetic field, the gaps with odd filling factors appear larger than those with even ones. The gap between the first and the second Landau level, which corresponds to filling factor 1, is significantly larger than all other gaps. Second, the gaps with even filling factors increase, as they should, as the tilt angle increases, while the odd ones, on the contrary, decrease. Third, odd gaps collapse at a tilt angle of about 45°, which also corresponds to the dependences in Fig. 6.10. The only discrepancy is that the calculated behavior of the first gap as a function of the angle does not coincide with the experiment. However, in such a simplified model, this can be neglected, as it does not take into account the presence of other types of charge carriers (electrons). Another possible explanation is the Dirac-like non-parabolicity, which is not foreign to our system. According to Fig. 6.11 (b), the energy gaps of the filling factors for the same parity and greater than 2 are the same. However, in experiment, we observe the tendency that minima with larger negative filling factors become less deep. This points to non-parabolic behavior of our system.

To conclude, we can state that bulk holes are characterized by a ratio of Zeeman splitting and cyclotron energy greater than 1. We suppose that the energy dispersion is parabolic with minor non-parabolicity. However, our study did not focus on this aspect. The exact mechanism could only be revealed using a sophisticated model of the band structure, taking into account more precise SOI parameters and a detailed wave function, which would describe possible interactions between the subbands.

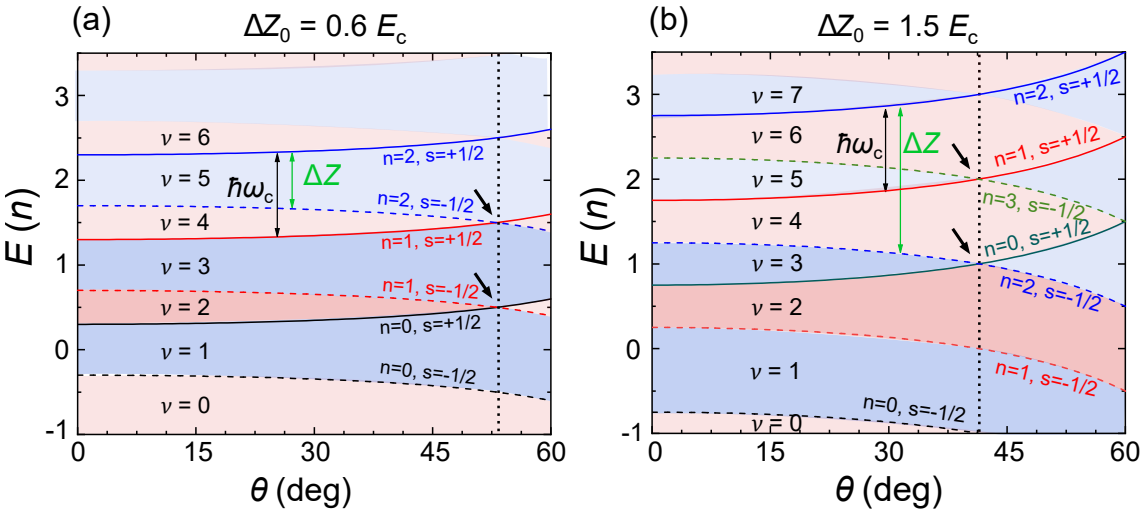

Fig. 6.11: Calculated energy (normalized to E_c), showing the dependence of the Landau levels n at fixed $B_\perp = 3$ T as a function of the tilt angle θ for the cases of (a) $\Delta Z_0 = 0.6\ E_c$ and (b) $\Delta Z_0 = 1.5\ E_c$. The cyclotron energy E_c (black) and Zeeman energy ΔZ (green) are marked. E_c remains constant with growing θ, while ΔZ increases. We draw our attention especially to the first three filling factors (colored in more saturated colors). Even filling factors are colored in red, odd ones in blue. The first filling factor corresponds to $\nu = 1$. ($\nu = 0$ and $n = -1$ are illustrated to complete our image, but have no significance in our model.) In (a), $\nu = 1$ increases with growing θ, $\nu = 2$ decreases and $\nu = 3$ increases. The parity of the Landau levels does not reflect our experimental data, presented in Fig. 6.10. $\nu = 1$ is supposed to decrease with growing θ, $\nu = 2$ to increase etc.. Here, the blue filling factors correspond to spin gaps, red ones to orbital gaps (without the spin gaps). (b) For larger Zeeman splitting $\Delta Z_0 = 1.5\ E_c$, an inversion of the parity of the energy levels with respect to (a) takes place, evident if we look at $\nu = 1$, which stays constant with growing θ (due to constant E_c), $\nu = 2$ increases, $\nu = 3$ decreases. This is the opposite behavior to (a), and at the same time the targeted scenario, in which the experimental findings from Fig. 6.10 are reflected. The angle θ, at which a crossing of two Landau levels occurs, is smaller for $\Delta Z_0 = 1.5\ E_c$ than in (a) with $\theta \approx 40°$, which is closer to our measured data. In (b), the assignment of blue color to spin gaps does not apply anymore, as the situation is more complicated. For example, the spin gap for $n = 2$ includes $\nu = 4, 5, 6$. Because of the parity order following the experimental results shown in Fig. 6.10, we conclude that the parameters chosen in (b) describe our system best, revealing a system with a ratio of Zeeman splitting and cyclotron energy larger than 1.

6.5 Summary

A parity effect in the sequence of conductance steps was observed in the valence band, when applying a tilted magnetic field, meaning that every second step disappeared at high inclined magnetic fields. At even higher inclined magnetic fields, the disappeared steps re-appeared again. It led us to a condition for a large Zeeman splitting, assuming that $\Delta Z_0 = 1.5\ E_c$, which is much higher than what is found in classical 2DEG/2DHG systems such as GaAs/AlGaAs heterostructures, though it is in line with observations made in thinner HgTe QWs [75]. With this, we were able to model the sequence of Landau levels in accordance with our measurements, especially incorporating the parity. In summary, the pattern of QPC conductance steps on the hole side is determined mainly by a specific sequence of Landau levels of heavy holes with parabolic dispersion, which leads to a broken parity of filling factors in comparison with classical 2DEG systems. For $\Delta Z_0 > E_c$, the parity of the filling factors is consistent with our measurements.

In conclusion, the influence of an inclined magnetic field on the sequence of filling factors is quite unusual, but it correlates with the behavior of the QPC conductance. Although the exact mechanism remains unclear, i.e., the reason for the large Zeeman splitting, the unusual behavior could be explained by a non-trivial band structure of the valence band including strong SOI, which might influence the Landau levels band dispersion in an unknown way. Overall, the initial hypothesis is valid, namely that the behavior of QPC conductance reflects the properties of 2DEG/2DHG, i.e., its reaction to the magnetic field, making it the main conclusion. At the same time, we did not find any effects caused by the intrinsic QPC response (related, for example, to the rearrangement of the QPC spectrum) to the tilted magnetic field neither in the valence band nor in the conduction band. This may be due to both the insufficient quality of the structures (high disorder in QPCs), as well as due to deeper phenomena related to the topological nature of the electrons, forming the conduction of QPC.

7. Conclusions and outlook

This thesis describes quantum transport in HgTe 3D topological insulator quantum point contacts. The main focus lies with the study of transport properties of point contacts with different dimensions and characteristic conductance ranging from 1 to 100 e^2/h exposed to quantizing magnetic fields in perpendicular direction to the sample plane. An appropriate model to describe the essential physics of conductance and transmission at a QPC was developed. These results were published in Ref. [43].

All investigated quantum point contacts exhibited the absence of conductance quantization in zero magnetic field, regardless of the conductance value (see Sec. 5.2). The observed steps are characterized by anomalous non-integer conductance values that persist over a wide range of magnetic fields, gate voltages, and temperatures, implying an underlying preferred scattering mechanism within the QPCs. An analysis of the transport response of macroscopic regions of the sample suggests that the conductance behavior of the QPC largely reflects the properties of adjacent regions with two-dimensional carriers. This is evident from the fact that, for a given B and V_g, the step number matches the QHE filling factor of the one for two-dimensional electrons or holes. In this case, the QPC acts as a selective filter that partially transmits QHE edge states. The constancy of the transmission coefficient of this filter is a striking and unusual result, which is not typical for one-dimensional systems. A possible reason for the lack of quantization is the non-adiabaticity of QPC boundaries, a consequence of their fabrication using etching lithographic techniques.

The occurrence of steps was reproduced in cooperation with the group of Klaus Richter by numerical tight-binding calculations, performed by Michael Barth, using the Python package KWANT, presented in Sec. 5.5. We refrained from the use of a more sophisticated, but speculative 3D model and based our theoretical approach on an effective model, describing a 2D electron conduction band. The calculations indicate that, besides the cross section of the constriction, disorder in the point contact plays a leading role in the atypical quantization sequences. Modeling the disorder phenomenologically by using a Landauer-Büttiker model, we deduced that the conductance steps can be described by $G = \frac{Nk}{N+k}\frac{e^2}{h}$, where N is the number of edge modes in the wide regions outside the QPC, equivalent to the filling factor, and k is the number of modes inside the QPC, equal to the conductance in units of e^2/h at zero magnetic field.

It was further found that the devices under study inevitably fall into one of two

groups (see Sec. 5.3): Group A, characterized by lower conductance steps, starting at $G = 0.6\ e^2/h$ for the first step, and group B, which showed larger step heights, with $G = 0.85\ e^2/h$ for the first step. These values apply in the presence of strong magnetic fields. Samples with other conductivity values were absent. Falling into one group or the other correlates with the QPC cross section, but because of an unpredictable factor associated with a random electrostatic potential distribution, the correlation shows a strong variation. However, the separation into groups could be well predicted by the conductance at zero magnetic field.

For larger point contacts (group C, see Sec. 5.6), the conductance behavior transitioned from step-like to oscillation-like patterns, resembling Shubnikov–de Haas oscillations. This transition points to a behavior gradually moving from the mesoscopic regime with well-defined conductance steps to a more macroscopic transport regime dominated by oscillatory conductance of strongly grown absolute values (up to $G = 100\ e^2/h$), as the QPC width increased.

In tilted magnetic fields (see Sec. 6.2), i.e., adding a parallel magnetic field component (with respect to the wire axis), the behavior of the conductance of the QPCs shows the following changes: On the electron side (CB), the difference between two cases is almost negligible, proving the topological nature of electrons (i.e., their insensitivity to a parallel magnetic field) dominating the transport. However, on the hole side (VB), the distinctness of the steps was found to be sensitive to the parallel component of the magnetic field. Moreover, an unusual feature was found: The behavior of steps with even and odd numbers exhibited an opposite trend, which we refer to as the parity effect: As the tilt angle of the magnetic field increases, the even steps become more pronounced, while the steps corresponding to odd filling factors become blurred and eventually disappear.

An analysis of SdH oscillations and the QHE in the macroscopic part of the sample under the same conditions (treated in Sec. 6.4) confirms the correlation between the transport properties of the macroscopic regions and the conductance quantization in the QPC. The observed parity effect is related to the interplay between the cyclotron gap and the Zeeman splitting of 2D holes in the regions adjacent to the QPC. The disappearance of odd plateaus at a certain critical tilt angle is associated with the collapse of the energy gap between neighboring Landau levels and their degeneracy. A quantitative analysis of the effect demonstrated that agreement with the experimental data can only be achieved by introducing a Zeeman splitting ΔZ_0 that exceeds the cyclotron energy in a perpendicular magnetic field, with $\Delta Z_0 = 1.5 E_c$. This large value is anomalous for classical 2DEGs/2DHGs such as in GaAs, but is also observed in similar HgTe systems [75]. Our analysis suggests that the system is dominated by heavy holes with parabolic dispersion, leading to an inversion of the usual parity sequence of Landau levels.

Finally, I would like to give an outlook on this work. The results obtained lay the foundation for further studies on more intricate systems. These could be shaped topological nanowires with more complex geometries such as varying cross sections, as depicted in Fig. 7.1 (a), similar to 1D QH interferometers [44, 136]. An arbitrary shape (examples depicted in Figs. 7.1 (c) and (d)) would allow the design of nanowires with custom-tailored magnetic flux barriers, enabling the confinement of Dirac electrons. The energy spectrum would then be characterized by

$$E_{nl} = \frac{\hbar\omega_c}{R}\sqrt{\left(l + \frac{1}{2} - \frac{\phi}{\phi_0}\right)^2 + \left(n\pi\frac{R}{L}\right)^2}, \tag{7.1}$$

with n, l the quantum numbers, R the radius of the quantum dot, L the constriction distance, ϕ the magnetic flux, ϕ_0 the flux quantum and $+\frac{1}{2}$ the Berry phase[1] γ_n [44, 66].

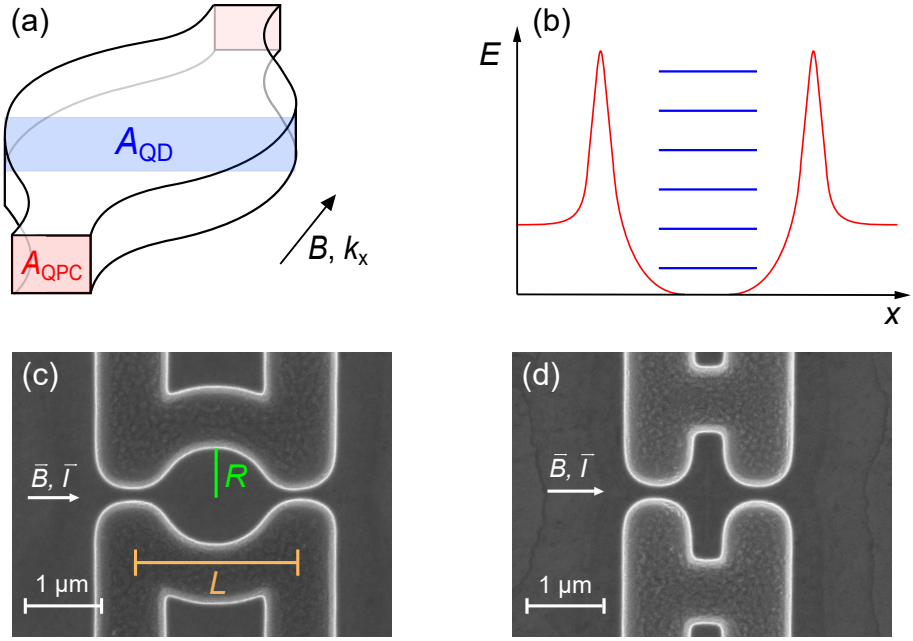

Fig. 7.1: (a) Suggested quantum dot device based on a double QPC structure. (a) Shaped nanowire with differing cross sections A_{QPC} and A_{QD} in an axial magnetic field B. Based on device as calculated in Ref. [44]. (b) Quantized energy levels (blue lines), similar to a quantum dot (QD), are expected to form between the point contact barriers (red). (c) and (d): SEM images of nanowires with varying cross section (fabricated for dose tests). In (c), the radius R (green) of the quantum dot is comparable to the length L (orange) of the shaped nanowire, while in (d), the radius is smaller in comparison with the length. The distance between the imagined discrete energy levels shown in (b) can be varied then. In the case of (d), they would have larger distances compared to (c).

[1] Here, the Berry phase is normalized to 2π.

Thus, a wide range of possibilities could be created, for example, to investigate the Coulomb blockade (illustrated in Fig. 7.1 (b)) in an in-plane magnetic field in Dirac electron systems [137]. This future work could combine the results of this doctoral thesis and the one of Johannes Ziegler [49], in which Aharonov-Bohm type oscillations on nanowires in in-plane magnetic field were investigated. For this purpose in particular, MBE-grown films offer the opportunity to design shaped nanowires. By contrast, this is not possible with core-shell nanowire QPCs [8]. However, in our system, we then have to take into account the interplay of two constrictions, instead of only one, exhibiting anomalous, non-quantized conductance steps if strong disorder is present in the constrictions, which might become challenging in its interpretation. For a better understanding of the 3D TI system, constructing an accurate 3D Hamiltonian might make it easier to work more reliably with non-quantized values. In any case, it would be essential to know the origin of the non-present quantization. With that said, the anomalous steps open up the question, if quantization can be achieved at all in thin-film 3D TI HgTe-based QPCs. On the contrary, we could even take advantage of those by uncovering a hidden mechanism, a yet unknown characteristic in the band structure, which forces the conductance to appear at precisely the observed values of the conductance.

A more general outlook would be to study TI-based QPCs or nanowires in general (i.e., including those with larger dimensions, not only QPCs), that could host Majorana bound states [33]. Proposals based on QPC devices allow spectroscopy of topological superconductivity [32, 34, 138] and the tuning of topological edge states [139]. In any case, TI QPCs are a fascinating tool not only for studying fundamental aspects of physics, but also for future revolutionary technical applications in quantum computing.

The absoluteness of quantization - free of room for any reinterpretation - makes QPCs irreplaceable in the study of elementary quantum transport. It is something that we can rely on, the building block of everything, which is - in the true sense of the word - true [140]. It was thanks to QPCs that the discovery of the conductance quantum was possible - something universal, forever valid, and, to cite Klaus von Klitzing one more time, “that remains, that is immortal” [141].

A. Fabrication guide

Splitting wafers	
protective resist	S1813 photoresist at 1500 rpm / 500 rpm/s / 30 s
bake-out	5 min at 80° C
scribe wafer	larger than size of structure 2.8 mm ×3.5 mm
split wafer	split over glass edge with clean tape
Standard cleaning	
acetone bath	5 min at 60° C
isopropanol bath	5 min
drying	N_2
Mesa	
standard cleaning	see above
spin coating	S1813 photoresist at 6000 rpm / 4000 rpm/s / 30 s
bake-out	5 min at 80° C
optical lithography	mask 'Novo1', exposure 90 s (depending on age of Hg lamp)
develop	MF26A for ca. 2 min
	distilled water 30 s
wet-chemical etching	$H_2O : C_2H_6O_2 : Br_2 = 25 : 100 : 0.1$ ml at 0° C
duration	2 min 30 s −4 min
standard cleaning	
Nanostructures	
standard cleaning	
spin coating	EBL resist PMMA 950K 4% at 3000 rpm / 4000 rpm/s
	for 5 s and
	800 rpm / 1000 rpm/s / 30 s
bake-out	30 min at 80° C
exposure	EHT (electron high tension): 3 kV, aperture: 20 µm,
	area dose: $140 - 250$ µC/cm²
	(Dose tests shortly before fabrication are necessary, as the

	resist texture depends on the age of the liquid resist.)
develop	2 min in MIBK : isopropanol = 1 : 3 30 s in isopropanol
wet-chemical etching	10 - 30 s (Depending on the structure, etching tests before fabrication are necessary).

Topgate	
Oxide layers	
PECVD	30 nm SiO_2 at 80° C
ALD	100 nm Al_2O_3 at 80° C
Metalization	
standard cleaning	
spin coating	S1813 photoresist at 6000 rpm / 4000 rpm/s / 30 s
bake-out	5 min at 80° C
optical lithography	mask 'Novo1', exposure 90 s (depending on age of Hg lamp)
develop	MF26A for approx. 2 min distilled water 30 s
thermal evaporation	no pre-sputtering Ti: 5 nm Au: 80 nm
lift-off	acetone at 60° C for at least 3 h flush sample with acetone from syringe optical check in isopropanol bath dry with N_2

Contacts	
soldering	with a fine soldering iron tip at $V \approx 7$ V, $I \approx 0.9$ A scratch oxide on contact pads with fine needle apply In drops onto contacts
chip carrier	mount sample with two-component silver epoxy adhesive EpoTek EE129-4, mix at ratio 1 : 1, bake out 2 h at 80° C

B. Material and device overview

B.1 Used material systems

wafer	growth direction	HgTe / CdHgTe buffer / CdTe cap (nm)	samples (used for)
191004	(013)	30 / 20 / 0	e14 (macroscopic characterization) e23 (devices A1 and B1)
170713	(013)	50 / 20 / 40	e8 (device B2) e9 (devices A2 and A3) s62 (device A4) s83 (devices C1 and C2)
180907	(013)	50 / 30 / 20	e32 (devices C3 and C4)
140826	(013)	80 / 20 / 40	e28 (device B3)
180910	(013)	80 / 20 / 40	j4 (devices C5 and C6)

Tab. B.1: Parameters of used HgTe wafers and their use, including the crystal growth direction and heights of the MBE-grown layers. Only samples treated in this thesis are listed. Sample s83 was fabricated by Johannes Ziegler and sample j4 by Juliane Steidl.

B.2 Device list

device	w (nm)	h (nm)	cross section A (nm^2)	first step in $G(e^2/h)$
A1 (e23w1)	580	30	17 400	0.53
A2 (e9w2)	140	50	7 000	0.6
A3 (e9w1)	95	50	4 750	0.6
A4 (s62w1)	85	50	4 250	0.55
B1 (e23w2)	710	30	21 300	0.9
B2 (e8w2)	200	50	10 000	0.87
B3 (e28w2)	135	80	10 800	0.85
C1 (s83w1)	580	50	29 000	1.3
C2 (s83w1)	580	50	29 000	1.3
C3 (e32w1)	1 000	50	50 000	2.0
C4 (e32w2)	2 000	50	100 000	2.0
C5 (j4w2)	5 000	80	400 000	2.7
C6 (j4w1)	10 000	80	800 000	3.0

Tab. B.2: Geometrical parameters width w, height h and cross section A of the discussed devices. The length is $l = 400 - 500$ nm for all QPC devices. These do not include C1 and C2, which are long wires with $l = 1500$ nm and 2500 nm, respectively, instead of short QPCs. The characteristic conductance values of the first step are listed. The area of the cross section is calculated from height and width of the wires at the narrowest point, for simplicity assumed to be rectangular. The original terminology used during the fabrication and measurement period is indicated in parentheses.

C. Supplemental theoretical considerations

C.1 Landauer-Büttiker formalism for a QPC system with six terminals

We consider a 2D TI model, based on the assumption that the bulk 3D TI layer is squeezed into two dimensions as described in [114]. To describe the transmission through a constriction, we assume a 6-terminal geometry based on the Landauer-Büttiker formalism. The following system of equations represents the entries in Eq. (5.12), and was introduced in this form by Michael Barth in order to simulate the experimental data. Here, N denotes the number of edge states, t the number of transmitted states and r the number of reflected states. The numbering of the contacts $1-6$ is in accordance with Fig. 5.9.

$$\begin{pmatrix} I \\ 0 \\ 0 \\ -I \\ 0 \\ 0 \end{pmatrix} = \frac{e^2}{h} \begin{pmatrix} N & 0 & 0 & 0 & 0 & -N \\ -N & N & 0 & 0 & 0 & 0 \\ 0 & -t & N & 0 & -r & 0 \\ 0 & 0 & -N & N & 0 & 0 \\ 0 & 0 & 0 & -N & N & 0 \\ 0 & -r & 0 & 0 & -t & N \end{pmatrix} \begin{pmatrix} V_1 \\ V_2 \\ V_3 \\ V_4 \\ V_5 \\ V_6 \end{pmatrix} \tag{C.1}$$

We fix the drain potential $V_4 = 0$ as a reference point. From the resulting system of equations, we obtain for the Hall, longitudinal and diagonal conductance signal at the QPC:

$$G_{xy} = G_{\text{Hall}} = \frac{e^2}{h} N \tag{C.2}$$

$$G = G_{xx \text{ / longitudinal (QPC)}} = \frac{e^2}{h} \frac{Nt}{r} \tag{C.3}$$

$$G_d = G_{\text{diagonal}} = \frac{e^2}{h} t \tag{C.4}$$

C.2 Landauer-Büttiker formalism for a QPC system with eight terminals

The toy model presented in Sec. 5.5.4 uses a matrix based on the Landauer-Büttiker formalism including the additional thermalization contacts 7 and 8. Here, N is the number of edge states and k determines the number of modes in the QPC. The numbering of the contacts 1-8 is according to Fig. 5.15.

$$\begin{pmatrix} I \\ 0 \\ 0 \\ -I \\ 0 \\ 0 \\ 0 \\ 0 \end{pmatrix} = \frac{e^2}{h} \begin{pmatrix} N & -N & 0 & 0 & 0 & 0 & 0 & 0 \\ 0 & N & 0 & 0 & 0 & 0 & -N & 0 \\ 0 & 0 & N & -N & 0 & 0 & 0 & 0 \\ 0 & 0 & 0 & N & -N & 0 & 0 & 0 \\ 0 & 0 & 0 & 0 & N & 0 & 0 & -N \\ -N & 0 & 0 & 0 & 0 & N & 0 & 0 \\ 0 & & 0 & 0 & 0 & -N & N+k & -k \\ 0 & 0 & -N & 0 & 0 & 0 & -k & N+k \end{pmatrix} \begin{pmatrix} V_1 \\ V_2 \\ V_3 \\ V_4 \\ V_5 \\ V_6 \\ V_7 \\ V_8 \end{pmatrix} \tag{C.5}$$

From this, we obtain

$$G_{xy} = G_{\text{Hall}} = \frac{e^2}{h} N \tag{C.6}$$

$$G = G_{xx \text{ / longitudinal (QPC)}} = \frac{e^2}{h} \frac{kN}{k+N} \tag{C.7}$$

$$G_d = G_{\text{diagonal}} = \frac{e^2}{h} \frac{kN}{2k+N} \tag{C.8}$$

C.3 2D Bernevig-Hughes-Zhang Hamiltonian

The so-called 2D Bernevig-Hughes-Zhang (BHZ) Hamiltonian for HgTe quantum wells [93] reads in the basis $|E1\uparrow\rangle$, $|H1\uparrow\rangle$, $|E1\downarrow\rangle$, and $|H1\downarrow\rangle$

$$H_{BHZ} = \begin{pmatrix} h(\mathbf{k}) & \begin{matrix} 0 & 0 \\ 0 & 0 \end{matrix} \\ \begin{matrix} 0 & 0 \\ 0 & 0 \end{matrix} & h^*(-\mathbf{k}) \end{pmatrix}, \tag{C.9}$$

with

$$h(\mathbf{k}) = \begin{pmatrix} C - (B+D)\mathbf{k}^2 + M & Ak_+ \\ Ak_- & C + (B-D)\mathbf{k}^2 - M \end{pmatrix}. \tag{C.10}$$

The momentum operators are given by $\mathbf{k}^2 = k_x^2 + k_y^2$ and $k_\pm = k_x \pm ik_y$. We use the Hamiltonian parameters $A = 364.5$ meV $\cdot$ nm, $B = -686$ meV $\cdot$ nm^2, $C = 0$, $D = -512$ meV $\cdot$ nm^2, and $M = -10$ meV which correspond to a 7 nm thick HgTe quantum well [121, 142]. Furthermore, we also take into account additional Hamiltonian terms originating from bulk inversion asymmetry and structure inversion asymmetry [96, 121, 142]

$$H_{BIA} = \begin{pmatrix} 0 & 0 & 0 & -\Delta \\ 0 & 0 & \Delta & 0 \\ 0 & \Delta & 0 & 0 \\ -\Delta & 0 & 0 & 0 \end{pmatrix} \tag{C.11}$$

and

$$H_{SIA} = \begin{pmatrix} 0 & 0 & -iRk_- & 0 \\ 0 & 0 & 0 & 0 \\ iRk_+ & 0 & 0 & 0 \\ 0 & 0 & 0 & 0 \end{pmatrix}, \tag{C.12}$$

with the parameters $\Delta = 1.6$ meV and $R = -15.6$ meV $\cdot$ nm. For the latter term, we simplified the Hamiltonian and neglected the linear dependence of R on the gate voltage-induced electric field. Finally, we also include the Zeeman effect via [96]

$$H_Z = \begin{pmatrix} g_E\mu_B B_z & 0 & 0 & 0 \\ 0 & g_H\mu_B B_z & 0 & 0 \\ 0 & 0 & -g_E\mu_B B_z & 0 \\ 0 & 0 & 0 & -g_H\mu_B B_z \end{pmatrix}, \tag{C.13}$$

with the g^*-factors given by $g_E = 22.7$ and $g_H = -1.21$.

References

1. Von Klitzing, K. The quantized Hall effect. *Review of Modern Physics* **58,** 519 (1986).
2. Aristotle. *Posterior Analytics II.19* (Presses Université Laval, 2004).
3. Feynman, R. Simulating physics with computers. *International Journal of Theoretical Physics* **21,** 467–488 (1982).
4. Kane, C. L. & Mele, E. J. Z2 topological order and the quantum spin Hall effect. *Physical Review Letters* **95,** 146802 (2005).
5. Fu, L., Kane, C. L. & Mele, E. J. Topological insulators in three dimensions. *Physical Review Letters* **98,** 106803 (2007).
6. Bernevig, B. A., Hughes, T. L. & Zhang, S. C. Quantum spin Hall effect and topological phase transition in HgTe quantum wells. *Science* **314,** 1757–1761 (2006).
7. König, M., Wiedmann, S., Brüne, C., Roth, A., Buhmann, H., Molenkamp, L. W., Qi, X.-L. & Zhang, S.-C. Quantum spin Hall insulator state in HgTe quantum wells. *Science* **318,** 766–770 (2007).
8. Strunz, J., Wiedenmann, J., Fleckenstein, C., Lunczer, L., Beugeling, W., Müller, V. L., Shekhar, P., Ziani, N. T., Shamim, S., Kleinlein, J., Buhmann, H., Trauzettel, B. & Molenkamp, L. W. Interacting topological edge channels. *Nature Physics* **16,** 83–88 (2020).
9. Majorana, E. Teoria simmetrica dell'elettrone e del positrone. *Il Nuovo Cimento* **14,** 171–184 (1937).
10. Fu, L. & Kane, C. L. Superconducting proximity effect and Majorana fermions at the surface of a topological insulator. *Physical Review Letters* **100,** 096407 (2008).
11. Beenakker, C. Search for Majorana fermions in superconductors. *Annual Review of Condensed Matter Physics* **4,** 113–136 (2013).

12. Zhang, H., Liu, C., Xu, D., Gazibegovic, S., Logan, J. A., Wang, G., van Loo, N., Bommer, J. D. S., de Moor, M. W. A., Car, D., het Veld, R. L. M. O., van Veldhoven, P. J., Koelling, S., Verheijen, M. A., Pendharkar, M., Pennachio, D. J., Shojaei, B., Lee, J. S., Palmstrøm, C. J., Bakkers, E. P. A. M., Sarma, S. D. & Kouwenhoven, L. P. RETRACTED ARTICLE: Quantized Majorana conductance. *Nature* **556,** 74–79 (2018).

13. Dvir, T., Wang, G., van Loo, N., Liu, C.-X., Mazur, G. P., Bordin, A., Sebastiaan L. D. ten Haaf, J.-Y. W., van Driel, D., Zatelli, F., Xiang Li, F. K. M., Gazibegovic, S., Badawy, G., Bakkers, E. P. A. M., Wimmer, M. & Kouwenhoven, L. P. Realization of a minimal Kitaev chain in coupled quantum dots. *Nature* **614,** 445–450 (2023).

14. Aasen, D. Roadmap to fault tolerant quantum computation using topological qubit arrays. *Preprint at arXiv* (2025).

15. Fischer, R., Picó-Cortés, J., Himmler, W., Platero, G., Grifoni, M., Kozlov, D. A., Mikhailov, N. N., Dvoretsky, S. A., Strunk, C. & Weiss, D. 4π-periodic supercurrent tuned by an axial magnetic flux in topological insulator nanowires. *Physical Review Research* **4,** 013087 (2022).

16. Himmler, W., Fischer, R., Barth, M., Fuchs, J., Kozlov, D. A., Mikhailov, N. N., Dvoretsky, S. A., Strunk, C., Gorini, C., Richter, K. & Weiss, D. Supercurrent interference in HgTe-wire Josephson junctions. *Physical Review Research* **5,** 043021 (2023).

17. Hartl, S. *Quantum transport in topological insulators and nanopatterned superconducting systems* Dissertation (Universität Regensburg, 2024).

18. Van Wees, B. J. Quantized conductance of point contacts in a two-dimensional electron gas. *Phys. Rev. Lett.* **60,** 848–850 (1988).

19. Wharam, D. A., Thornton, T. J., Newbury, R., Pepper, M., Ahmed, H., Frost, J. E. F., Hasko, D. G., Peacock, D. C., Ritchie, D. A. & Jones, G. A. C. One-dimensional transport and the quantisation of the ballistic resistance. *Journal of Physics C: Solid State Physics* **21,** L209–L214 (1988).

20. Landauer, R. Spatial variation of currents and fields due to localized scatterers in metallic conduction. *IBM Journal of Research and Development* **1,** 223–231 (1957).

21. Van Houten, H. & Beenakker, C. W. J. Quantum point contacts. *Physics Today* **49,** 22–27 (1996).

22. Büttiker, M. Four-terminal phase-coherent conductance. *Physical Review Letters* **57,** 1761–1764 (1986).

23. Krans, J. M., van Ruitenbeek, J. M., Fisun, V. V., Yanson, I. K. & de Jongh, L. J. The signature of conductance quantization in metallic point contacts. *Nature* **375,** 767–769 (1995).

24. Requist, R., Baruselli, P. P., Smogunov, A., Fabrizio, M., Modesti, S. & Tosatti, E. Metallic, magnetic and molecular nanocontacts. *Nature Nanotechnology* **11,** 499–508. ISSN: 1748-3395 (2016).

25. Steiner, J. F. & von Oppen, F. Readout of Majorana qubits. *Physical Review Research* **2,** 033255 (2020).

26. Munk, M. I. K., Schulenborg, J., Egger, R. & Flensberg, K. Parity-to-charge conversion in Majorana qubit readout. *Physical Review Research* **2,** 033254 (2020).

27. Xie, H., Yu, S., Mao, H. & Jin, J. Majorana qubit readout by a point-contact detector under finite bias voltages. *Physical Review B* **111,** 075412 (2025).

28. Shor, P. W. Scheme for reducing decoherence in quantum computer memory. *Physical Review A* **52,** R2493(R) (1995).

29. Kitaev, A. Y. Unpaired Majorana fermions in quantum wires. *Physics-Uspekhi* **44,** 131 (2001).

30. Lutchyn, R. M., Bakkers, E., Kouwenhoven, L. P., Krogstrup, P., Marcus, C. & Oreg, Y. Majorana zero modes in superconductor-semiconductor heterostructures. *Nature Reviews Materials* **3,** 52–68 (2018).

31. Oreg, Y., Refael, G. & Oppen, F. V. Helical liquids and Majorana bound states in quantum wires. *Physical Review Letters* **105,** 177002 (2010).

32. Wimmer, M., Akhmerov, A. R., Dahlhaus, J. P. & Beenakker, C. W. J. Quantum point contact as a probe of a topological superconductor. *New Journal of Physics* **13,** 053016 (2011).

33. Cook, A. & Franz, M. Majorana fermions in a topological-insulator nanowire proximity-coupled to an s-wave superconductor. *Physical Review B* **84,** 201105(R) (2011).

34. Kjærgaard, M., Nichele, F., Suominen, H. J., Nowak, M., Wimmer, M., Akhmerov, A., Folk, J., Flensberg, K., Shabani, J., w. C. Palmstrøm & Marcus, C. Quantized conductance doubling and hard gap in a two-dimensional semiconductor-superconductor heterostructure. *Nature Communications* **7,** 1–6 (2016).

35. Suominen, H. J., Kjærgaard, M., Hamilton, A. R., Shabani, J., Palmstrøm, C. J., Marcus, C. M. & Nichele, F. Zero-energy modes from coalescing Andreev states in a two-dimensional semiconductor-superconductor hybrid platform. *Physical Review Letters* **119,** 176805 (2017).

36. De Juan, F., Ilan, R. & Bardarson, J. H. Robust transport signatures of topological superconductivity in topological insulator nanowires. *Phys. Rev. Lett.* **113,** 107003 (2014).

37. Chuang, P., Ho, S.-C., Smith, L. W., Sfigakis, F., Pepper, M., Chen, C.-H., Fan, J.-C., Griffiths, J., Farrer, I., Beere, H. E., Jones, G. A. C., Ritchie, D. A. & Chen, T.-M. All-electric all-semiconductor spin field-effect transistors. *Nature Nanotechnology* **10,** 35–39 (2015).

38. Stano, P., Fabian, J. & Jacquod, P. Nonlinear spin to charge conversion in mesoscopic structures. *Physical Review B* **85,** 241301(R) (2012).

39. Stano, P. & Jacquod, P. Spin-to-charge conversion of mesoscopic spin currents. *Physical Review Letters* **106,** 206602 (2011).

40. Schäpers, T. *Semiconductor Spintronics* (De Gruyter, Berlin, Boston, 2016).

41. Elzerman, J. M., Hanson, R., van Beveren, L. H. W., Witkamp, B., Vandersypen, L. M. K. & Kouwenhoven, L. P. Single-shot read-out of an individual electron spin in a quantum dot. *Nature* **430,** 431–435 (2004).

42. Nichele, F., Hennel, S., Pietsch, P., Wegscheider, W., Stano, P., Jacquod, P., Ihn, T. & Ensslin, K. Generation and detection of spin currents in semiconductor nanostructures with strong spin-orbit interaction. *Physical Review Letters* **114,** 206601 (2015).

43. Richter, E., Barth, M., Kozlov, D. A., Knothe, A., Mikhailov, N. N., Steidl, J., Gorini, C., Hartl, S., Himmler, W., Richter, K. & Weiss, D. Anomalous conductance steps in three-dimensional topological insulator HgTe-based quantum point contacts. *Physical Review Research* **7,** 013260 (2025).

44. Kozlovsky, R. *Magnetotransport in 3D topological insulator nanowires* Dissertation (Universität Regensburg, 2020).

45. Ihn, T. *Semiconductor Nanostructures* (Oxford University Press, 2010).

46. Hasan, M. Z. & Kane, C. L. Colloquium: Topological insulators. *Reviews of Modern Physics* **82,** 3045–3067 (2010).

47. Fischer, R. *Induced superconductivity in HgTe based topological insulator nanowires* Dissertation (Universität Regensburg, 2022).

48. Fischer, R. *Magnetocapacitance and transport measurements on HgTe-based 2D and 3D topological insulators* MA thesis (Universität Regensburg, 2016).

49. Ziegler, J. *Quantum transport in HgTe topological insulator nanostructures* Dissertation (Universität Regensburg, 2018).

50. Maier, H. *Geometrische Resonanzen in einem HgTe-basierten dreidimensionalen topologischen Isolator* Dissertation (Universität Regensburg, 2023).

51. Ando, T., Fowler, A. B. & Stern, F. Electronic properties of two-dimensional systems. *Reviews of Modern Physics* **54** (1982).

52. Yu, P. Y. & Cardona, M. *Fundamentals of Semiconductors* (Springer Berlin Heidelberg, 2010).

53. Sarma, S. D., Adam, S., Hwang, E. H. & Rossi, E. Electronic transport in two-dimensional graphene. *Reviews of Modern Physics* **83** (2011).

54. Kozlov, D. A., Kvon, Z. D., Olshanetsky, E. B., Mikhailov, N. N., Dvoretsky, S. A. & Weiss, D. Transport properties of a 3D topological insulator based on a strained high-mobility HgTe film. *Physical Review Letters* **112** (2014).

55. Hunklinger, S. *Festkörperphysik* (Oldenburg Wissenschaftsverlag GmbH, 2011).

56. Drude, P. Zur Elektronentheorie der Metalle. *Annalen der Physik* **306,** 566–613 (1900).

57. Heider, J. *Flippern mit Elektronen - Magnetotransport in Halbleiternanostrukturen* (Universität Regensburg, 2000).

58. Sarma, S. D. & Stern, F. Single-particle relaxation time versus scattering time in an impure electron gas. *Physical Review B* **32** (1985).

59. Von Klitzing, K., Dorda, G. & Pepper, M. New method for high-accuracy determination of the fine-structure constant based on quantized Hall resistance. *Physical Review Letters* **45,** 494–497 (1980).

60. *Private communication with D. A. Kozlov.*

61. Davies, J. H. *The physics of low-dimensional semiconductors* (Cambridge University Press, 1998).

62. Novoselov, K. S., Geim, A. K., Morozov, S. V., Jiang, D., Katsnelson, M. I., Grigorieva, I. V., Dubonos, S. V. & Firsov, A. A. Two-dimensional gas of massless Dirac fermions in graphene. *Nature* **438,** 197–200 (2005).

63. Goerbig, M. O. Electronic properties of graphene in a strong magnetic field. *Reviews of Modern Physics* **83,** 1193–1243 (2011).

64. Gospodarič, J., Dziom, V., Shuvaev, A., Dobretsova, A. A., Mikhailov, N. N., Kvon, Z. D., Novik, E. G. & Pimenov, A. Band structure of a HgTe-based three-dimensional topological insulator. *Physical Review B* **102** (2020).

65. Lee, J., Watanabe, K., Taniguchi, T. & Lee, H.-J. Realisation of topological zero-energy mode in bilayer graphene in zero magnetic feld. *Scientific Reports* **7,** 6466 (2017).

66. Berry, M. V. Quantal phase factors accompanying adiabatic changes. *Proceedings of the Royal Society A* **392,** 45 (1984).

67. Ziegler, J., Kozlovsky, R., Gorini, C., Liu, M.-H., Weishäupl, S., Maier, H., Fischer, R., Kozlov, D. A., Kvon, Z. D., Mikhailov, N., Dvoretsky, S. A., Richter, K. & Weiss, D. Probing spin helical surface states in topological HgTe nanowires. *Physical Review B* **97** (2018).

68. Koester, S., Brar, B., Bolognesi, C., Caine, E., Patlach, A., Hu, E., Kroemer, H. & Rooks, M. Length dependence of quantized conductance in ballistic constrictions fabricated on InAs/AlSb quantum wells. *Physical Review B* **53,** 13063 (1996).

69. Többen, D., Wharam, D. A., Abstreiter, G., Kotthaus, J. P. & Schäffler, F. Ballistic electron transport through a quantum point contact defined in a $Si/Si_{0.7}Ge_{0.3}$ heterostructure. *Semiconductor Science and Technology* **10,** 711–714 (1995).

70. Goel, N., Graham, J., Keay, J., Suzuki, K., Miyashita, S., Santos, M. & Hirayama, Y. Ballistic transport in InSb mesoscopic structures. *Physica E: Low-dimensional Systems and Nanostructures* **26,** 455–459 (2005).

71. Yacoby, A. & Imry, Y. Quantization of the conductance of ballistic point contacts beyond the adiabatic approximation. *Physical Review B* **41,** 5341 (1990).

72. Szafer, A. & Stone, A. D. Theory of quantum conduction through a constriction. *Physical Review Letters* **62,** 300–303 (1989).

73. Knobbe, J. & Schäpers, T. Magnetosubbands of semiconductor quantum wires with Rashba spin-orbit coupling. *Physical Review B* **71,** 035311 (2005).

74. Trottmann, M. *Characterisation of III-V semiconductor hybrid systems for spinorbitronic functionality* Dissertation (Universität Regensburg, 2020).

75. Gudina, S. V., Neverov, V. N., Ilchenko, E. V., Bogolubskii, A. S., Harus, G. I., Shelushinina, N. G., Podgornykh, S. M., Yakunin, M. V., Mikhailov, N. N. & Dvoretsky, S. A. Electron effective mass and g factor in wide HgTe quantum wells. *Semiconductors* **52,** 12–18 (2018).

76. Yakunin, M. V., Podgornykh, S. M., Mikhailov, N. N. & Dvoretsky, S. A. Spin splittings in the n-$HgTe/Cd_xHg_{1-x}Te$ (013) quantum well with inverted band structure. *Physica E* **42,** 948–951 (2010).

77. Marx, A. & Gross, R. *Festkörperphysik* (München: De Gruyter Oldenbourg, 2014).

78. Dresselhaus, G. Spin-orbit coupling effects in zinc blende structures. *Physical Review* **100,** 580–586 (1955).

79. Rashba, E. Properties of semiconductors with an extremum loop. 1. Cyclotron and combinational resonance in a magnetic field perpendicular to the plane of the loop. *Sov. Phys. Solid State* **2,** 1109–1122 (1960).

80. Bychkov Y. A. Rasbha, E. I. Properties of a 2D electron gas with lifted spectral degeneracy. *P. Zh. Eksp. Teor. Fiz.* **39,** 66–69 (1984).

81. Lechner, V. *Bulk and structure inversion asymmetry in semiconductor quantum well structures* Dissertation (Universität Regensburg, 2012).

82. Minkov, G., Rut, O. E., Sherstobitov, A. A., Dvoretsky, S. A. & Mikhailov, N. N. Zeeman splitting of conduction band in HgTe quantum wells near the Dirac point. *Physica E* **91,** 203–208 (2017).

83. Gui, Y. S., Becker, C. R., Dai, N., Liu, J., Qiu, Z. J., Novik, E. G., Schäfer, M., Shu, X. Z., Chu, J. H., Buhmann, H. & Molenkamp, L. W. Giant spin-orbit splitting in a HgTe quantum well. *Physical Review B* **70** (2004).

84. Manchon, A., Koo, H. C., Nitta, J., Frolov, S. M. & Duine, R. A. New perspectives for Rashba spin–orbit coupling. *Nature Materials* **14,** 871 (2015).

85. Ganichev, S. D. & Golub, L. E. Interplay of Rashba/Dresselhaus spin splittings probed by photogalvanic spectroscopy – A review. *Phys. Status Solidi B* **251,** 1–23 (2014).

86. Liu, J., Daumer, V., Gui, Y. S., Hock, V., Becker, C. R., Buhmann, H. & Molenkamp, L. W. Competition between Rashba effect and exchange interaction in a $Hg_{0.98}Mn_{0.02}Te$ magnetic 2DEG. *Journal of Superconductivity* **16,** 365–368 (2003).

87. Park, Y. H., Kim, H.-j., Chang, J., Han, S. H., Eom, J., Choi, H.-J. & Koo, H. C. Separation of Rashba and Dresselhaus spin-orbit interactions using crystal direction dependent transport measurements. *Applied Physics Letters* **103,** 252407 (2013).

88. Thouless, D. J., Kohmoto, M., Nightingale, M. P. & Nijs, M. D. Quantized Hall conductance in a two-dimensional periodic potential. *Physical Review Letters* **49,** 405–408 (1982).

89. Kohmoto, M. Topological invariant and the quantization of the Hall conductance. *Annals of Physics* **160,** 343–354 (1985).

90. Yang, Y., Xu, Z., Sheng, L., Wang, B., Xing, D. Y. & Sheng, D. N. Time-reversal-symmetry-broken quantum spin Hall effect. *Physical Review Letters* **107** (2011).

91. Kane, C. & Mele, E. J. Quantum Spin Hall Effect in Graphene. *Physical Review Letters* **95,** 226801 (2005).

92. Fu, L. & Kane, C. L. Topological insulators with inversion symmetry. *Physical Review B* **76,** 045302 (2007).

93. Bernevig, B. A., Hughes, T. L. & Zhang, S.-C. Quantum spin Hall effect and topological phase transition in HgTe quantum wells. *Science* **314,** 1757–1761 (2006).

94. Ando, Y. Topological insulator materials. *Journal of the Physical Society of Japan* **82,** 102001 (2013).

95. Ando, T., Nakanishi, T. & Saito, R. Berry's phase and absence of back scattering in carbon nanotubes. *Journal of the Physical Society of Japan* **67,** 2857–2862 (1998).

96. König, M., Buhmann, H., Molenkamp, L., Hughes, T., Liu, C., Qi, X. & Zhang, S. The quantum spin Hall effect: Theory and experiment. *Journal of the Physical Society of Japan* **77,** 031007. ISSN: 0031-9015 (2008).

97. Gerchikov, L. G. & Subashiev, A. V. Interface states in subband structure of semiconductor quantum wells. *Physica Status Solidi B* **160,** 443 (1990).

98. Büttner, B., Liu, C., Tkachov, G., Novik, E., Brüne, C., Buhmann, H., Hankiewicz, E., Recher, P., Trauzettel, B., Zhang, S. & Molenkamp, L. Single valley Dirac fermions in zero-gap HgTe quantum wells. *Nature Physics* **7,** 418–422 (2011).

99. Kvon, Z. D., Olshanetsky, E. B., Kozlov, D. A., Novik, E., Mikhailov, N. N. & Dvoretsky, S. A. Two-dimensional semimetal in HgTe-based quantum wells. *Low Temperature Physics* **37,** 202–209 (2011).

100. Diniz, L. G. & Mohallem, J. R. Asymptotic relation between Darwin and mass-velocity one-electron molecular relativistic corrections. *American Journal of Physics* **74** (2006).

101. Berchenko, N. & Pashkovskii, M. V. Mercury telluride – a zero-gap semiconductor. *Soviet Physics - Uspekhi* **19,** 462–480 (1976).

102. Wu, S. C., Yan, B. & Felser, C. Ab initio study of topological surface states of strained HgTe. *Europhysics Letters* **107,** 57006 (2014).

103. Brüne, C., Thienel, C., Stuiber, M., Böttcher, J., Buhmann, H., Novik, E. G., Liu, C.-X., Hankiewicz, E. M. & Molenkamp1, L. W. Dirac-screening stabilized surface-state transport in a topological insulator. *Physical Review X* **4** (2014).

104. Kvon, Z. D., Kozlov, D. A., Olshanetsky, E. B., Gusev, G. M., Mikhailov, N. N. & Dvoretsky, S. A. Topological insulators based on HgTe. *Physics-Uspekhi* **63,** 629–647 (2020).

105. Wu, S.-C., Yan, B. & Felser, C. Ab initio study of topological surface states of strained HgTe. *Europhysics Letters* **107** (2014).

106. Kozlov, D. A., Bauer, D., Ziegler, J., Fischer, R., Savchenko, M. L., Kvon, Z. D., Mikhailov, N. N., Dvoretsky, S. A. & Weiss, D. Probing quantum capacitance in a 3D topological insulator. *Physical Review Letters* **116,** 166802 (2016).

107. Steidl, J. *Annealing of HgTe-based 3D topological insulator nanostructures* MA thesis (Universität Regensburg, 2023).

108. Daumer, V., Golombek, I., Gbordzoe, M., Novik, E. G., Hock, V., Becker, C. R., Buhmann, H. & Molenkamp, L. W. Quasiballistic transport in HgTe quantum-well nanostructures. *Applied Physics Letters* **83,** 1376–1378 (2003).

109. Varavin, V. S., Dvoretsky, S. A., Mikhailov, N. N., Remesnik, V. G., Sabinina, I. V., Sidorov, Y. G., Shvets, V. A., Yakushev, M. V. & Latyshev, A. V. Molecular beam epitaxy of CdHgTe: Current state and horizons. *Optoelectronics, Instrumentation and Data Processing* **56,** 456–469 (2020).

110. Maier, H., Ziegler, J., Fischer, R., Kozlov, D., Kvon, Z. D., Mikhailov, N. N., Dvoretsky, S. A. & Weiss, D. Ballistic geometric resistance resonances in a single surface of a topological insulator. *Nature Communications* **8** (2017).

111. Maier, F. *Hafniumdioxid als Isolator auf HgTe-basierten zweidimensionalen topologischen Isolatoren* (Universität Regensburg, 2021).

112. Pobell, F. *Matter and methods at low temperatures* (Springer-Verlag Berlin Heidelberg, 2007).

113. *Datasheet Femto DLPVA-100-F Series* `https://www.eoc-inc.com/wp-content/uploads/FEMTO-DLPVA-100-FS-FD-R6.pdf` (2025).

114. Ziegler, J., Kozlov, D. A., Mikhailov, N. N., Dvoretsky, S. & Weiss, D. Quantum Hall effect and Landau levels in the three-dimensional topological insulator HgTe. *Physical Review Research* **2,** 033003 (2020).

115. Kvon, Z. D., Olshanetsky, E. B., Kozlov, D. A., Mikhailov, N. N. & Dvoretsky, S. A. Two-dimensional electron–hole system in a HgTe-based quantum well. *JETP Letters* **87,** 502–505 (2008).

116. Halperin, B. I. Quantized Hall conductance, current-carrying edge states, and the existence of extended states in a two-dimensional disordered potential. *Physical Review B* **25,** 2185–2190 (1982).

117. Thomas, K. J. Possible spin polarization in a one-dimensional electron gas. *Physical Review Letters* **77,** 135 (1996).

118. Cronenwett, S. M., Lynch, H. J., Goldhaber-Gordon, D., Kouwenhoven, L. P., Marcus, C. M., Hirose, K., Wingreen, N. S. & Umansky, V. Low-temperature fate of the 0.7 structure in a point contact: A Kondo-like correlated state in an open system. *Physical Review Letters* **88,** 226805 (2002).

119. Groth, C. W., Wimmer, M., Akhmerov, A. R. & Waintal, X. Kwant: a software package for quantum transport. *New Journal of Physics* **16,** 063065 (2014).

120. Neverov, V. N., Bogolubskii, A. S., Gudina, S. V., Podgornykh, S. M., Turutkin, K. V., Popov, M., Shelushinina, N. G., Yakunin, M. V., Mikhailov, N. N. & Dvoretsky, S. Effective mass and g-factor of two-dimentional HgTe Γ_8-band electrons: Shubnikov–de Haas oscillations. *Semiconductors* **54,** 982 (2020).

121. Essert, S. *Mesoscopic transport in topological insulator nanostructures* Dissertation (Universität Regensburg, 2016).

122. Peierls, R. On the theory of the diamagnetism of conduction electrons, II. Strong magnetic fields. *Z. Phys* **81,** 186 (1933).

123. Ferry, D. & Goodnick, S. M. *Transport in Nanostructures, Cambridge Studies in Semiconductor Physics and Microelectronic Engineering* (Cambridge University Press, 1997).

124. Minkov, G. M., Rut, O. E., Sherstobitov, A. A., Dvoretsky, S. A. & Mikhailov, N. N. Zeeman splitting of the conduction band of HgTe quantum wells with a semimetallic spectrum. *Condensed Matter* **104,** 241–247 (2016).

125. Kozlov, D., Ziegler, J., Mikhailov, N. N., Dvoretsky, S. A. & Weiss, D. Shubnikov-de Haas oscillations in a three-dimensional topological insulator based on a strained HgTe film in an inclined magnetic field. *JETP Letters* **109,** 799–805 (2019).

126. Lechner, V., Golub, L. E., Olbrich, P., Stachel, S., Schuh, D., Wegscheider, W., Bel'kov, V. V. & Ganichev, S. D. Tuning of structure inversion asymmetry by the -doping position in (001)-grown GaAs quantum wells. *Applied Physics Letters* **94,** 242109 (2009).

127. Dolgopolov, V. T. & Gold, A. Magnetoresistance of a two-dimensional electron gas in a parallel magnetic field. *JETP Letters* **71,** 27–30 (2000).

128. Okamoto, T., Hosoya, K., Kawaji, S. & Yagi, A. Spin degree of freedom in a two-dimensional electron liquid. *Phys. Rev. Lett.* **82** (1999).

129. Okamoto, T., Hosoya, K., Kawaji, S., Yagi, A., Yutani, A. & Shiraki, Y. Metal–insulator transition and spin degree of freedom in Silicon 2D electron systems. *Physica E* **6,** 260–263 (2000).

130. Minkov, G. M., Aleshkin, V. Y., Rut, O. E., Sherstobitov, A. A., Germanenko, A. V., Dvoretsky, S. A. & N.Mikhailov, N. Valence band energy spectrum of HgTe quantum wells with an inverted band structure. *Physical Review B* **96,** 035310 (2017).

131. Beenakker, C. W. J. & van Houten, H. Quantum transport in semiconductor nanostructures. *Solid State Physics* **44,** 1–228 (1991).

132. Houten, H. v., Wees, B. v., Mooij, J., Roos, G. & Berggren, K.-F. Magnetic depopulation of subbands and universal conductance fluctuations in quasi-one dimensional GaAs-AlGaAs heterostructures. *Superlattices and Microstructures* **3** (1987).

133. Patel, N. K., Nicholls, J. T., Martin-Moreno, L., Pepper, M., Frost, J. E. F., Ritchie, D. A. & Jones, G. A. C. Properties of a ballistic quasi-one-dimensional constriction in a parallel high magnetic field. *Physical Review B* **44,** 10973 (1991).

134. Minkov, G. M., Aleshkin, V. Y., Rut, O. E., Sherstobitov, A. A., Germanenko, A. V., Dvoretsky, S. & Mikhailov, N. N. Spin-orbit splitting of the conduction band in HgTe quantum wells: Role of different mechanisms. *Physica E: Low-dimensional Systems and Nanostructures* **110,** 95–99 (2019).

135. Michetti, P., Budich, J. C., Novik, E. G. & Recher, P. Tunable quantum spin Hall effect in double quantum wells. *Physical Review B* **85,** 125309 (2012).

136. Graf, A., Kozlovsky, R., Richter, K. & Gorini, C. Theory of magnetotransport in shaped topological insulator nanowires. *Physical Review B* **102,** 165105 (2020).

137. Kozlovsky, R., Graf, A., Kochan, D., Richter, K. & Gorini, C. Magnetoconductance, quantum Hall effect, and Coulomb blockade in topological insulator nanocones. *Physical Review Letters* **124,** 126804 (2020).

138. Barth, M. *Spectral properties and quantum transport in hybrid Dirac systems* Dissertation (Universität Regensburg, 2023).

139. Calzona, A. & Trauzettel, B. Moving Majorana bound states between distinct helical edges across a quantum point contact. *Physical Review Research* **1,** 033212 (2019).

140. Plato. *The Republic, Book VII, 514a-521d* (Plumbstone Books, 2016).

141. Koelbl, H. *Ich habe keine Angst vor dem Tod* `https://www.zeit.de/zeit-magazin/2016/45/klaus-von-klitzing-physik-nobelpreistraeger-rettung` (2025).

142. Rothe, D. G., Reinthaler, R. W., Liu, C.-X., Molenkamp, L. W., Zhang, S.-C. & Hankiewicz, E. M. Fingerprint of different spin–orbit terms for spin transport in HgTe quantum wells. *New Journal of Physics* **12,** 065012 (2010).

Danksagung

Die Zeit der Promotion war für mich ein Prozess der persönlichen Reifung. Die Jahre des Suchens, des Zweifelns und des Findens haben mich nicht nur fachlich, sondern auch menschlich weiterentwickeln lassen. Stünde ich heute vor der Entscheidung, am Lehrstuhl Weiss zu promovieren, so würde ich denselben Weg wieder gehen. Mein Dank gilt all jenen, die diese Zeit in direkter oder indirekter Weise begleitet und bereichert haben:

- Prof. Dr. Dieter Weiss dafür, dass er mir die Durchführung einer Dissertation an diesem Thema ermöglicht hat. Vielen Dank für die wegweisenden Einschätzungen und die zahlreichen Diskussionen zur Interpretation der Ergebnisse. Besonders geschätzt habe ich Ihren Betreuungsstil, der Freiheit und Führung in ausgewogenem Maße vereinte. In Ihrer bedachten, ruhigen Art sind Sie mir nicht nur als Wissenschaftler, sondern auch als Mensch Vorbild.

- Dr. Dmitriy Kozlov für die vielen Diskussionen zur Interpretation der Ergebnisse und für hilfreiche Ratschläge zu den Messungen. Besonders verbunden fühlte ich mich ihm in seinem Dasein als letzter verbliebener Kollege in der Topo-Gruppe.

- Dr. Michael Barth, Dr. Cosimo Gorini, Dr. Angelika Knothe und Prof. Dr. Klaus Richter für das Entwickeln der Theorie zu meinen Messergebnissen und die zahlreichen Diskussionen darüber. Insbesondere danke ich Michael für die unzähligen Simulationen zu meinen Messungen und das Beantworten all meiner weiteren Fragen zur Theorie.

- Prof. Dr. Dominique Bougeard für das Übernehmen des Zweitgutachtens.

- Wolfgang Himmler und Dr. Ralf Fischer für die gute Zusammenarbeit beim Betreuen des Mischkryostaten.

- den Technikern und der Technikerin des Lehrstuhls, Uli Gürster, Daniel Pahl, Michael Weigl, Cornelia Linz und Thomas Haller, für die Unterstützung an den Anlagen, insbesondere Michael für seine Hilfe bei Wartungen des Mischkryos.

- PD Dr. Jonathan Eroms, Dr. Robin Huber und Julia Amann für die gute Zusammenarbeit beim Betreuen der Rasterkraftmikroskope.

- Elke Haushalter und Claudia Moser für ihre Hilfe bei administrativen Angelegenheiten.

- den Studierenden, die ich betreuen durfte, Juliane Steidl und Florian Maier, für eine vertrauensvolle und warmherzige Zusammenarbeit. Darüber hinaus möchte ich Juliane als treueste Kaffeeseele und loyale Bürokollegin würdigen.
- den Werkstudenten, mit denen ich zusammenarbeiten durfte, Stefan Obloh und Tobias Biehler, für das zuverlässige Überheben von flüssigem Helium und Stickstoff am Mischkryostaten.
- für ihre Hilfsbereitschaft insbesondere den Doktoranden Tobias Rockinger, Niklas Hüttner, Dr. Benedikt Grünewald und Dr. Ralf Fischer.
- für das Korrekturlesen dieser Arbeit Prof. Dr. Dieter Weiss, Dr. Dmitriy Kozlov, Dr. Hubert Maier, Dr. Stefan Hartl, Dr. Jan Bärenfänger, Niklas Hüttner, Felix Braun, Fabian Haneder, Dr. Ralf Fischer, Dr. Robin Huber, Agata Zielińska, Pauline Drexler, Juliane Steidl und Rudolf Richter.
- der glorreichen GBU-Gang, bestehend aus dem Trio Robin Huber, Hubert Maier und mir, ergänzt durch Sofia Franke, für eine gelungene Zeit voller Abenteuer im Büro 8.1.25 und auf Ausflügen ins Gebirge. Auch danke ich meiner späteren Bürokollegin Agata Zielińska für eine gute Zeit, in der sich eine polnisch-tschechische Freundschaft entwickelt hat.
- Christian Scholtes und Prof. Dr. Gabriele Hierlmeier für den Dialog zur Chemie bei gemeinsamen Mensabesuchen.
- Dr. Dieter Schuh, dem ich den Impuls verdanke, mich am Lehrstuhl Weiss zur Promotion zu bewerben. Diesen Mut hätte ich sonst womöglich nicht gehabt.
- Jeder Weg beginnt in der Schule. Meinen Physiklehrern danke ich dafür, dass sie mich für ein Studium der Physik begeistern konnten.
- meinen Eltern Ivana und Oswald Richter und meinem Großvater MUDr. Antonín Šulc dafür, dass sie in mir eine Faszination für die Phänomene der Natur geweckt haben.
- meinem Bruder Rudolf dafür, dass wir es immer wieder geschafft haben, schwierige Zeiten innerhalb der Familie durch hervorragende Zusammenarbeit zu überwinden. Nicht nur blieb er mir als Kollege durch seine Doktorarbeit bei Prof. Dr. Dominique Bougeard in besonderer Weise verbunden, sondern durch viele gemeinsame Interessen und als kritischer Ratgeber auch als ein Freund.
- allen Freunden und Wegbegleitern, die ich hier gar nicht alle nennen kann, dafür, dass sie mich in dieser langen Zeit durch ihre Präsenz unterstützt und an mich geglaubt haben. Einem von ihnen gilt mein besonderer Dank.
- Jedem und jeder Einzelnen für jedes gute Gespräch, das stattgefunden hat.